PRODUCTION AND CHARACTERIZATION OF AMORPHOUS SILICON THIN-FILM SOLAR CELLS ON FLEXIBLE SUBSTRATES WITH LASER TEXTURING

A THESIS SUBMITTED TO
THE GRADUATE SCHOOL OF NATURAL AND APPLIED SCIENCES
OF
MIDDLE EAST TECHNICAL UNIVERSITY

BY

ZEYNEP DEMİRCİOĞLU

IN PARTIAL FULFILLMENT OF THE REQUIREMENTS
FOR
THE DEGREE OF DOCTOR OF PHILOSOPHY
IN
PHYSICS

MARCH 2022

Approval of the thesis:

PRODUCTION AND CHARACTERIZATION OF AMORPHOUS SILICON THIN-FILM SOLAR CELLS ON FLEXIBLE SUBSTRATES WITH LASER TEXTURING

submitted by **ZEYNEP DEMİRCİOĞLU** in partial fulfillment of the requirements for the degree of **Doctor of Philosophy** i**n Physics, Middle East Technical University** by,

Prof. Dr. Halil Kalıpçılar
Dean, Graduate School of **Natural and Applied Sciences** ________________

Prof. Dr. Seçkin Kürkçüoğlu
Head of the Department, **Physics** ________________

Prof. Dr. Raşit Turan
Supervisor, **Physics, METU** ________________

Examining Committee Members:

Prof. Dr. Macit Özenbaş
Metallurgical and Materials Eng, METU ________________

Prof. Dr. Raşit Turan
Physics, METU ________________

Prof. Dr. Mehmet Parlak
Physics, METU ________________

Assoc. Prof. Dr. Mustafa Kulakcı
Physics, Eskişehir Teknik Uni. ________________

Assoc. Prof. Dr. Tahir Çolakoğlu
Physics Eng., Ankara Uni. ________________

Date: 10.03.2022

I hereby declare that all information in this document has been obtained and presented in accordance with academic rules and ethical conduct. I also declare that, as required by these rules and conduct, I have fully cited and referenced all material and results that are not original to this work.

Name Last name : Zeynep Demircioğlu

Signature :

ABSTRACT

PRODUCTION AND CHARACTERIZATION OF AMORPHOUS SILICON THIN-FILM SOLAR CELLS ON FLEXIBLE SUBSTRATES WITH LASER TEXTURING

Demircioğlu, Zeynep
Doctor of Philosophy, Physics
Supervisor : Prof. Dr. Raşit Turan

March 2022, 160 pages

Thin-film photovoltaic (PV) panels are promising technologies in the PV market due to their low production costs and other advantages such as temperature resistance and diffuse radiation performances. Thin-film photovoltaic panels can be produced on not only rigid substrates but also on flexible substrates. Flexible solar cells have several advantages: flexibility, lightweight, mobility, and easy transport specifications. The scope of the research presented is to study low-temperature deposition and optimization of hydrogenated amorphous silicon (a-Si:H) deposition for flexible solar cells. The aim of this study is to optimize the flexible solar cell process by investigating the effects of deposition parameters on a-Si:H thin film properties and cells, to obtain surface texturing on transparent conductive oxide by a novel texture, which is done by direct laser writing, to scale-up from cell to monolithically series-connected flexible solar module. Different flexible substrates are compared for flexible solar cell production. A novel texturing of aluminum-doped zinc oxide (AZO) films is proposed and deposited on flexible substrates for photovoltaic applications. A comparative study of the effects of different laser

wavelengths on texturing/patterning of AZO is discussed. Single-junction flexible thin-film solar cell production methods and efficiency enhancements are developed and applied. Thin-film deposition optimization in CVD chambers and laser processes is optimized during this study.

Keywords: Flexible Solar Cell, Amorphous Silicon, PECVD, Sputter, Laser Process

ÖZ

ESNEK ALTTAŞLAR ÜZERİNE LAZER İLE DESENLENDİRİLMİŞ AMORF SİLİSYUM İNCE FİLM GÜNEŞ GÖZESİ ÜRETİMİ VE KARAKTERİZASYONU

Demircioğlu, Zeynep
Doktora, Fizik
Tez Yöneticisi: Prof. Dr. Raşit Turan

Mart 2022,160 sayfa

İnce film fotovoltaik (FV) panelleri, düşük üretim maliyetleri ve ısıya karşı dayanıklılık ve indirek radyasyon performansı gibi diğer avantajları nedeniyle FV pazarında umut verici teknolojilerdir. İnce film fotovoltaik panelleri sadece sert alttaşlara değil esnek alttaşlara da üretilebilir. Esnek güneş gözeleri, esneklik, hafiflik, mobilite ve kolay taşınabilirlik gibi özellikleri sayesinde birçok avantaja sahiptir. Sunulan çalışmanın kapsamı, esnek güneş gözeleri için düşük sıcaklıkta biriktirme ve hidrojene amorf silisyum (a-Si:H) büyütmenin optimizasyonunu incelemektir. Esnek güneş gözesi üretimi için farklı esnek yüzeyler karşılaştırılır. Alüminyum katkılı çinko oksit (AZO) filmleri fotovoltaik uygulamalar için esnek substratlar üzerinde biriktirilmiş ve bu tabakanın pürüzlendirmesi yeni bir yöntemle çalışılmıştır. Farklı lazer dalga boylarının AZO tabakasının pürüzlendirilmesi üzerindeki etkileri karşılaştırmalı olarak tartışılmıştır. Tek eklemli esnek ince film güneş gözesi üretim yöntemleri ve verimlilik iyileştirmeleri geliştirilmiş ve uygulanmıştır. Bu çalışmada plazma destekli kimyasal buhar biriktirme (PECVD) odalarında ince film biriktirme ve lazer işlemleri optimize edilmiştir. Bu çalışmanın amacı, birikme parametrelerinin a-Si:H ince film özellikleri ve güneş gözeleri üzerindeki etkilerini araştırarak esnek güneş gözesi üretim sürecini optimize etmek, doğrudan lazerle yazma ile yapılan yeni bir pürüzlendirme ile şeffaf iletken oksit üzerinde yüzey dokusu elde etmek ve tek eklemli güneş gözesinden monolitik seri bağlı esnek güneş modülü elde etmektir.

Anahtar Kelimeler: Esnek Güneş Gözesi, Amorf Silisyum, PECVD, Sıçratma, Lazer İşleme

To love

ACKNOWLEDGMENTS

I would like to express my deepest gratitude to my supervisor Prof. Raşit Turan, for his guidance, advice, criticism, encouragement, and insight throughout the research.

I would like to express my sincere gratitude to my TİK committee members, Prof. Macit Özenbaş and Prof. Mehmet Parlak, for their suggestions, comments, and support.

I would like to thank Prof. Robert Balog for helping me approach problems from an engineering perspective. This thesis is partially supported by his project Smart PV Skin with project number NPRP 7 - 299 - 2 - 124.

My deepest thanks go to my colleagues, Mr. Engin Özkol, Ph.D., Mr. Hisham Nasser, Ph.D., and Mr. Ergi Dönerçark, Ph.D. This work would not have been possible without Engin, whose process and productions I learned, and his valuable suggestions. In addition, after I started my business life, this thesis would not have been completed without Ergi's support. I would also like to thank Hisham for his support and technical assistance when I lost faith in this thesis.

Special thanks to Miss. E. Hande Çiftpınar for her moral, material, technical, academic, and other support, which I regard as my family. She deserves my deepest thank for her patience and suggestions during the writing of this thesis. I would like to thank my supporters, Mrs. Makbule Bilgen, Ph.D., Mrs. Serim İlday, Ph.D., and Miss. Gamze Kökbudak, for making this thesis journey enjoyable for all of us.

I would like to thank countless other people who supported me during my thesis. Especially, I would like to thank all GÜNAM researchers and staff. I would also like to thank my business life colleagues, who taught me patience.

Last but not least, my family deserves endless gratitude. None of this would have happened without the love and support of my beloved husband Olgu and my dear daughter Arya and my lifetime supporter sister Sibel.

TABLE OF CONTENTS

LIST OF TABLES

TABLES

LIST OF FIGURES

FIGURES

CHAPTER 1

INTRODUCTION

Technology is developing rapidly throughout the world, and as a result, energy demand is increasing exponentially. This demand created the need for lower-cost energy generation. Also, the Global warming concerns created the sustainability research field to find greener and renewable energy sources.

The COVID-19 pandemic, which started at the end of 2019, affected the world in every aspect in 2020, causing a significant economic crisis globally. Although the closure of the whole world caused a decrease in energy consumption, the share of renewable energy in production has increased [1]. As a result, solar energy has proven its importance and place in the market among the inexhaustible, green, and renewable energy sources.

Solar energy conversion into electricity occurs by two different methods, either directly or indirectly. The method of obtaining thermal energy indirectly from the sun is solar thermal. It is used to meet the heat energy requirement. Another indirect energy conversion is concentrated solar energy, used for electrical energy generation. Concentrated solar energy is an energy conversion obtained by converting the solar energy into heat and transferring the converted energy to the turbines to acquire electricity. The direct conversion of solar energy to electrical energy is done by the photovoltaic effect (PV). Structures working with the PV effect principle are solar cells.

The discovery of the “photovoltaic effect” was founded by Edmond Becquerel in 1839, but no further research was conducted until the 1950s. [2]. Silicon layers have been used for photovoltaic technology since the 1950s. In 1953, Daryl Chapin and

Calvin Fuller, the two scientists at Bell Laboratories, demonstrated the first silicon solar cell, which converts enough energy to electrical power via a p-n junction [3]. These studies were on crystalline silicon, which is solid and fragile—increasing production costs, creating research opportunities to investigate methods to deliver cost-effective solutions. Later a new material was developed by Sterling et al., based on the deposition of silicon thin-film from silane gas in 1965 [4]. Better and acceptable quality of undoped amorphous silicon layers were obtained by Chittick et al. from a silane discharge in 1969 [5].

The ability to produce silicone in thin layers allowed the low-cost production of solar energy. In 1975 Spear and LeComber reported that amorphous silicon could be doped to obtain p and n-type materials [6]. In 1976 Carlson and Wronski announced the first experimental a-Si:H solar cell made at the Radio Corporation of America (RCA) Laboratory with 2.4% efficiency (on glass) [7]. In addition to that, Wronski, Carlson, and Daniel at RCA Laboratories reported a Pt/a-Si:H Schottky barrier solar cell made on a stainless-steel substrate [8]. The production of thin-film silicon solar cells started the new era called second-generation solar cells.

In 1977 Staebler and Wronski reported a decrease in the photoconductivity under illumination. Also, another decrease in the dark conductivity after illumination [9]. This effect caused by the amorphous structure is known as the light-induced degradation (LID) or Staebler-Wronski effect (SWE). Although this feature is one of the most significant disadvantages against crystal silicon, it also has cost reduction advantages due to less material usage, low temperature, and large-area production possibilities. After the evolution of the plastic industry in the 1980s, plastic substrates gain an attraction. As a result, 1980s p+–i–n+ a-Si:H/ITO solar cells were made on organic polymer (plastic) film substrates by Okaniwa et al. [10]. Later in the 1990s, the production of flexible modules on the plastic substrates was produced by roll-roll processes.

1.1 Amorphous Silicon

In the thin-film silicon solar cells (TFSSC) structure, silicon is used mainly in the amorphous form since the amorphous silicon has a higher direct bandgap than the crystalline form. Also, the absorption coefficient of the amorphous silicon material is higher when compared to the crystalline version. This property of amorphous silicon makes it possible to be used in TFSSC as a very thin layer [11].

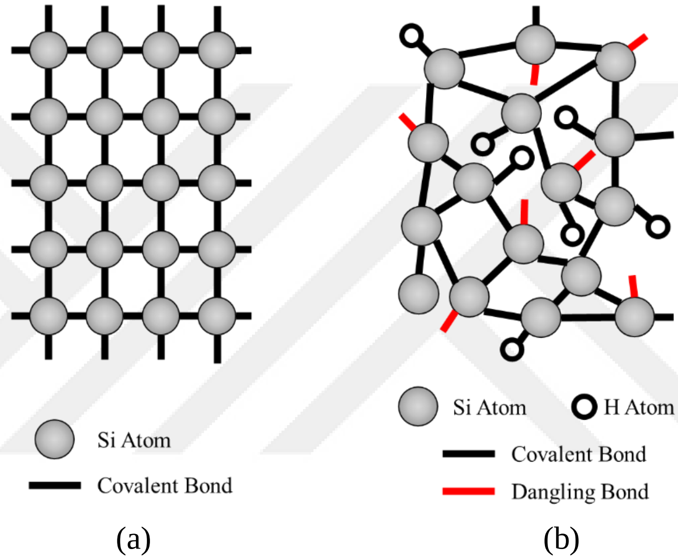

Figure 1.1 Atomic structure of (a) c-Si b) a-Si

The term amorphous is commonly used for non-crystalline materials. Figure 1.1 shows the comparison of crystalline and amorphous silicon (a-Si) atomic structures. Silicon atoms bond four neighboring atoms in the structure. In crystalline silicon (c-Si), the atoms are oriented in a periodic structure; the bonds have the same length and same angle (Figure 1.1 (a)). Due to the well-oriented structure, c-Si has long-range order. However, there are slight differences in bond length and angle between the atoms of the amorphous structure, making the material amorphous with a continuous random network. Thus, some atoms remain unbonded in the structure. This difference creates a disoriented material. (See Figure 1.1(b)). Such broken bonds are called dangling bonds and act as defects in the material. Dangling bonds can be passivated by another atom, which is done with a hydrogen (H) atom for silicon material. Passivated dangling bonds no mare act as a defect state. Thus, the improved form of amorphous silicon, generally known as hydrogenated amorphous silicon or briefly a-Si:H, is used in TFSSC. The amorphous form of silicon without any passivation has a high, dangling bond, which results in a defect density of 10^{19} defects/cm^3. Hydrogenated amorphous silicon (a-Si:H) passivates dangling bonds and has a relatively low defect density of 10^{16} defects/cm^3 [12].

Defects caused by the highly disordered structure directly affect the charge transport mechanism in the amorphous silicon structure. Due to short-range order, charge carriers are not free to move and are confined within the material, which is also called localization, and it is the cause of the band tails. The variations and the disorientations between the bonds result in band tails at the edge of valance and conduction bands. In addition, dangling bonds behave like trap states which are referred to as defect states that lie between the valance band tail and conduction band tail. Band tails and defect states combine to form a continuous distribution between non-localized states. This distribution of density of states, Figure 1.2, causes the bandgap of a-Si to be different from c-Si, and for a-Si material, the bandgap is defined as the mobility bandgap.

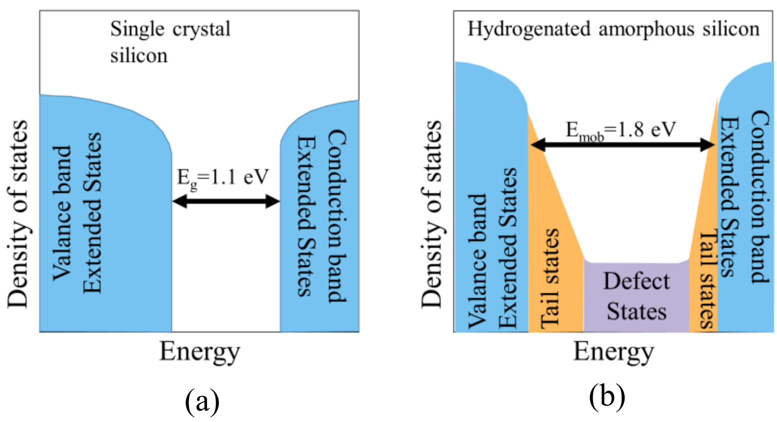

Figure 1.2 Schematic representation of the density of states of (a) c-Si (b) a-Si:H

Thin-film silicon solar cell uses silicon mainly in the amorphous form since the a-Si has a direct bandgap. A highly disordered form of silicon increases its absorbance. The bandgap of this material is higher (1.75 eV) than the crystalline form (1.1 eV). Additionally, the absorption coefficient of the a-Si:H is higher than the c-Si [11]. The material requirement in the system decreases as the absorbance increases. Thus, a-Si:H is a preferable choice for thin-film solar cells.

1.2 Thin Film Silicon Solar Cell

Thin-film silicon solar cells work with the principle of photovoltaic effect, which is the conversion of light into current. The conversion of light into electrical energy consists of i) generation of charged particles, ii) separation of charged particles from each other, and iii) collection of separated particles to pass over a load.

The material absorbs the photon that enters the system, and the generation of charged particles is ensured. This process, also referred to as photogeneration, is related to the bandgap of the material forming the thin-film silicon solar cell structure. Photons with at least as much energy as the bandgap energy or higher energies contribute to photogeneration. The absorbed photon excites the electrons (negatively charged carriers) from the valance band and leaves a hole (positively charged carrier) behind. If the excited electron is not transferred within a sufficient time, it returns to its initial state (recombination) and releases the absorbed energy by transferring it to a new photon or as heat. Then the generated charged carries, which have opposite charges, are separated with the help of an electrical field (E-field) created by two electronically dissimilar materials.

In c-Si material, since it has a stable structure, charged particles move freely for a long distance within the material. This type of transport mechanism is called diffusion. However, due to the abundant defects in a-Si material, charge carriers cannot travel long distances. Therefore, charge carriers have shorter lifetimes in a-Si:H. Thus, an intrinsic layer with less defect density is placed between the materials that make up the E-field. This type of junction used for thin-film silicon solar cells is called p-i-n type junction.

In p-i-n type solar cells, absorption occurs in the intrinsic layer placed in the junction. Charge carriers in the junction move by a drift mechanism under the E-field. An intrinsic layer with fewer defects is needed to minimize the recombination and the number of carriers trapped in localized states. Charge carriers with a short lifetime must travel to the material side of which they are the majority carriers before they recombine. Therefore, this mechanism limits the thickness of the intrinsic layer, which affects the design and performance of the thin-film silicon solar cell.

According to their majority carrier in the material, the layers are called p- or n-type. In p-type material, the majority of carriers are positively charged carriers, whereas, for n-type, it is negatively charged carriers. The dominant transport mechanism is diffusion within these materials, where the diffusion length is too short for amorphous silicon material. As a result of low diffusion length, both p- and n-type material should be thin in the solar cell structure, and thus those layers do not contribute to absorption and photogeneration.

Hydrogenated amorphous silicon is most widely produced by the glow discharge method used in plasma-enhanced chemical vapor deposition (PECVD) systems. Doping is also possible within these systems, which allows ease of production. Both p- and n-type material are formed during deposition by doping with the corresponding gas precursor. Boron doping is done for obtaining p-type material with a B_2H_6 gas precursor, whereas phosphorus is used to obtain n-type material with a PH_3 gas precursor.

Since the layers of amorphous silicon thin-film are less than 1 micron in total in solar cell structure, they require a carrier. Due to high defect density, short-range order, and carrier transport mechanisms, the light should illuminate the whole structure of the amorphous silicon thin-film solar cell. This need means one of the carrier collection layers should be transparent, which is a transparent conductive oxide (TCO) arises. Glass substrates are used to support the entire structure with TCOs.

Glass substrates have not only the advantage of high light transmittance but also have the capability of the large-area production.

Large area production is accelerated with the use of flexible substrates. The thin-film silicon flexible electronics production goes back to the 1960s by thinning the crystal silicon wafer [4]. In the 1980s, the large area production of silicon flexible solar cells was established. The main drawback of thin-film a-Si:H solar cell is the light-induced degradation, also known as Staebler-Wronski degradation (SWE). When light is introduced to the system week, bonding between hydrogen atoms breaks, and separation in the bonding matrix occurs, leaving more dangling bonds in the system. The newly formed dangling bonds result in defects in the material [5]. As a result, single-junction solar cell efficiency reduction occurs, and the efficiency reaches a limit. To overcome this issue, Matsuda produced another form of silicon material: the transition from the amorphous phase to the crystalline phase, also called microcrystalline silicon (μc-Si) [6]. The importance of this material is that it is not affected by light-induced degradation.

The μc-Si material has a lower optical bandgap since it is at the edge of the crystalline phase. A lower bandgap means a thicker material need for absorption. Variation of materials with different bandgaps leads to higher light absorption from the solar spectrum. By arranging layer stacks, photons with different energies can be absorbed. Thus, the ability to adjust bandgaps leads to tandem structures. Combining the amorphous and microcrystalline silicon layers has high and more stable efficiency [7].

Bandgap variation can be obtained with other silicon alloys as well. In 1997, United Solar achieved 13% stable efficiency with silicon-germanium thin-film on stainless steel flexible solar cells [8]. The degradation of silicon-germanium [9] and silicon-carbon [10] alloys was reported by various research groups in the 1980s. Since there is degradation in the amorphous silicon and its alloys, it is essential to study the efficiency values in terms of stabilized values.

Lots of different types of flexible substrates are studied. Polyethylene terephthalate (PET); polyethylene naphthalate (PEN); polycarbonate (PC); polyimide (PI); polyethersulfone (PES); stainless steel (SS) are examples of flexible substrates. Each substrate has different advantages, which are discussed in section 1.3.

1.3 Flexible Substrates

Several organic polymer films have been used as a substrate, like Polyimide (PI), Polyethylene terephthalate (PET), and polyethylene naphthalene (PEN). Typically, plastic materials cannot sustain their forms and material properties under high process temperatures. However, they have the advantage of high optical transparency. On the contrary, the opaque substrates, which are flexible metal substrates, have the advantage of electrical conductivity. Also, these metal substrates are more durable at high process temperatures.

On the other hand, metal diffusion from substrate deteriorates the solar cell. Stainless steel and Titanium (Ti) metal are common opaque substrates used in literature. A comparison of different flexible substrates can be seen in Table 1.1.

Table 1.1 Comparison of different flexible substrates

	ADVANTAGE	**DISADVANTAGE**
PI	High process temperatures (T< 500ºC) It can be used for both configurations Available for R2R process	Low chemical resistance Need substrate holder
PET/PEN	High optical quality Suitable for electrical isolation for module formation Available for R2R process	Cannot sustain high temperature Glass transition temperatures are 80 and 120º C for PET and PEN, respectively
FLEXIBLE GLASS	Highly transparent High chemical resistance High process temperatures (T< 500ºC)	Need special care for handling (fragile)
STAINLESS STEEL	High process temperatures It can be used as a back reflector Available for R2R process	Metal diffusion into the cell Because of electrical conductivity, module formation is not available. Adhesion between layers

Substrate configuration is vital to determine the flexible substrate type. The types of flexible substrates can be divided into two groups: transparent and non-transparent. Transparent substrates such as plastics (PET/PEN) do not limit the structure, and they can be used underneath or on top of the whole structure. Flexibility to select the position of the substrate for cell structure leads to an advantage to choose the production sequence by the manufacturer. In order to allow the light to enter the system, non-transparent flexible substrates like stainless steel can only be used at the bottom of the layer stack, which leaves the substrate under the device structure, called substrate configuration. Alternatively, in the case of having substrate on top of the device structure where the light enters from the substrate side, the configuration is called superstrate [13]. Examples of both substrate and superstrate configurations can be seen in Figure 1.3.

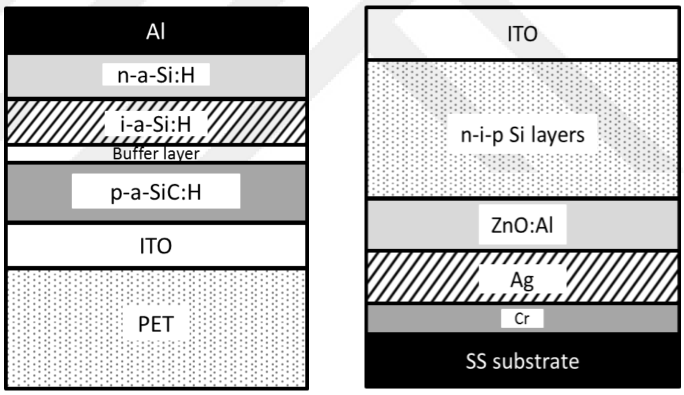

Figure 1.3. Schematics of a) superstrate configuration b) substrate configuration

In the substrate configuration, the substrate is generally opaque, as in the case of stainless steel, or transparent, as in the case of plastics. For superstrate orientation, light enters the device through the top contact, making the top contact transparent for incoming light, usually chosen from one of the TCOs. In the case of opaque substrates, for example, stainless steel can manage to stay undamaged up to temperatures of 500°C. On the contrary, having stainless steel substrates deteriorate the film quality because of metal diffusion to other layers during film deposition at high deposition temperatures. In order to overcome this problem, different barrier layers were studied by different research groups. Using Ti thin film as a barrier layer is another option, increasing the production cost for large-area applications.

If the substrate is transparent, they are often easily damaged by ultraviolet light, in the case of most plastics. In addition to that, plastic substrate usage limits the deposition temperature. The need for low-temperature processes for plastic substrates also reduces the production cost. The substrate foil would have to fulfill the three main requirements of high optical transparency, temperature compatibility, and cost-effectiveness in the superstrate configuration.

1.4 Light Management for Thin-Film Silicon Solar Cells

Loss mechanisms reduce cell performances in addition to the theoretical limits of solar cells. Light management is utilized to enhance the photon conversion of solar cells with less material. Photo-conversion is related to the absorption of a photon. If more photons are absorbed, more electrical energy is created. Thus, the performance strongly depends on the conversion of the photon into a charge carrier. In order to improve the photon conversion mechanism, (i) efficient conversion of the solar spectrum, (ii) enabling reflections between conductive layers to reduce optical losses (iii) entrapment of photons in absorber layers need to be developed.

Effective conversion of the solar spectrum can be done by bandgap arrangement. Most of the energetic photons in the solar spectrum can be absorbed by using low and high bandgap materials consecutively in the solar cell structure. In this way, the contribution to the generation of electrical energy increases. Thus, it can be achieved in thin-film silicon solar cells with a multi-junction solar cell structure formed by combining a-Si:H and µc-Si:H.

Optical loss in the structure is another way that affects the absorption of photons. Some photons reaching the surface are lost before reaching the absorber layer. Some of these photons are reflected from the surface, and some are absorbed by interacting with other layers. Both do not contribute to photon conversion. To maximize light in-coupling with the absorber layer, one should minimize front surface reflections and interactions with other layers.

Two methods are used to light in-coupling with the absorbing layer: applying the anti-reflective (AR) coating and surface texture. In a thin-film solar cell structure, highly reflective materials in the visible region of the solar spectrum are used since the light illuminates the entire structure. Since the reflectivity of these materials, which are usually glass or TCO, is very low, AR coating application is generally used in c-Si solar cells. However, it has also been used in some flexible plastic substrate applications. Surface texturing, which is achieved using micro and nano features, is a widely used application, especially in thin-film solar cells. The size and distribution of features determine the interaction with light. If the feature size of the structure is smaller than the wavelength of the incoming light, then the light progresses gradually through the structure, creating an effect similar to AR coating. The structures having greater feature size than the wavelength of the incident light reflected from a rough surface can reflect more than once, which means an increase in more possibility of absorption of the light.

If the light reaching the absorber layer stays in this layer, it increases the probability of photon absorption. Therefore, the essential purpose of light trapping is to extend the optical path traveled by the light in the structure. It is achieved by placing a layer in the light's exit direction with a reflective surface. Another way to extend the path traveled by the light is by deflecting it from the path it travels with the help of multiple reflections. A textured surface with dimensions smaller or equal to the wavelength of the light acts as an intermediate layer where total internal reflection occurs.

In the light of this information, within the scope of this thesis, studies have been carried out to obtain high-efficiency flexible solar cells in the PECVD system produced by a local company. With the data obtained in this direction, a single junction a-Si:H solar cell with novel textured structures was produced. It has been studied to develop the potential of the amorphous counterpart of tandem thin-film solar cells for use in flexible micromorph structures.

1.5 Aim of the work

The scope of the research presented in this thesis is to study low-temperature deposition and optimization of hydrogenated amorphous silicon deposition for flexible solar cells. Novel texturing of aluminum-doped zinc oxide (AZO) films is proposed and deposited on flexible substrates for photovoltaic applications. A comparative study of the effects of different laser wavelengths on texturing/patterning of AZO is discussed. In this work, it is objected

1. To optimize the flexible solar cell process by investigating the effects of deposition parameters on a-Si thin-film properties and cells.
2. To obtain surface texturing on transparent conductive oxide by a novel laser texturing done by direct laser writing.
3. To scale up from flexible cell to module with monolithically series-connection.

1.6 Outline of the thesis

Historical development of PV and thin-film solar cells, the details of the technology, and amorphous silicon materials are mentioned, and the thesis's motivation is given in Chapter 1. In the second chapter, thin film deposition and laser system used in this thesis, sample preparation techniques, thin film characterization, and theories are given. In Chapter 3, the optimization of the hydrogenated amorphous silicon for the thin film silicon solar cell and the results are discussed. In Chapter 4, optimization of the transparent conductive oxide (TCO) layer is discussed. Results of optimization are given. In addition, in this chapter, the results of TCO layer texturing via laser processes are given. In Chapter 5, the results of thin film flexible solar cells, which are deposition with optimized layers, are discussed. Finally, Chapter 6 gives the summary of the thesis work.

CHAPTER 2

EXPERIMENTAL

Active and conductive layers of a solar cell are produced and characterized by different production methods. This chapter describes the production and characterization systems involved in this study. System description, sample preparation, thin film, and device characterization are discussed.

2.1 System Description

2.1.1 PECVD Cluster System

Thin film deposition processes conducted in this study are produced in a cluster system. Each layer of silicon thin film and transparent conductive oxide layers that combine thin film silicon solar cells are produced in this system called GünEr, produced by Turkish company VAKSİS Corp.

The cluster system consists of three different capacitively coupled plasma (CCP) chambers, one inductively coupled plasma (ICP) chamber, and one magnetron sputtering chamber having two sources connected with a central transfer chamber. A load-lock chamber is also attached to the system to transfer samples without breaking the vacuum during successive depositions. The Chamber configuration of the cluster system can be seen in Figure 2.1 and Figure 2.2.

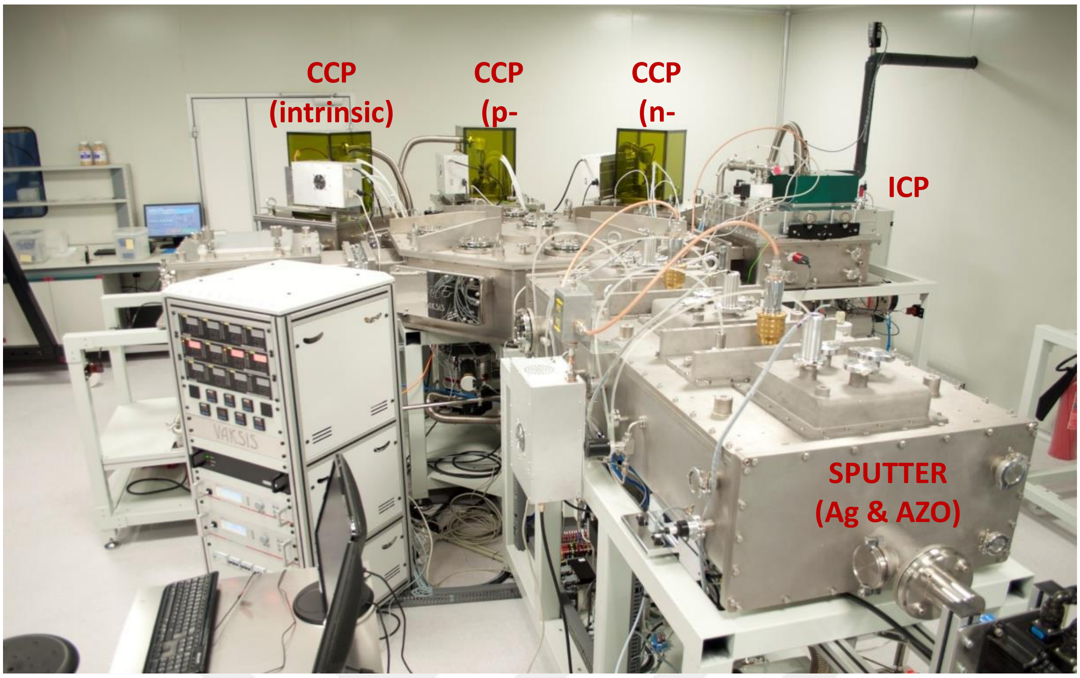

Figure 2.1. Image of the thin film deposition cluster system GünEr

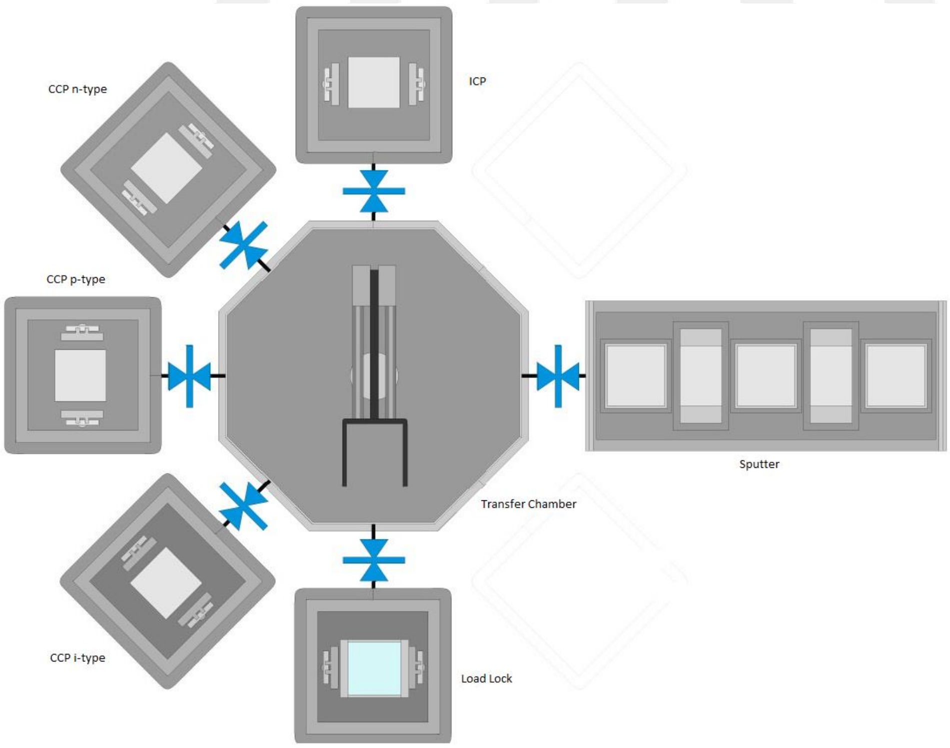

Figure 2.2. Schematics of the GünEr System

All the gas flows are controlled via digital mass flow controllers. Each chamber has substrate heaters to control the deposition temperature. CCP chambers are controlled by a power generator operating at 13.56 MHz radio frequency (RF), having a maximum power of 600 Watt, and ICP and magnetron sputtering chambers are controlled with a similar RF power generator having a maximum power of 5000 Watt. A computer program automates control of these support systems. CCP, ICP, and Sputter chambers are always kept at vacuum level, and the base pressure of these chambers is $1x10^{-6}$ Torr. Chambers are connected to an exhaust system to burn extra gas leaving the system after deposition.

Both CCP and ICP chambers are operated to produce intrinsic or doped silicon layers. Silane (SiH_4) gas is used as a silicon source in the deposition process. Both %10 silane diluted in hydrogen and pure silane gas sources are used throughout this study for amorphous silicon thin film deposition. Doping of silicon layers is provided with diborane (B2H6) and phosphine (PH3) gasses connected to the CCP-p and CCP-n chambers, respectively. Apart from doping gasses, other common process gasses such as helium (He), nitrogen trifluoride (NF_3), ammonia (NH_3), methane (CH_4), hydrogen (H_2), nitrogen (N_2) are connected to the system for different applications. He and NF_3 are used for chamber cleaning. After each deposition, a cleaning recipe is applied with such gasses. H_2 gas is used for Silane dilution, and N_2 gas is used for vacuum breaking purposes.

The sputtering chamber has gas inlets of argon (Ar), oxygen (O_2) for process, and N_2 for vacuum-breaking purposes. Sputter target materials used in the system are Silver (Ag) and Aluminum doped Zinc Oxide (AZO). The sputtering chamber has two sputtering targets of 10x30 cm^2. A longitudinal chamber design for the sputter chamber is shown in Figure 2.2. This design provides large-area production with high thickness uniformity. In order to ensure thickness uniformity, samples move back and forth under the target material. Different film thicknesses are obtained by repeating this back-and-forth movement and controlling the movement speed.

GünEr system is designed to deposit on glass samples with a maximum of 25x25 cm^2. Samples smaller than the maximum size are placed on top of 25x25 cm^2 glass and secured with vacuum-compatible tape or any other small sample holder. Samples are transferred to the process chambers through the load-lock and transfer chambers. Samples are placed into the load-lock chamber with an aluminum sample holder and transferred with a robotic arm placed in the transfer chamber.

The cluster system has the advantage of producing each p-i-n layer separately, reducing contamination of impurity atoms. Layers can also be produced in the ICP chamber as well.

2.1.2 Laser System

The laser source used throughout this study is HIPPO Spectra-Physics, a diode-pumped solid-state (DPSS) Q-switched laser. This laser system is designed for solar cell scribing, crystal silicon (c-Si) edge isolation, semiconductor wafer dicing, glass marking, micromachining, and material processing. The laser system operates at three different wavelengths, which are infrared (IR-1064 nm), green (532 nm), and ultraviolet (UV-355 nm).

The laser beam operates at TEM_{00} spatial mode with less than 15 ns pulse at the width of 50 kHz. The repetition rate of the laser pulse can be varied from 15 kHz to 300 kHz. Laser power at 50 kHz is 17 W, 11 W, and 5 W for wavelengths in infrared (IR), green and ultra-violet (UV), respectively. HIPPO Spectra-Physics laser uses two crystals that can be supplied from 20 A to 38 A current. The power of the laser can be controlled through the current passing through the diode, which pumps the crystals.

As seen in Figure 2.3, both sample and the focusing lenses are placed on two different motor-controlled stages. The sample moves in the vertical axis during operation, whereas the focused laser beam moves in the horizontal axis controlled by the software. Only the speed of the motor located on the horizontal axis can be controlled, and it can be varied from 1 mm/sec to 600 mm/sec.

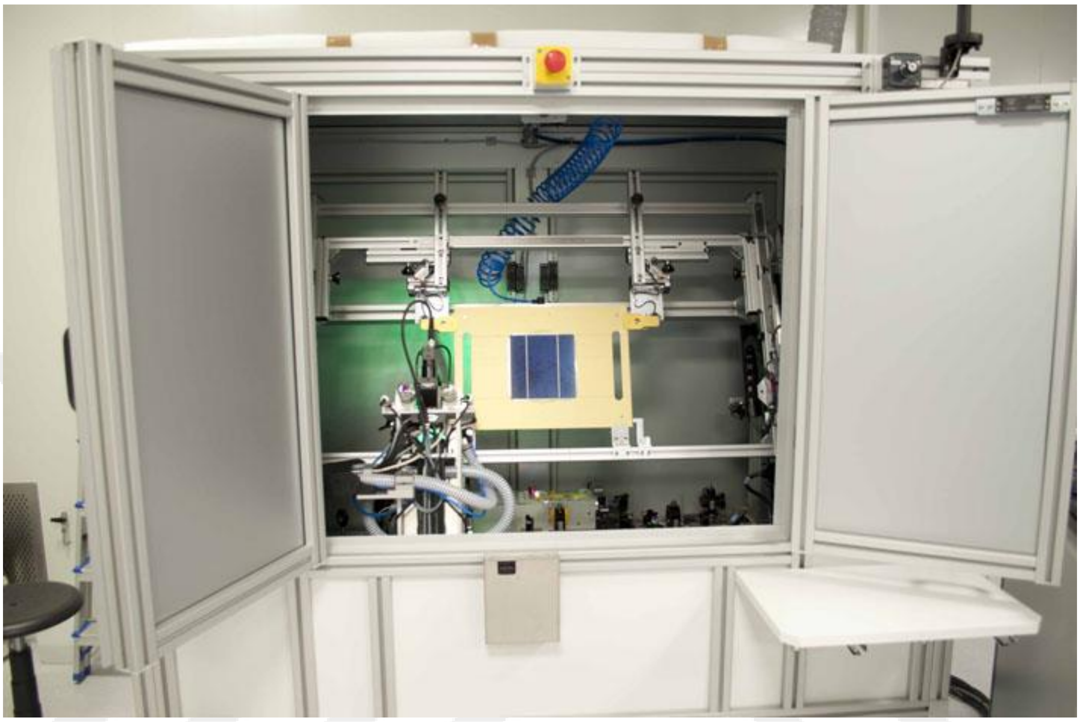

Figure 2.3. Image of the laser scribing system

Software of the laser system provides to change the working modes of the laser, which means the laser can move on a straight line (scribing mode), can shoot at specific points (drilling mode), or can follow a trace (edge isolation mode).

2.2 Sample Preparation

The cluster system has the advantage of depositing 25x25 cm^2 samples to obtain thin film solar cells on flexible substrates; each layer is required to be characterized separately. Samples smaller than 25x25 cm^2 are preferred at the characterization phase of the study. Several small-sized samples are deposited in a single run, and each sample is characterized by a different method. In addition, different substrates are used to optimize process parameters to reach the best device performance.

Commonly used flexible substrates consist of plastic materials. The process temperature of high transparent plastic materials does not exceed 100-150℃. This limitation plays an essential role in determining process parameters where the choice of flexible substrate depends on process parameters. Low deposition temperature is required to maintain the form of the flexible plastic substrate. Substrates obtained from DuPont Teijin Films are used as flexible substrates that are uncoated polyethylene terephthalate (PET). There is also a new generation of ultra-thin flexible glass that allows production at high temperatures (up to 500℃). Ultra-thin (100 μm thick) flexible glass substrates used in this study are provided by the Schott Glass Company.

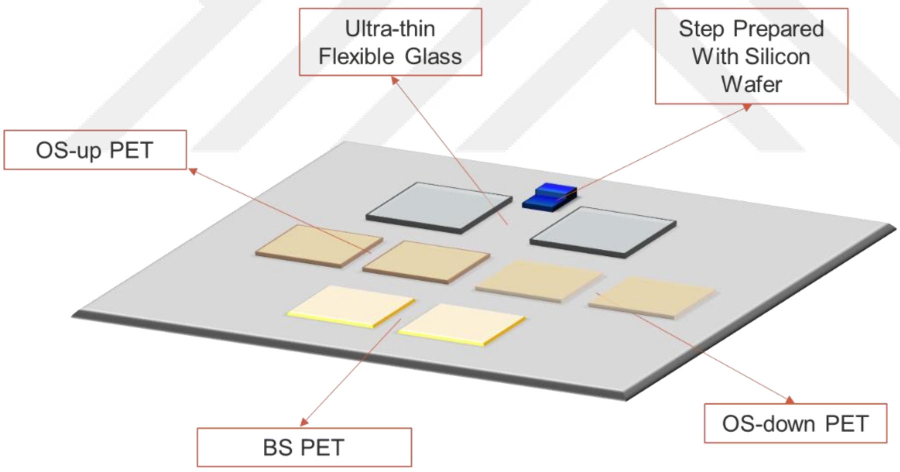

Figure 2.4. Sample orientation during depositions for substrate comparison

Two different types of PET samples from DuPont (500 gauge Melinex STCH11 [14] and Melinex STCH12 [15]) and one sample of ultra-thin flexible glass (D 263® T eco [16]) from Schott are placed in each deposition for flexible substrate comparison. Manufacturer treats surfaces of the PET samples for adhesion which is called *"adhesion promotion"* by DuPont. One sample type has this promotion only on one surface, and the other has it on both surfaces. Because of this distinction, three PET samples are placed for each deposition. Both side adhesive applied PET (BS PET), one side adhesive applied PET with adhesive facing up (OS-up PET), and one side adhesive applied PET with adhesive facing down (OS-down PET). Samples and their orientation during deposition are presented in Figure 2.4.

Several suitable samples are prepared to meet the measurement criteria for efficiently characterizing each deposited film. Samples are arranged and placed in the middle of the sample holder, as shown in Figure 2.5. They are placed as close as possible to reduce uniformity variations in the large area. Polished c-Si wafer, transparent conductive oxide (TCO) coated substrates, and uncoated substrates are the samples used for characterization.

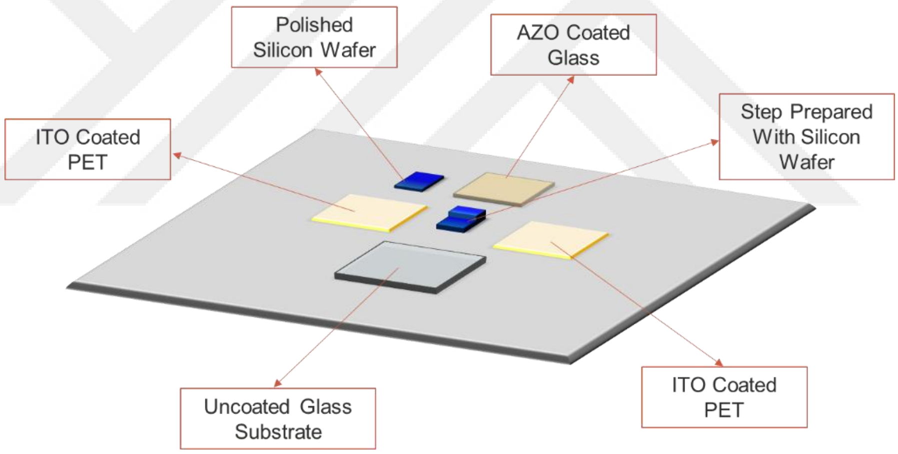

Figure 2.5. Sample orientation during depositions for characterization

Substrates are pre-cleaned by the supplier; thus, prior to deposition, substrates are only blown by nitrogen gas to remove any possible dust residue from the surface. Samples that are cut into small pieces are cleaned with ultrasonic cleaners. In addition to ultrasonic cleaning, standard cleaning (SC) is applied [17]. First, standard cleaning (SC-1), also called RCA1, is applied then the second part of standard cleaning (SC-2), also called RCA2, is applied. After cleaning, rinsed samples are N_2 blown and stored. Si wafers used for characterization are cleaned by hydrofluoric acid (HF) solution prior to deposition to remove the native oxide layer on silicon. Glass substrates used in these experiments were cleaned by RCA1 or piranha procedures. After RCA2 cleaning, samples are rinsed, and hydrofluoric acid (HF) cleaning is done for silicon wafers. No hydrofluoric acid (HF) cleaning is applied after RCA2 cleaning for glass samples.

2.3 Thin Film Characterization

In this thesis, studies of single-junction flexible thin film silicon solar cell production are carried out. Due to their nature, solar cells consist of multi-layered thin film stacks. It is aimed to produce the most efficient flexible solar cell; thus, each layer is produced and examined separately, and production parameters are optimized.

The structure of flexible solar cells produced is seen in Figure 2.6. AZO layer is used as a transparent conductive oxide layer, hydrogenated amorphous silicon (a-Si: H) is used as p-i-n junction layers, and the silver layer is used as a back reflector and rear contact. Each layer is examined in terms of structural, optical, and electrical properties, as described below.

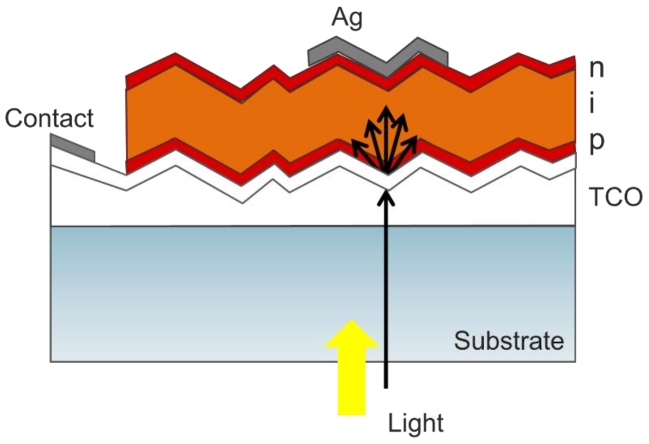

Figure 2.6. Schematic of superstrate type thin film solar cell structure

In this study, two different thickness measurement method is used. The first method is measurement via profilometer by DEKTAK. Thickness measurements are gathered from steps prepared with polished c-Si wafers. The second method is spectroscopic ellipsometer measurement done directly from the glass substrate. Hydrogen content and microstructure factor can be obtained via Fourier Transform Infrared Spectroscopy (FTIR) measurement. The sample used for this analysis is a polished c-Si wafer. In addition, FTIR measurements are used to analyze the bond structure of the deposited film. Raman measurements are taken from the surface of the material; thus, any sample is appropriate for this measurement. A spectrophotometer in the range of ultraviolet and visible (UV-VIS) spectrum is used to obtain the optical bandgap of each layer. UV-VIS measurement is conducted from films deposited on uncoated substrate samples. Electrical characterization is done to determine the conductivity of each layer in the device. For electrical characterization, TCO-coated samples were used for the non-conductive films. In order to analyze the current-voltage characteristics of the films, aluminum is evaporated with a point-contact configuration. The films that are already conductive are investigated by the four-point probe method. The device structure is examined using a scanning electron microscope (SEM) to have detailed information about the layer.

2.3.1 Structural Analysis

Optimizations of the films are achieved through varying process parameters to reach the demands of a proper conductive layer for thin film silicon solar cell applications. X-ray diffraction (XRD) spectroscopy involves structural analysis to determine the crystallinity of the layers is done by X-ray diffraction (XRD) spectroscopy. Structural analysis is also done on TCO layers to determine the microstructure of the films. Throughout this study, silicon layers are used in the amorphous phase; thus, they are checked for validation.

Structural Analysis of a-Si:H

Since hydrogen is used to passivate the dangling bonds of amorphous silicon, it is crucial to analyze the hydrogen content in the material. Hydrogen content is a measure of control of defect density in the material. Hydrogen content characterization is done by analyzing the IR spectrum absorption peaks. FTIR measurement is done to analyze these peaks.

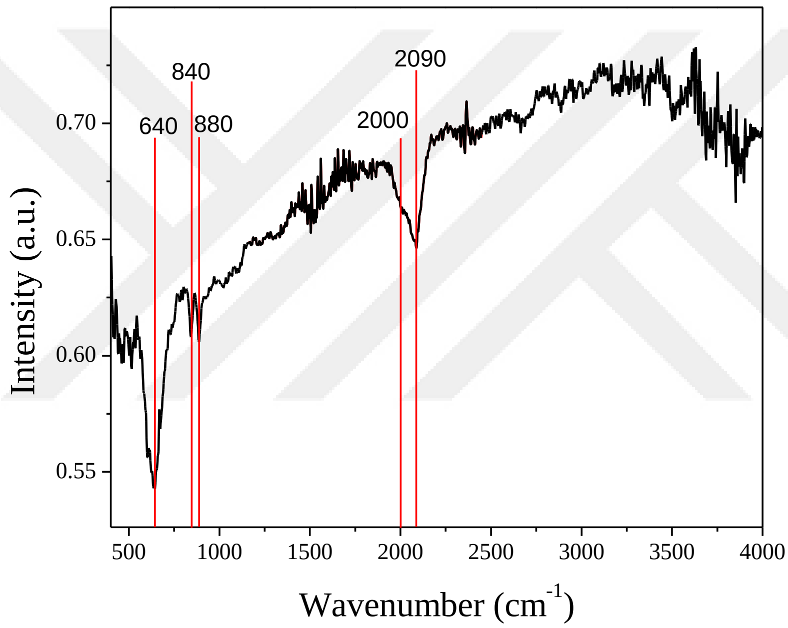

Figure 2.7. IR spectrum of a-Si:H layer deposited in GünEr

Different absorption peaks are observed in the IR spectrum of a-Si:H (see Figure 2.7). The first peak is at 640 cm^{-1}, the second and third is a doublet at 840-880 cm^{-1}, and the fourth and fifth are absorption peaks at 2000 cm^{-1} and 2090 cm^{-1}. The first peak comes from the rocking-wagging mode of hydrogen to silicon (Si-H) bond. Therefore, this peak is used to determine the hydrogen content of the film. The second and third peaks result from vibrational modes of SiH_2 and mainly occur at low-temperature depositions. The fourth and fifth peaks combine high stretching (HSM) and low stretching modes (LSM).

Equation 1 (Eqn.1) is used to calculate the hydrogen content in the films [18]. Only the bending mode peak located around 640 cm-1 is used in this calculation. The Peak Fit software is used for the extraction, sectioning, and baseline correction.

$$C_H = \frac{A_w}{N_{Si}} \int_{\nu_{r/w}} \frac{\alpha(\nu)}{\nu} d\nu \approx \frac{A_w}{N_{Si}} \sum_{\nu_{r/w}} \frac{\alpha(\nu)}{\nu} \triangle \qquad \text{Eqn.1}$$

where $\alpha(\nu)$ is the absorption coefficient at the wavenumber ν, $\nu_{r/w}$ stands for the rocking-wagging bands around 640 cm^{-1}, $A_w = 1.6 \times 10^{19}$ cm^{-2} is the proportionality constant and $N_{Si} = 5 \times 10^{22}$ cm^{-3} is the atomic density of pure silicon [18].

The absorption coefficient in units of cm^{-1} is related to the transmission as given in Eqn.2,

$$\alpha = \frac{-\log(T)}{d} \qquad \text{Eqn.2}$$

where d is the thickness of the film.

After substituting the absorption coefficient, the proportionality constant, and atomic density of pure silicon into Eqn.1, the resulting equation becomes as given in Eqn.3,

$$C_H \approx \frac{6400}{d\,[nm]} \sum_{\nu_{r/w}} \frac{-\log(T)}{\nu} \qquad \text{Eqn.3}$$

Another analysis can be done using stretching mode absorption peaks. The microstructure factor is determined from HSM and LSM absorption peaks. A peak around 2000 cm^{-1} reflects isolated Si−H bonds. A peak in the range of 2070-2100 cm^{-1} reflects Si−H bonds at the interfaces, voids, SiH_2, or SiH_3 bonds. LSM and HSM peaks are obtained by deconvolution of the peak appearing in the FTIR spectrum. Microstructure factor (r) is calculated from the Eqn.4 [19],

$$r = \frac{I_{2090}}{(I_{2090} + I_{2000})} \quad \text{Eqn.4}$$

where I_{2000} and I_{2090} is the intensity of the FTIR signal.

Device quality a-Si:H contains less than 10 atomic % of hydrogen and is characterized by r<0.25. r should be around 0.2.

Structural Analysis of AZO

AZO crystal structure is hexagonal wurtzite as represented in Figure 2.8 [20] with lattice constants of a=3.24 Ǻ and c=5.19Ǻ [21].

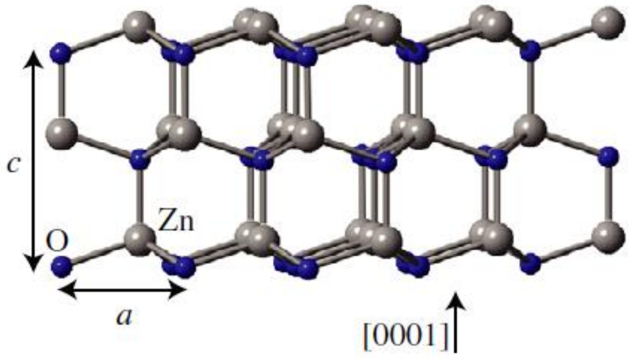

Figure 2.8. Wurtzite structure of ZnO [20]

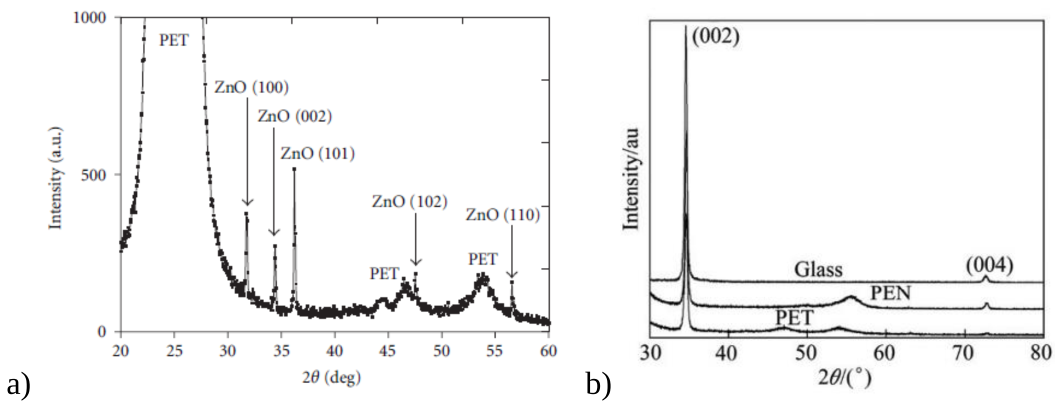

Figure 2.9. XRD patterns of ZnO thin films on a) PET b) compared with other substrates [22] [23]

A typical XRD spectrum for AZO thin films deposited on PET substrate can be seen in Figure 2.9 [22], [23]. Similar peeks are observed in our films and reported in the following chapters.

The presence of the intense (002) peak (and also (004)) implies the grains are strongly c-axis oriented, which means columnar growth (perpendicular to the substrate) of the film [24]. (002) peak positions and Full Width at Half Maximum (FWHM) values are determined by using Peak Fit software. (002) position shift to higher values implies compressive stress formation on the films (shift to lower values means tensile stress) [25], [26]. An increase in (002) peak FWHM and broadening of (002) peak, corresponds to the decrease in grain size. When grain size decrease, grain boundary increases, which means the number of scattering centers for carriers increases and Hall mobility decreases [27], [28].

The grain size (t) can be calculated with the Scherrer formula given in Eqn.5;

$$t = \frac{0.9\lambda}{B\ cos\theta} \qquad \text{Eqn.5}$$

Where λ is the X-Ray wavelength (λ=0.154056 nm), B is the corrected peak width, and θ is the Bragg angle in radians [29].

2.3.2 Electrical Analysis

Electrical analysis of layers is done according to their conductivity level. TCO layers are characterized by the four-point probe method. The resistivity of the film is simply calculated as the product of sheet resistance and film thickness.

Electrical characterization of a-Si:H layers is done via I-V measurement to determine the conductivity of the layer. Measurement is done from aluminum (Al) metal contacts evaporated on samples. 200 nm Al is thermally evaporated on samples by using a shadow mask. Different shadow mask designs and configurations are used and discussed below.

Intrinsic (undoped) a-Si:H layers are first characterized via the point contact configuration, and the design is shown in Figure 2.10. In this study, both point contact and lateral contact mask designs are used for a-Si:H layers. Radius dimensions are given in millimeters.

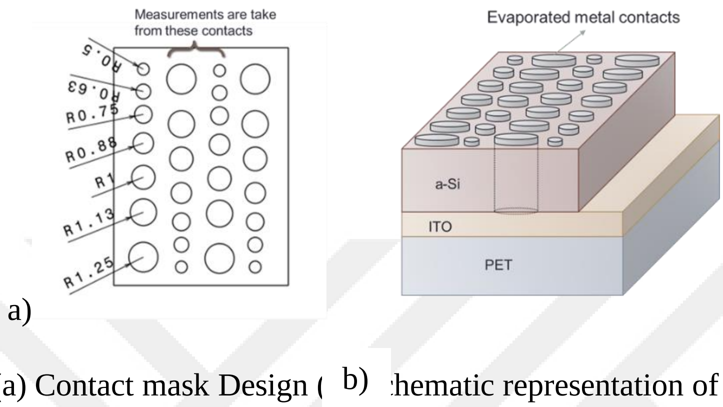

Figure 2.10. (a) Contact mask Design (b) Schematic representation of the point contact configuration

Since the conductivity relation is associated with the contact geometry, relations are given according to this contact configuration. Conductivity relation is given Eqn.6 is used for calculation. Dark conductivity is determined inverse of resistivity (ρ), which is defined by the formula which is used for point contacts;

$$\sigma_d = \frac{1}{\rho} = \frac{t}{AR} = \frac{I}{V}\frac{t}{A} \qquad \text{Eqn.6}$$

where t is the thickness of the film, R is the resistance of the film, and A is the contact area. Resistance of the film is determined by the I-V measurement. The inverse of the slope of the I-V measurement will give the resistance value.

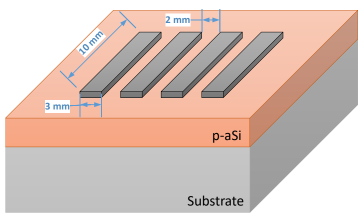

Figure 2.11. Schematic of the contact mask design for lateral contact pads

Besides point contact configuration, lateral contract configuration is also used for the electrical analysis of the films. Further characterization of electrical analysis is conducted through I-V measurements. A lateral contact mask design is used for this purpose, and a schematic of the mask design is seen in Figure 2.11.

Dark and photo conductivity is determined inverse of resistivity (ρ), which is defined by the formula given in Eqn.7, which is used for point contacts;

$$\sigma = \frac{1}{\rho} = \frac{g}{AR} = \frac{I}{V}\frac{g}{Lt} \qquad \text{Eqn.7}$$

where is t is the thickness of the film, R is the resistance of the film, A is the area that current passes, g is the gap between the contact strips, and L is the length of the contact strips. Resistance of the film is determined by I-V measurement. The inverse of the slope of the I-V measurement will give the resistance value.

2.3.3 Optical Analysis

The transparent conductive oxide (TCO) layer is textured for light management. An optical analysis is used for bandgap determination and surface characterization. For each thin film, the layer bandgap is determined from transmission measurement.

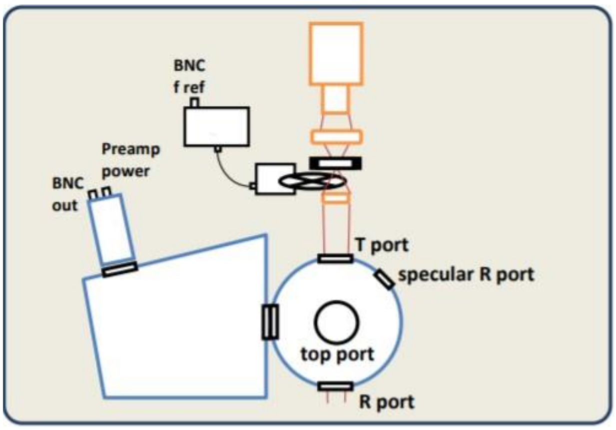

Figure 2.12. Schematics of the transmission measurement setup

Optical responses of the obtained textures, such as total transmittance and haze in transmittance, are obtained using an integrating sphere system. Transmission measurements are done with an in-house optical setup containing an integrating sphere, a monochromator, and a silicon detector, as seen in Figure 2.12.

A background signal is checked and measured as dark measurement (Dark) by leaving entrance and exit ports open during measurement. A reference measurement is done with a calibration disk called $BaSO_4$, which has known reflectance by placing the disk at the exit port. In order to measure the total transmission (T) sample is placed at the entrance port while the calibration disk remains at the exit port. Total transmittance can be calculated as follows (see Eqn.8).

$$\text{Total transmittance} = T/Ref \qquad \text{Eqn.8}$$

In order to measure haze, total transmission measurement is repeated with the exit port of the sphere empty. Let this signal be called T* as stated in Eqn.9 and Eqn.10.

$$\text{Diffuse transmittance} = [T^* - Dark \times (T/Ref)]/Ref \qquad \text{Eqn.9}$$

$$\text{Diffuse transmittance} = T^*/T \qquad \text{Eqn.10}$$

Another optical analysis for bandgap measurement is done from the transmission measurement obtained from the UV-VIS system. Transmissivity of the films is compared through substrates and deposition parameters and reported in the results section. Transmission data is also used to investigate the bandgap of the films. Determination of bandgap is done by Tauc plot analysis discussed below.

Band Gap Determination of AZO

Tauc's optical bandgap relation for direct bandgap material such as AZO is given in Eqn.11,

$$(\alpha h\nu)^2 = A(h\nu - E_g) \quad \text{Eqn.11}$$

where α is the absorption coefficient and is obtained from Eqn.12,

$$\alpha(\lambda) = \frac{1}{d}\ln(\frac{1}{T(\lambda)}) \quad \text{Eqn.12}$$

where T is transmission value, d is the film thickness in nm, E_g is optical bandgap, and ν is wavenumber in cm^{-1}. This value might be adjusted with different doping atoms and doping concentrations.

Band Gap Determination of a-Si:H

Tauc's optical bandgap relation for amorphous silicon is given in Eqn.13,

$$(\alpha h\nu)^{1/2} = A(h\nu - E_g) \quad \text{Eqn.13}$$

where α is the absorption coefficient and is obtained from Eqn.12,

2.4 Device Characterization

The operating regime of the solar cell is 0 – V_{OC}, as seen in Figure 2.13.

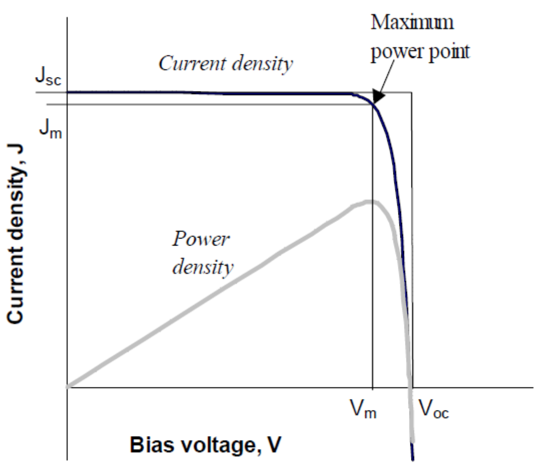

Figure 2.13. Schematic of characteristic J-V curve.

The cell power density is given by;

$$P = J \qquad \text{Eqn.14}$$

P reaches a maximum at a V_m and J_m, known as the maximum power point. The fill factor describes the squareness of the J-V curve and is formulated as;

$$FF = \frac{J_m V_m}{J_{sc} V_{oc}} \qquad \text{Eqn.15}$$

The efficiency, η, of the cell is the power density delivered at the operating conditions divided by the coming incident light power density, P_s.

$$\eta = \frac{J_m V_m}{P_s} \qquad \text{Eqn.16}$$

It can be expressed in terms of FF, V_{OC}, and J_{SC} as;

$$\eta = \frac{J_{sc} V_{oc} FF}{P_s} \qquad \text{Eqn.17}$$

These four quantities (FF, V_{OC}, J_{SC}, η) are the critical performance characteristics of the cell.

CHAPTER 3

OPTIMIZATION OF AMORPHOUS SILICON

This chapter gives the optimization studies of hydrogenated amorphous silicon (a-Si:H) layers used in single junction amorphous silicon thin film solar cells. Due to the nature of thin film amorphous silicon solar cells, it consists of three different types of a-Si:H layers. Intrinsic (undoped) and Boron (B) were doped for p-type, and Phosphorus (P) was doped for n-type silicon layers. The optimization is achieved by varying process parameters of each layer to reach the requirements for thin film silicon solar cell applications.

Deposition power, deposition pressure, deposition temperature, and deposition gas ratios are the variables for the cluster system used in GUNAM facilities. In order to reach device-quality a-Si:H layers for thin film silicon solar cells, parameters are carefully studied. Layers, i-layer, p-layer, and n-layer are characterized separately. Layer characterization includes electrical analysis to obtain information about the light and dark conductivity ratio through I-V measurement to identify the change in production parameters. The film thickness is determined by measuring the step height with a profiler directly from the sample surface. The effect of each process parameter on film quality is discussed, and the results are given in the following sections.

3.1 Optimization of Intrinsic Amorphous Silicon (i-aSi:H) Layer

Unlike crystal silicon (c-Si) in amorphous silicon (a-Si) material, atoms are not well-oriented, and long-range order is not found in its structure. Therefore, amorphous silicon forms a continuous random network. Covalently bonded silicon (Si) atoms in the a-Si structure have different bond lengths and angles. These non-identical bonds form broken and weak bonds that are considered as defects in the material throughout the continuous random network.

By the nature of this disordered structure of a-Si, some Si atoms are bonded to three Si atoms instead of four Si atoms. This missing bond is called a dangling bond. Dangling bonds can be passivated by hydrogen atoms. Hydrogen passivated amorphous silicon thin films are called hydrogenated amorphous silicon. Passivated dangling bonds are not considered defects; thus, it is essential to determine hydrogen incorporated in silicon films. The hydrogen content is calculated to characterize a-Si:H films. Higher than 10 atomic % is considered disruptive to the film quality [30].

Amorphous silicon is produced by glow discharge deposition methods [31]. Hydrogen inclusion in the silicon film is done by plasma-enhanced chemical vapor deposition (PECVD). During deposition with gas precursors, silicon thin film is obtained as alloyed with hydrogen [11]. Silane (SiH_4) is the primary gas precursor during deposition. Silane gas exists in different forms as hydrogen diluted silane or pure silane. In this study, both 10% Hydrogen (H_2) diluted SiH_4 and pure SiH_4 is used as main gas precursors for silicon deposition. Silicone layers are also doped with other gas precursors within the same system. Doped a-Si:H has two or three orders of greater defect density than intrinsic a-Si:H [32].

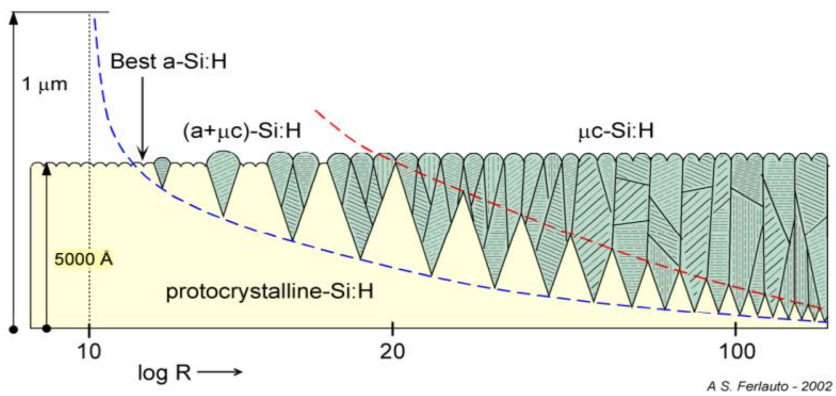

Figure 3.1 Schematic representation of amorphous to microcrystalline silicon growth regime

Given the nature of gas precursor silane, the silicon layer deposited from pure silane is also hydrogenated. In addition to passivating the dangling bonds, hydrogen plays an important role in controlling film transition from amorphous to a crystalline structure. This transition is dependent on the ratio of H_2 to SiH_4 and the film thickness. Here, this ratio is defined as R = [H_2] / [SiH_4]. When this ratio is R<10, a transition does not occur even if at higher thicknesses; however, for the R>10, a transition can occur depending on the film thickness and the substrate type, as seen in Figure 3.1 [33]. In this study, according to this discussion and the schematic given in Figure 3.1, the intrinsic layer deposited is arranged to be on the best a-Si:H line.

Since this thesis aims to deposit thin film silicon solar cells onto flexible substrates, different types of flexible substrates are used throughout this study. The first choice of the flexible substrate is a transparent conductive oxide (TCO) coated PET. It is a commercially available substrate with 60 Ω/sq sheet resistance. Later uncoated PET and ultra-thin flexible glass substrates are used. Since all the samples are transparent to visible light, superstrate configuration is preferred for deposition sequence.

3.1.1 i-aSi:H Deposition Parameters

In this thesis, the most widely used radio frequency plasma enhanced chemical vapor (rf-PECVD) deposition method is studied to produce hydrogenated amorphous silicon. The aim is to optimize the process parameters of the system GünEr. PECVD process parameters that will affect the i-aSi:H layer is plasma frequency (F), plasma power (Pw.), deposition pressure (Pr.), and gas flow rate (Flw.), H_2/SiH_4 feed gas molar ratio (R), substrate temperature (T), and the distance between the substrate and the plasma source (d). The design of the system GünEr limits the two of the process parameters. The first limitation is the plasma frequency fixed to radiofrequency (RF) at 13.56 MHz. The second limitation is the separation of anode and cathode which is the distance between the substrate and the cathode fixed at 2 cm.

First experiments are designed to optimize the i-aSi:H, 10% SiH_4 diluted in an H_2 gas mixture is used; thus, the ratio R is fixed to 9. The experiments are designed to correlate the parameters of Pw, Pr, and T. As described in the previous chapter, the system GünEr has separate deposition chambers for all three a-Si:H layers. The configuration of these chambers is identical. The results of this optimization set are received for the other two doping chambers. However, during this study system configuration of the intrinsic chamber is changed, and the optimized parameters are re-tested with the second design of experiments. In addition, experiments are done with different R ratios and with higher process temperatures. R ratio variation is done to examine the effect of the R ratio on the i-aSi:H layer. During this study, pure silane is used for a-Si:H depositions. Since temperatures higher than 150℃ are needed to produce the doped layers, the intrinsic silicon layer is optimized again at a higher temperature. The need for higher process temperatures leads the study to work with ultra-thin flexible glass substrates.

3.1.2 i-aSi:H Design of Experiments (i-DOE)

The first design of the experiment (i-DOE-1) aims to associate plasma power, deposition pressure, and substrate temperature. The effect of the change of these parameters is investigated. In order to correlate these parameters, initial experiments are designed as two-level experiments. Parameter ranges are given in Table 3.1.

Table 3.1 Process parameters and values (i-DOE-1)

	LEVEL 1	LEVEL 2
Plasma Power (Watt)	50	150
Deposition Pressure (Torr)	0.5	1
Substrate Temperature (°C)	50	100
SiH_4 Flow Rate (sccm)	FIXED (350)	
R = $[H_2]$ / $[SiH_4]$	9	

For simplicity, the SiH_4 flow rate is also fixed to 350 sccm. This flow rate is preferred to obtain a stable plasma for all other variables during the deposition. Plasma power density is varied from 80 mW/cm^2 to 240 mW/cm^2.The experiment set, which is prepared with two-level variables, consists of ***11 experiments***, and 2^3 experiments, including 3 repeat tests.

In the thin film coating system-GünEr, other studies such as a-Si passivation are carried out besides thin film solar cell deposition. Production problems encountered in these studies were solved by changing the system design. The previous experiments for the intrinsic layer were deposited in the old chamber design, which is represented in Figure 3.2 a). In the deposition chamber of the intrinsic layer (i-chamber), the substrate is placed at the bottom of the reactor. System i-chamber layer is changed to the diode type reactor ***with plasma box*** as seen in Figure 3.2 b). The plasma box enables to eliminate of contaminations and to obtain more uniform films.

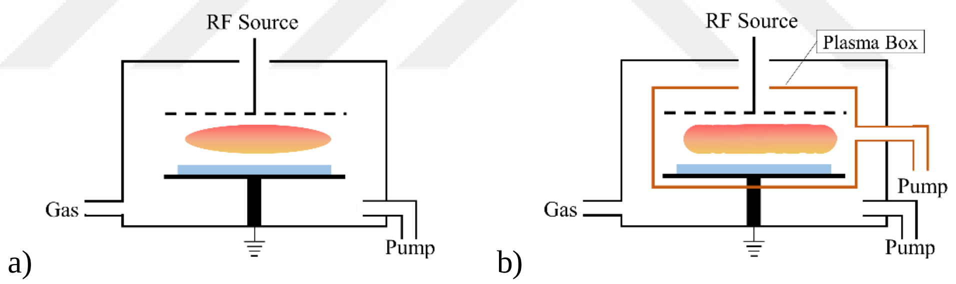

Figure 3.2 a) Standard diode type PECVD b) Diode type PECVD with plasma box

Along with this new cluster system design, a new experiment set is planned for intrinsic layer optimization. In addition, the production temperature is increased according to the results obtained from the doping studies. Therefore, the temperature value is increased for the new experiment set and arranged for the intrinsic layer. Deposition parameters, levels, and values are given in Table 3.2.

These experiments are performed with pure silane gas as a precursor for deposition. The films that are deposited at a higher R-value result in film delamination. Thin film deformations can be caused by pinholes, oil/dirt on the substrate, and process parameters. The source of the problem is investigated by reproducing the film under different conditions. Thus, five-level H_2 dilutions are tested. However, the film delamination continued in all iterations, which shows that process parameters are the leading cause of delamination.

Table 3.2 Intrinsic layer deposition parameters with plasma box reactor (i-DOE-2)

Parameters	**Values**
Deposition Power	50 W
Deposition Pressure	1 mTorr
Temperature	175°C
$R=[H_2]/[SiH_4]$	4 – 9 – 14 – 19 – 24

The final set of experiments (i-DOE-3), which are depositions of i-layer with plasma box design in i-chamber, is planned by reducing the deposition power. These experiments are prepared for R=9 and R=14 with reduced deposition power. Deposition power is reduced to 30 W to solve the pealing problem of the intrinsic layer. The effect of R on thin film properties is analyzed with the new experiments. Deposition parameters, levels, and values are given in Table 3.3. The plasma power density of i-DOE-3 is 48 mW/cm^2.

Table 3.3 Intrinsic layer deposition parameters with plasma box reactor (i-DOE-3)

Parameters	**Values**
Deposition Power	50 W
Deposition Pressure	1 mTorr
Temperature	175°C
$R=[H_2]/[SiH_4]$	9 – 14

3.1.3 Results and Discussion of Intrinsic a-Si:H Layer Optimization

As discussed in the previous section, all samples are analyzed to characterize different film properties. The following methods are used to examine thin films produced at GünEr:

- *Microscope:* for visual inspection
- *Profilometer:* to determine thicknesses of films
- *FTIR:* for chemical analysis
- *Raman:* to determine crystallinity
- *UV-VIS:* to determine bandgap
- *I-V measurement:* for layer characterization
- *SEM:* for structural analysis

Sample photographs from i-DOE-1 of run3 (PET sample) are presented in Figure 3.3 (a). All samples are visually inspected for pinholes and surface defects. At the bottom of the sample, a Teflon tape is wrapped to obtain an electrical contact opening after the process for I-V measurement. A microscope image of the same sample is given in Figure 3.3 (b). The surface of the samples is smooth and clean (Black spots at the edges of the picture are caused by the dirt coming from the objective of the microscope). All the samples other than the delaminated ones are the same as this microscope image shown in Figure 3.3 (a).

Examples of delaminated samples are shown in Figure 3.3 (c) and (d). A microscope image of a telephone cord blister is seen in Figure 3.3 (b). This type of blister occurs when residual stress is present [34]. In this case, the source of the residual stress is the substrate itself. Due to deposition parameters, high substrate bending occurred, and thin film on that sample delaminated because of film buckling. The sample is given in Figure 3.3 (c), and Figure 3.3 (d) is run 4 from i-DOE-1, deposited at high power and low pressure.

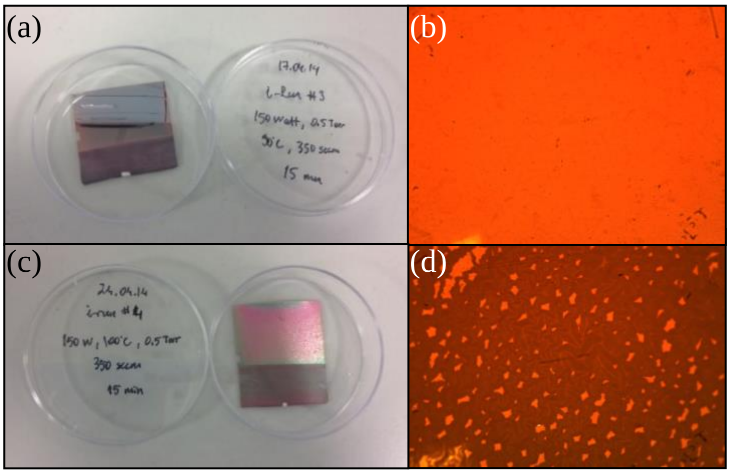

Figure 3.3 (a) Sample of run3 from i-DOE-1 (b) microscope image of run3 (c) Sample of run4 from i-DOE-1 (b) microscope image of run4

From the first experiment, set thickness is measured by a profilometer, film characterization is done via Raman measurement, hydrogen content and microstructure factor are calculated from FTIR measurement, the optical bandgap is extracted from UV-VIS measurement, conductivities are calculated from I-V measurement, and the surface is analyzed by SEM imaging. The details of these analyses are discussed in Chapter 2.

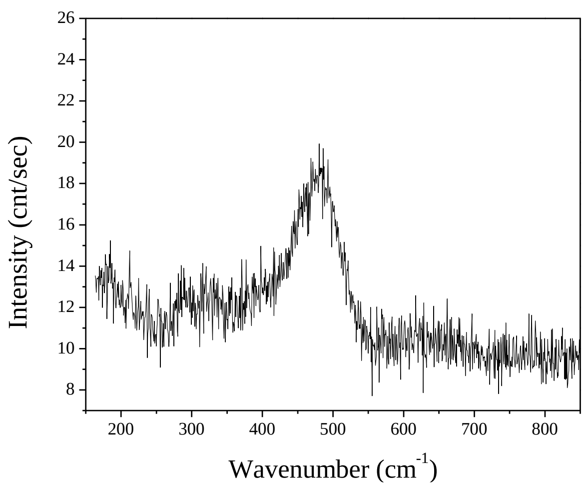

Figure 3.4 Raman measurement from i-DOE-1 of run1 sample deposited on PET

Here a typical Raman measurement of amorphous silicon is given in Figure 3.4. Since all the samples are produced in the amorphous or protocrystalline growth regime, Raman measurement is used only to justify the form of a-Si structure, and no further analysis is carried out.

Structural analysis is done by a deep investigation of the structure of the films via a scanning electron microscope (SEM) image. SEM results show that the films produced on different substrates throughout this thesis have an amorphous structure. As seen in Figure 3.5, the films grown on different substrates are in amorphous form.

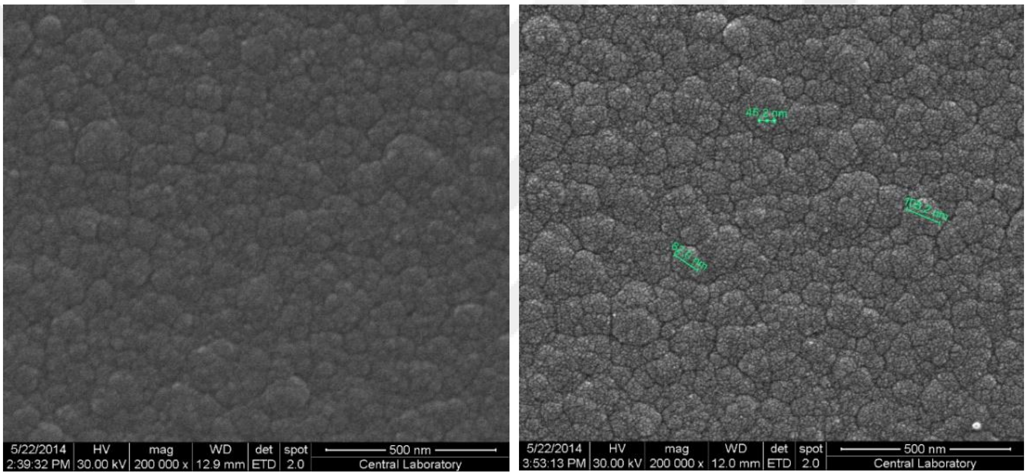

(a) (b)

Figure 3.5 SEM images (a) from pet sample (b) from glass sample

Substrates used in the i-DOE-1 set are TCO-coated PET. Since the PET samples are already coated with TCO, the point contact design is used for I-V measurements. Point contact design was discussed in Chapter 2. I-V measurements are taken from the middle contacts. Metal contacts with less than 1 mm in metal contact design are too small to measure current; thus, they are not considered. Only the four contacts with a size equal to or greater than 1 mm are used for dark I-V measurement, and calculated dark conductivities (given as “cond.” in the table) are given in Table 3.4. The results of conductivities given in the table are the geometrical mean of four measurements.

Contacts are damaged while trying to take measurements from samples of run1 from i-DOE-1; thus, the measurements of such samples are not reliable for analysis. Samples are bent after deposition, and the curvature of the sample depends on the process parameters. This curvature makes it difficult to make electrical contact through the metal pads for current measurement.

Table 3.4 Table of Results of i-DOE-1

EXPERIMENT SET				MEASUREMENTS AND CALCULATIONS				
	Temp. (°C)	**Press. (Torr)**	**Pow. (W)**	**Thick. (nm)**	**C_H (%)**	**E_g (eV)**	**r**	**Cond. ($\Omega^{-1}CM^{-1}$)**
run1	100	1	150	400	11.8	1,75	0.23	5.38x10-7
run2	50	1	150	450	5.9	1,72	0.14	5.53x10-10
run3	50	0.5	150	380	7.0	1,74	0.21	1.02x10-9
run4	100	0.5	150	350	3.8	1,84	0.18	PEELED
run5	50	1	50	280	2.7	1,86	0.70	1.22x10-9
run6	100	1	50	350	8.4	1,83	0.61	1.57x10-10
run7	50	0.5	50	270	14.0	1,83	0.56	1.74x10-8
run8	100	0.5	50	270	10.6	1,83	0.31	7.83x10-10
repeat1	80	0.8	100	330	10.8	1,76	0.35	5.78x10-10
repeat2	80	0.8	100	340	4.5	1,80	0.39	7.52x10-11
repeat3	80	0.8	100	410	10.7	1,76	0.42	4.37x10-11

In addition, since the a-Si:H layers are deposited at low temperatures, metal contacts cannot be annealed after evaporation. In order to overcome these issues, first, it is tried to make a wire bond to the contact with metal paste to take the current measurement without damaging the contact pads, but the contact size and number of contacts make it difficult for wires to stay on the sample. A vacuum chuck probe station is used for IV measurements as a second solution. The vacuum chuck probe station avoids measurement problems due to bending, but only dark I-V measurements can be taken with this setup. Conductivity values obtained are all in the range of high-quality film. After these experiments, metal contact design and substrates are changed.

All the quantities studied to optimize the a-Si:H layers are affected by the system parameters: deposition temperature, deposition pressure, and deposition power. It is observed that hydrogen content decreases when the pressure increases. The other parameters, temperature and pressure, do not play an essential role in the bandgap since the changes in the values are around 0.02. The increase of power decrease the bandgap and the microstructure factor dramatically. As power increases, silane disassociation into radical gets promoted, and as a result, high-quality film formation is obtained.

As a result of the optimization matrix of i-DOE-1, it is founded that the parameter used to produce run6 is the most appropriate parameter group for thin film silicon solar cell application. However, as discussed previously, these results are not used for intrinsic layer deposition for thin film solar cells since the i-chamber design has changed.

The studies carried out until the i-chamber change contributed to the experiments done after the new chamber installation. Accordingly, the production parameters were fixed as 175°C temperature, 1 mTorr pressure, and 50 W power. As a result of experiments with these variables in the new i-chamber, it was observed that most of the films produced were peeled off. The results from i-DOE-2, where measurements can be made, are presented in combination with i-DOE-3.

Deposition power is reduced to overcome the delamination problem. One of the delaminated samples within the i-DOE-2 is reproduced with decreased power value. R=9 is reproduced for this comparison.

Dark conductivity (σ_d) and photoconductivity (σ_{ph}) are calculated from the I-V measurements of i-DOE-3 samples. The photoconductivity to dark conductivity ratio, which is the photosensitivity, gives the intrinsic layer's electrical quality. Ratios higher than five orders (σ_{ph} / $\sigma_d > 10^5$) are considered as qualified layers for solar cells [35].

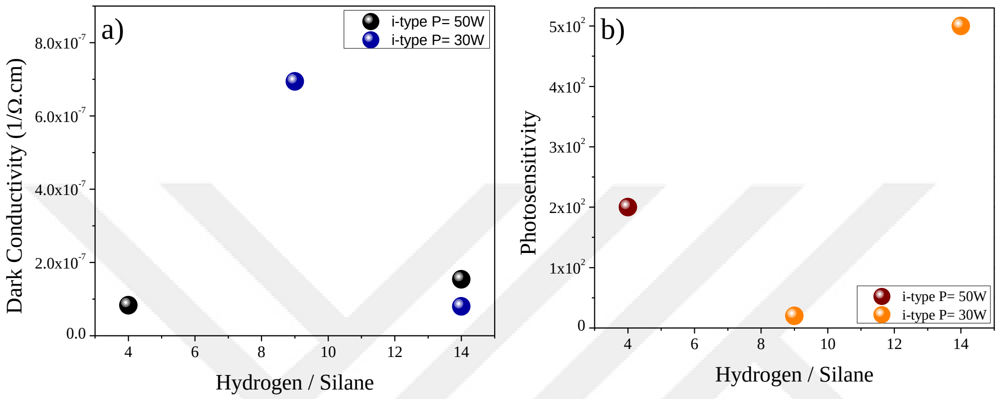

Figure 3.6 a) Dark conductivity change b) Photoresponse change to the hydrogen to silane change of both i-DOE-2 and i-DOE-3

The results represented in Figure 3.6 of the i-DOE-2 show that the hydrogen to silane ratio does not affect the dark conductivity. According to the intrinsic a-Si:H characterization study (i-DOE-3), the calculated photoresponse values do not reach five orders. Low photoresponse is due to slightly high dark conductivity values. The low production temperature also contributes to the result. Low deposition temperatures result in higher defect densities in the film, resulting in higher dark conductivity values.

According to the optimization study of intrinsic layer results, the most proper intrinsic a-Si:H layer for thin film silicon solar cell is chosen to be at the edge of crystallinity transition (R>10) and with high photoresponse. Intrinsic layers for device production are deposited at 30W, 1 mTorr, 175°C having hydrogen to silane ratio R=14.

3.2 Optimization of Boron Doped Amorphous Silicon (p-aSi:H) Layer

Different types of boron sources, such as diborane(B_2H_6) and trimethyl boron (TMB), are used in studies in the literature. Doping is done by Boron atoms to obtain p-type material of hydrogenated amorphous silicon (p-aSi:H). In this study, p-type silicon layers are obtained with a gas mixture of silane and diborane during PECVD deposition. Diborane diluted to 2% of volume in hydrogen gas is installed in the cluster system for p-aSi:H deposition.

Diborane is a form of boron hydride, and it is a colorless, toxic, and flammable gas. It is reported that diborane is decomposed slowly at room temperature and in hydrogen dilution [30]. 2% diluted diborane degrades 85% of its initial value within 600 days. The dopant to silane ratio is calculated according to this decay for each experiment.

All the p-type doping studies are carried out with pure silane gas connected to the cluster system. For simplicity, preliminary studies do not concentrate on the $R=[H_2]/[SiH_4]$ ratio. The ratio $D=[B_2H_6]/[SiH_4]$ is determined to examine its effect on the electrical and optical properties of the doped layers. Low-temperature production enables the possibility of deposition onto PET substrates. Thus, the initial experiment set, prepared according to the changing D ratio, is planned at room temperature with the lowest deposition temperature value.

According to the data obtained from the first set of experiments, it is seen that the desired doping levels could not be reached. In addition to the low production temperature, it is observed that diborane is not sufficient to dope the silicon layers due to the decomposition of the diborane. Decomposition of diborane also leads to dust particles in films and pinholes caused by these dust particles. New diborane gas is installed in the system before further experiments are done. A comparative study with different temperatures is planned in the second set of experiments. For this purpose, plastic substrates are no longer used since they cannot sustain temperatures greater than 150°C. Ultra-thin flexible glasses are used as the substrate due to increased temperature levels.

During doping study experiments, a third experiment set is planned to investigate the effect of higher dopant to silane ratios regarding the previous design of the experiment. For the third set of experiments, the working temperature is 175°C, and additional experiments are carried out at 100°C for comparison within this experiment design. As a result of the productions carried out for temperature comparison, no change was observed in the conductivity value. As a result of this situation, system heaters are tested for performance.

The heaters performance test is taken place for two days with a thermocouple placed on the substrate surface in the p chamber. On day 1, the p chamber is heated to 275°C. System temperature increases by 10 degrees every two minutes starting from room temperature. The p chamber is kept at 5E-5 torr pressure, and the temperature is set to 275°C for 2 hours, but the p chamber temperature reaches only 70.8°C during this period. After 2 hours of wait time, a standard procedure of substrate heating, which is heating under nitrogen (N_2) atmosphere at 0.8 torr pressure for 5 minutes, is applied. After this heating procedure, the chamber temperature only reached 83°C temperature value. System heaters are kept open at 170°C set value overnight. On day 2, the heating test started at 170°C set value, and the actual temperature read was only 45°C. When the 275°C set temperature is reached, heating under an N_2 environment for 10 minutes is applied. This heating procedure is repeated two more times, and the max temperature reached is only 120.2°C. It is concluded that heaters do not work correctly; thus desired temperature of 175°C cannot be reached in reality. As a result of this heating test, it is revealed that the heaters of the system do not work correctly. In addition to that, at high-temperature values setting heaters blow a fuse and then shut down the system. After that, the system goes into maintenance to overcome such problems.

During maintenance, a heater calibration was studied for the p-chamber. After fixing the chamber issues, one last experiment is designed to finalize the deposition parameters of the p-aSi:H layer for solar cell application. The details of the design of the experiments are given in the following sections.

3.2.1 p-aSi:H Deposition Parameters

Investigation of doping levels of a-Si layers is done by doping gasses. PECVD process parameters that will affect the doped silicon layers are the same as the intrinsic layer. Additional parameters that will affect the deposition are the total gas flow rate (T.Flw.) and the dopant to silane gas molar ratio (D).

Samples for the analysis are prepared as described in Chapter 2. The p-type material is produced in thicker layers than the solar cell structure to characterize these layers suitably. According to the intrinsic layer optimization study results, the following parameters are constant during depositions.

- Fixed parameters: 50 W, 1 Torr, 20 minutes deposition

The varying parameters are the flow rate of process gasses and the deposition temperature. The rate of the varying process gases, flow rate, is given as the dopant gas to silane ratio. Ultra-thin flexible glasses are used as flexible substrates in experimental sets designed to see the effect of temperature on doped films. PET substrates are not used for the experiment with a temperature greater than 150°C since they cannot resist high temperatures.

3.2.2 p-aSi:H Design of Experiments (p-DOE)

Preliminary studies are dependent on doping of the p-aSi:H layer at room temperatures (R.T.). Fix parameters are total flow rate (350 sccm), silane flow rate (22 sccm), and deposition power (50W). Two-level doping and two-level of deposition pressure are considered. Ratio (D: N_{dopant}/N_{silane}) is calculated according to a decayed concentration estimation of 0.8%. Deposition pressure change is planned to examine the deposition parameters optimized for the intrinsic layer deposition chamber. The first design of the experiment for p-aSi:H layer characterization (p-DOE-1) is given in Table 3.5. According to the table given below, 3 experiments are conducted. Samples used in p-DOE-1 are ultra-thin flexible glass and one side adhesion promotion treated PET (OS-PET). Samples were very resistive so that no I-V characteristics were observed even if very narrow contact pads were used.

Table 3.5 Preliminary design of experiment for doping of a-Si (p-DOE-1)

Sample Name	p1	p2	p3
Deposition Power	50 W		
Deposition Pressure	1 mTorr	0.8 mTorr	1 mTorr
N_{dopant}/N_{silane}	0.007	0.01	0.01
Temperature	R.T.		

According to the results of p-DOE-1, the deposition pressure value is fixed at 1 mTorr. Also, after installing new diborane to the deposition system, a new design of the experiment, which is given in Table 3.6 (p-DOE-2), is created. Since the deposition temperature of this experimental set is increased to 225°C, PET substrates are not used. A total of 9 depositions are done for the second doping study.

Table 3.6 Design of Experiment for doping study of p-aSi:H (p-DOE-2)

	LEVEL 1	LEVEL 2	LEVEL 3
Deposition Power	50 W		
Deposition Pressure	1 mTorr		
N_{dopant}/N_{silane}	0.015	0.047	0.07
Temperature	R.T.	175°C	225°C

Due to achieving the low-temperature production target, the medium temperature is determined as the fabrication temperature for the new experiments. After p-DOE-2, the deposition temperature is chosen to be 175°C. As a comparison study, depositions at a lower temperature (at 100°C) are also done. Deposition parameters, levels, and values of p-DOE-3 are given in Table 3.7. 9 experiments for p-DOE-3 are planned to see the effect of a lower D ratio on doping of a-Si:H.

Table 3.7 Design of Experiment for doping study of p-aSi:H (p-DOE-3)

Parameters	Levels	Values
Deposition Power	-	50 W
Deposition Pressure	-	1 mTorr
Temperature	2	100°C – 175°C
$D = N_{Dopant}/N_{Silane}$	3	0.008 – 0.013 – 0.025

According to the results of p-DOE-3 productions, it is revealed that the heaters of the p-chamber do not work correctly. Due to the unexpected system shutdown, the system goes under maintenance, and a new set of experiments is planned. Different dopant to silane ratio is also considered to optimize doped layers. A narrow interval of dopant ratio is chosen to tune out the layer characterization concerning the previous optimization set reported. Deposition parameters levels and values are given in Table 3.8 and experiments.

Table 3.8 Design of Experiment for doping study of p-aSi:H (p-DOE-4)

Parameters	Levels	Values
Deposition Power	-	50 W
Deposition Pressure	-	1 mTorr
Temperature	-	175°C
$R = N_{Hydrogen} / N_{Silane}$	2	4 – 18
$D = N_{Dopant}/N_{Silane}$	3	0.015 – 0.055

Effect of dopant to silane ratio and effect of hydrogen to silane ratio on conductivity, bandgap, and hydrogen content of these films is reported. According to the optimization results, the best parameters having the highest performance were chosen for device production. Adding diborane to this gas mixture provides B atoms to the a-Si:H to have p-type doping.

3.2.3 Results and Discussion of Boron Doped a-Si:H Layer Optimization

The first design of experiments (p-DOE-1) conducted to optimize p-type a-Si:H is analyzed optically and electrically. These experiments are done with old diborane installed in the cluster system. Ratio (D: N_{dopant}/N_{silane}) is calculated according to an estimation of decayed concentration diborane. Varying deposition parameters are tabulated in Table 3.9.

Table 3.9 Results of p-DOE-1

Sample Name	N_{dopant}/N_{silane}	***B_2H_6 Flow***	***Dep. Pressure***	***Thickness***	***Substrate***	***Bandgap***
p1	0.007	19.5 sccm	1 Torr	110 nm	Flex. Glass	1.91
					OS-PET	1.85
p2	0.1	35 sccm	0.8 Torr	230 nm	Flex. Glass	1.72
					OS-PET	1.74
p3	0.1	35 sccm	1 Torr	190 nm	Flex. Glass	1.85
					OS-PET	1.85

In Table 3.9, calculated optical bandgaps are reported. Samples are very resistive so that no I-V characteristics are observed even if very narrow contact pads are used. It is known that the dopant precursor gas decays in time. Results showed that proper doping could not be sustained under these conditions. New diborane is ordered, and a new experiment set is designed (p-DOE-2). In the second set of experiments, production pressure and power values are kept constant to examine the temperature and doping concentration in more detail.

It is known that diborane gas decomposes by solidifying over time. Solidification causes dust particles to form, which adhere to the film surface by mixing with the plasma during production. Dust particles separated from the film surface after production form pinhole structures in the film. Such pinhole structures are observed via visual inspection and microscope imaging on the film surface in the productions carried out.

No pinhole structures are found in the films produced after introducing new diborane gas into the system. In the first production after the gas exchange, too many pinhole structures are encountered, and measurements of these productions could not be made. This situation is caused by the dust particles remaining in the gas line. The fact that pinhole structures are not encountered in other productions of the p-DOE-2 experimental set supports the argument that pinhole structures originate from diborane gas.

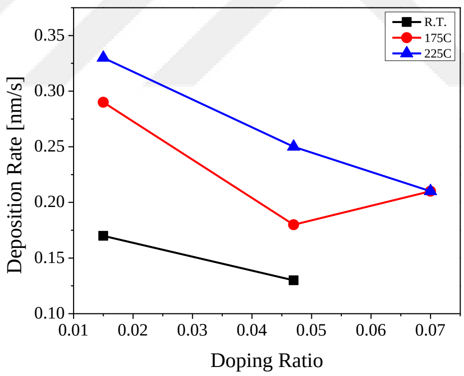

Figure 3.7 Deposition rate dependence on doping ratio

The average deposition rate is calculated by analyzing the results of the second set of experiments. As expected and seen in Figure 3.7, the deposition rate decreases as the dopant to silane ratio increases. As a result of the results obtained here, thickness estimation can be made for the parameters determined from the optimization study.

Since the amorphous silicon is used as an alloy of hydrogen and silicon, it is crucial to analyze the hydrogen content in the material. Hydrogen content is a measure of control of defect density in the material where it should be in the range of less than 25% and higher than 2.5%. Hydrogen characterization is done from Fourier infrared transform spectroscopy (FTIR) measurement, and the results are given in Figure 3.8. The hydrogen content of the films is in the range of optimum concentration.

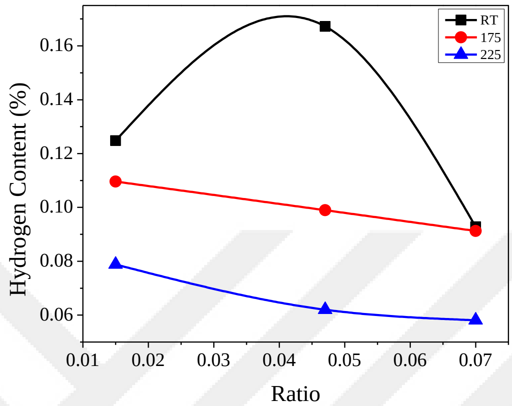

Figure 3.8 Hydrogen content dependence dopant to silane ratio

Further characterization of electrical analysis is conducted via I-V measurements. The calculated dark conductivity values are shown in Figure 3.9 with solid shapes and lines; photoconductivity values are given with hollow shapes and dashed lines.

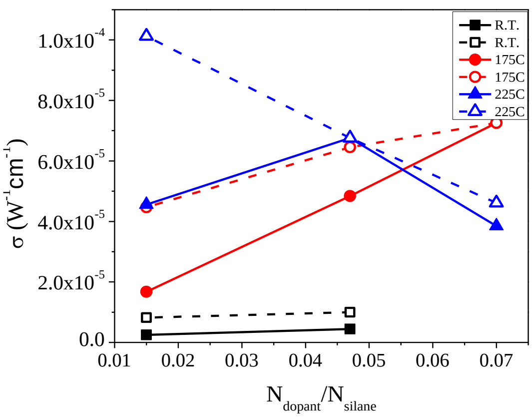

Figure 3.9 Conductivity dependence on the ratio

The typical value of dark conductivity of the p-type a-Si:H layer is $10^{-6}\Omega^{-1}cm^{-1}$ [36]. Low-temperature samples have high resistivity, and therefore one of the samples could not be measured. The lower dopant to silane ratio should be investigated to obtain higher conductivity.

As shown in Figure 3.10 bandgap of the films decreases with increasing doping ratio, which is consistent with the literature. The bandgap of the p-layer is lower than the intrinsic layer. As a window layer p-layer should have a wider bandgap. Usually, it is obtained using another alloy of a-Si, carbohydrate boron-doped amorphous silicon. This type of p-layer is out of the scope of this thesis. In order to overcome the low bandgap of p-layer is used as thin as possible for this study.

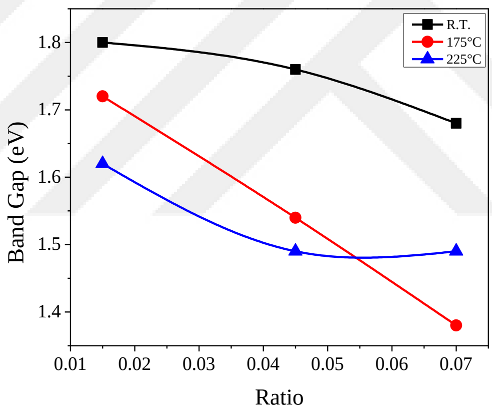

Figure 3.10 Effect of dopant to silane ratio on Optical Bandgap change

According to the electrical analysis of the depositions at room temperature, the films are not sufficiently doped to show photoresponse. Based on these two results, a deposition temperature of 175 °C was chosen to achieve high absorption for the device application.

The p-DOE-2 shows that the new gas installed in the system works appropriately. For further study, low doping ratios are studied with p-DOE-3. During the deposition of experiments of p-DOE-3, at high-temperature depositions, it is revealed that the heaters of the system do not work correctly and blow a fuse and shut down the system. As a result of this problem, one of the experiments within this matrix cannot be produced. Results of this p-DOE-3 in terms of bandgap, dark conductivity (σ), and H2 content (C_H at. %) are tabulated in Table 3.10.

Table 3.10 Results of p-DOE-3 of Boron doping study

		100°C			175°C		
R	D	Eg (eV)	σ (1/Ω.cm)	C_H at. %	Eg (eV)	σ (1/Ω.cm)	C_H at. %
9	0.008	1.76 eV	3.28E-06	27.9			
18	0.008	1.81 eV	3.25E-06	14.4	1.8 eV	1.14E-06	10
18	0.013	1.78 eV	2.56E-06	10.1			
18	0.025	1.67 eV	1.03E-05	7.5	1.67 eV	7.71E-06	9.9

In addition to that, the last doping study experiments show that another parameter, the silane to hydrogen ratio, is an essential and significant effect on bandgap and hydrogen content. Subsequent experiments on doping are designed accordingly.

It is revealed that each experiment's deposition temperatures could not reach the designed temperatures. As a result of this issue, the heaters of the system changed to obtain uniform heating at a temperature of 175°C. New optimization sets are designed for future studies.

Table 3.11 Results of p-DOE-4 of Boron doping study

		R=4		R=18	
T (°C)	D	Eg (eV)	σ (1/Ω.cm)	Eg (eV)	σ (1/Ω.cm)
175	0.015	1.73	3.93E-05	1.73	8.00E-06
175	0.035	1.73	3.68E-05	1.73	4.03E-06
175	0.055	1.75	4.88E-05	1.73	2.24E-05

Results of the last doping given in study experiments show that another parameter, the silane to hydrogen ratio, is essential and significantly affects bandgap and hydrogen content. Results are given in Table 3.11. The doped layer experiment design is selected accordingly. During this optimization, setting bandgap values does not change drastically. Results show that the bandgap does not significantly change the doping ratio. However, the hydrogen to silane ratio (R) has a more significant effect on the bandgap. The hydrogen to silane ratio mainly affects the bandgap of the material. On the other hand, the dopant to silane ratio affects the conductivity of the layers.

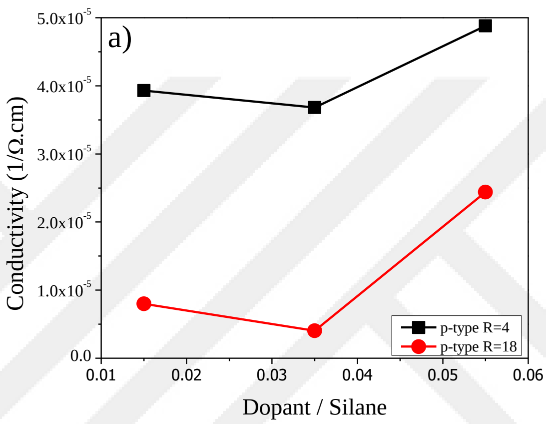

Figure 3.11 Effect of dopant to silane ratio on conductivity

3.3 Optimization of Phosphorus Doped Amorphous Silicon (n-aSi:H) Layer

Investigation of doping levels of a-Si layers is done by doping gasses. Doping of amorphous silicon is investigated to obtain n-layers. Phosphorus atom is used to obtain n-type a-Si:H layers. The dopant gas used in the system for the n-layer is phosphine (PH_3). PECVD process parameters that will affect the doped silicon layers are the same as the p-layer. Doping is studied in terms of changing dopant to silane ratios. According to the previous optimization study of a-Si:H depositions, other parameters are fixed. Parameters of deposition power, deposition pressure, deposition temperature, and silane flow are fixed during deposition.

Characterization analysis includes optical and electrical analysis to gather optical and electrical properties of the films through UV-Visible spectroscopy and I-V measurement. In addition to those characterizations, time of flight secondary ion mass spectrometry (ToF-SIMS) is done to find the doping concentration of each layer.

A new cylinder of dopant (phosphine) of PH_3 is installed in the system before the optimization study experiments are done. After the first set of experiments, the heat performance test procedure is applied to the n-chamber.

As a result of the heater performance test done for the n-chamber, the same heater problem is present. Day 1 starts with a cold chamber, and the system is the temperature set point increased gradually under vacuum. The system is heated under 0.8 Torr pressure for 5 minutes as the usual heating procedure. The maximum value reached on day 1 is 133°C. At the end of day-1 heater is left open at the 150°C set value; thus, day 2 starts at the 150°C set temperature. The maximum setpoint, which is 400°C, is reached at the end of day 2. Even if the maximum setpoint is used, the maximum value reached at the end of day 2 is again 133°C. Better than p-chamber but still cannot reach the desired value of 175°C.

3.3.1 n-aSi:H Deposition Parameters

Varying process parameters achieve optimizations of the films to reach the demands of a proper conductive layer for thin film silicon solar cell applications. Doped layers are investigated in varying dopant to silane ratios (D; doping ratio). In order to reduce some of the varying parameters, deposition power, deposition pressure, deposition temperature, and silane flow is fixed during each deposition.

Phosphine (PH3) diluted to 2% of volume in hydrogen gas is installed in the cluster system for p-aSi:H deposition. The parameters determined as fixed and variable for the production are determined by considering the parameters previously optimized for the intrinsic and p-type layer deposition chambers. Samples are prepared as reported previously. The following parameters are fixed during deposition.

- Fixed parameters: 175°C, 50 W, 1 Torr

The varying parameters are the flow rate of process gasses and temperature. The flow rate of the varying gases is given as the dopant to silane ratio (R). The production time for the first experimental set is 20 minutes, and the production time for the second experimental set is 10 minutes.

3.3.2 n-aSi:H Design of Experiments (n-DOE)

Electrical characterization of a-Si:H layers is obtained via I-V measurement to determine n-type doping. New experiment matrices are designed according to the results of p-type doping. For this study, the silane to hydrogen ratio is taken into account. DOE-1 for the n-type doping study is given in Table 3.12.

Table 3.12 Design of Experiment for doping study of p-aSi:H (n-DOE-1)

Deposition Power	50 W	
Deposition Pressure	1 mTorr	
Temperature	175°C	
$R = N_{dopant}/N_{silane}$	0.08 – 0.008	
$N_{Silane}/N_{Hydrogen}$	1/4	1/18

14 experiments are done to obtain a proper conductive layer for thin film silicon solar cell deposition. FTIR characterization could not be done for n-type layers. The reason is the lower film thickness of the FTIR sample. Similar to p-type characterization, deposited films are characterized electrically to obtain dark conductivity values.

Phosphorus doping is done by phosphine to obtain n-type a-Si:H layers. Experiment matrices are designed to match the boron doping study for consistency shown in Table 3.13.

Table 3.13 Design of Experiment for doping study of p-aSi:H (n-DOE-2)

Deposition Power	50 W	
Deposition Pressure	1 mTorr	
Temperature	175°C	
$R = N_{Hydrogen} / N_{Silane}$	4	18
$D = N_{dopant}/N_{silane}$	0.015 – 0.055	

3.3.3 Results and Discussion of Phosphorus Doped a-Si:H Layer Optimization

14 experiments were done to obtain a proper conductive layer for thin film silicon solar cell deposition. Similar to p-type characterization, deposited films are characterized electrically to obtain dark conductivity values. Conductivity results given in Table 3.14 are measured from flexible glass substrates.

Table 3.14 Conductivity results of phosphorus doping study (n-DOE-1)

Silan/Hydrogen	PH_3/Silane	σ (1/Ω.cm)	Silan/Hydrogen	PH_3/Silane	σ (1/Ω.cm)
1/4	0.0035	9.46E-06			
1/4	0.005	1.14E-05			
1/4	0.008	1.85E-05	1/18	0.008	2.94E-03
1/4	0.015	5.56E-06	1/18	0.015	2.50E-03
1/4	0.035	1.79E-06	1/18	0.035	1.00E-03
1/4	0.065	7.41E-07	1/18	0.065	8.33E-05
1/4	0.08	2.50E-07	1/18	0.08	3.00E-05

The bandgap is calculated from UV-VIS measurement done via a flexible glass substrate. Results given in Figure 3.12 show that the bandgap does not significantly change the doping ratio. However, the hydrogen to silane ratio (R) has a more significant effect on the bandgap.

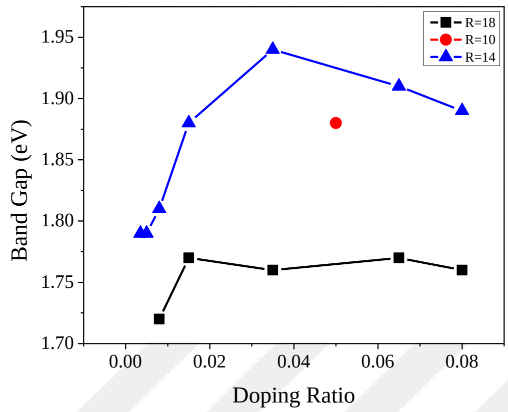

Figure 3.12 Effect of PH_3 to silane ratio on Optical Bandgap change

Phosphorus concentration in n-type films is obtained from ToF-SIMS results for selected samples and represented in Figure 3.13. Doping concentration cannot be compared with a universal reference; nevertheless, results show that films are sufficiently doped with phosphorus atoms.

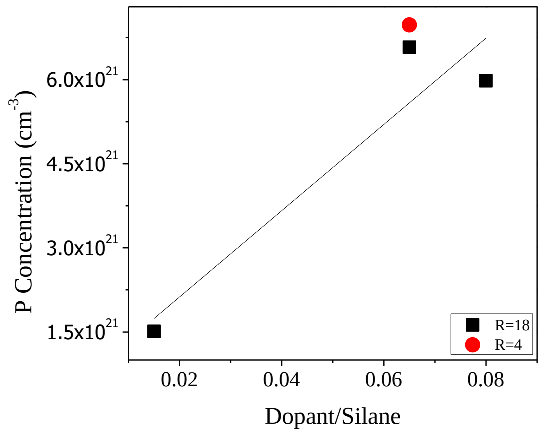

Figure 3.13 Phosphorus concentration obtained from ToF-SIMS result (black line is drawn to guide the eye)

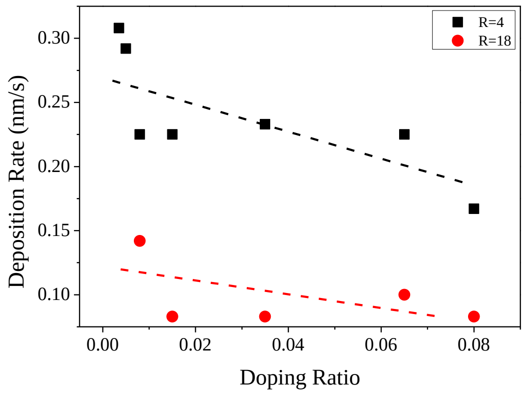

Figure 3.14 Deposition rate to doping ratio

Results obtained from n-DOE-2 are represented in Table 3.15 shows good conductivity results after changing heaters.

Table 3.15 Results of n-DOE-2 of phosphorus doping study

		R=4		R=18	
T (°C)	D	Eg (eV)	σ (1/Ω.cm)	Eg (eV)	σ (1/Ω.cm)
175	0.015	1.86	1.94E-03	1.89	1.67E-02
175	0.035	1.92	3.68E-03	1.83	5.71E-04
175	0.055	1.94	4.88E-03	1.84	3.50E-03

3.4 Summary

In this chapter, silicon-based thin-film solar cells produced in the RF PECVD type thin-film deposition system GünEr and the optimization of amorphous silicon layers are studied. Amorphous silicon layers were produced in three different types intrinsic, p-type and n-type. Each type of layer was grown in separate production chambers and characterized separately.

Changing the deposition parameters also means changing the properties of the films. This study determined the production parameters of the layers required to produce amorphous silicon-based thin film solar cells. The optical, electrical, and morphological properties of the films were investigated to determine the effects of production parameters.

Merit parameters for the device quality intrinsic layer are given in Table 3.16. Results of characterizations are discussed according to reach these values.

Table 3.16 Merit parameters for device quality p-i-n layers

Parameter	p-aSi:H	i-aSi:H	n-aSi:H
C_H	$\leq$ 10 atomic %	$\leq$ 10 atomic %	$\leq$ 10 atomic %
Band Gap	~1.7 eV	1.7-1.8 eV	1.8-2.0 eV
Microstructure Fac.	< 0.2	< 0.2	< 0.2
Dark Conductivity	$> 10^{-2}\ \Omega^{-1}\ cm^{-1}$	$< 10^{-11}\ \Omega^{-1}\ cm^{-1}$	$> 10^{-1}\ \Omega^{-1}\ cm^{-1}$
Photo Conductivity	-	$1x10^{-5}\ \Omega^{-1}\ cm^{-1}$	-

During the studies, the design of the intrinsic layer deposition chamber is changed. The i-type chamber is re-characterized to eliminate the differences in production parameters due to this change. The production parameters determined by the first intrinsic layer studies are taken as the basis for p- and n-type chambers.

Table 3.17 Summary of the optimization of a-Si:H layers

		Gas Flows (sccm)			Ratios		Conductivity	Band gap
# of Run	Type	Dopant	SiH_4	H_2	R	D	1/Ω.cm	eV
1	p	45	60	196	4	0.015	3.93E-05	1.73
2	p	105	60	137	4	0.035	3.68E-05	1.73
3	p	165	60	78.3	4	0.055	4.88E-05	1.75
4	p	18.75	25	432	18	0.015	8.00E-06	1.73
5	p	43.75	25	407	18	0.035	4.03E-06	1.73
6	**p**	**68.75**	**25**	**383**	**18**	**0.055**	**2.44E-05**	**1.73**
7	n	45	60	196	4	0.015	1.94E-03	1.86
8	n	105	60	137	4	0.035	1.25E-03	1.92
9	n	165	60	78.3	4	0.055	2.00E-03	1.94
10	**n**	**18.75**	**25**	**432**	**18**	**0.015**	**1.67E-02**	**1.89**
11	n	43.75	25	407	18	0.035	5.71E-04	1.83
12	n	68.75	25	383	18	0.055	3.50E-03	1.84
14	i	-	35	315	9	-	6.94E-07	
15	i	-	23	327	14	-	8.00E-08	

Due to the high temperatures requirement for doping studies, device applications are carried out only on ultra-thin flexible glass substrates. According to the results of the p-type doping studies, the production temperature was determined as 175°C. For this reason, ultra-thin flexible glass was chosen as the substrate for flexible thin film solar cell production.

The doping study of amorphous silicon layers is finalized with top parameters that can be reached with this cluster system. Each layer was characterized electrically, optically, and structurally. In order to optimize doped layers, different dopant to silane ratio samples is varied. The effect of the dopant to silane ratio and hydrogen to silane ratio on these films' conductivity, bandgap, and hydrogen content was reported in Table 3.17. According to the optimization set, the best parameters used to produce high-efficient silicon solar cells are denoted in red in Table 3.17.

CHAPTER 4

OPTIMIZATION, CHARACTERIZATION, AND LASER TEXTURING OF TRANSPARENT CONDUCTIVE OXIDE LAYER

This chapter gives the optimization and characterization studies of transparent conductive oxide (TCO) layers used in single junction amorphous silicon thin film solar cells. In this study, aluminum-doped zinc oxide (AZO) is used as the TCO layer. In this chapter, the texturing of the AZO layers via direct laser writing is also examined.

Optimization of the AZO films is achieved by varying process parameters of the TCO layer to reach the requirement for thin film silicon solar cell applications. AZO layers are deposited in the sputter chamber of the GünEr cluster system in GUNAM. The effect of deposition power, deposition pressure, and deposition temperature on the film quality are investigated. In order to use appropriate TCO for device application, various characterization methods are done. Structural analysis of the films is done by X-ray diffraction spectroscopy. The optical and electrical properties of the films are carried out through UV-Visible spectroscopy and four-point probe measurements. The thickness of the films is obtained by spectroscopic ellipsometry. Structural analysis is done for crystallinity, electrical characterization is done to find the conductivity of the thin film, and optical analysis is done to determine the AZO film's bandgap and investigate the films' transmissivity.

The texturing of thin films is achieved by laser application. The laser is set for a straight-line scan to obtain uniform ablation in a linear pattern. By changing the laser frequency and direction of the scan, periodic or random various features geometries are obtained. The resulting surface texture is characterized using scanning electron microscopy (SEM) and atomic force microscopy (AFM). Four-point probe measurement is used to determine the sheet resistance of the textured films. The optical response of the obtained textures, such as total transmittance and haze in transmittance, was obtained using an integrating sphere system. The effect of each process parameter on film quality is discussed, and the results are given in the following sections.

4.1 Optimization of Aluminum-doped Zinc Oxide (AZO) Layer

TCOs have widely studied materials for various applications. Prevalent TCOs used in photovoltaic applications are indium tin oxide (ITO), fluorine-doped tin oxide (FTO), and aluminum-doped zinc oxide (AZO) [37], [38],[39]. For photovoltaic applications such as solar cell production, a key issue is reducing the fabrication cost. For this purpose, both low-cost materials and substrates are introduced. Flexible and lightweight plastic substrates are commonly used, especially for roll-to-roll processes. An important parameter to work with plastic substrates is temperature. The low-temperature resistance of plastic substrates limits the production conditions, which have been recently investigated [40],[41]. On the other hand, new low-cost materials such as ultra-thin flexible glass are introduced for OLED displays and other electronic applications [42],[43],[44],[45]. . These ultra-thin flexible glasses hold the inherent benefits of high transparency, high surface quality, and high thermal stability, yet they are still fragile.

Among the TCO materials, AZO is preferred due to its high transparency, non-toxicity, excellent thermal stability, and low cost [46]. Another advantage of thin film silicon solar cell applications is its compatibility with hydrogen-rich plasma media [47]. Various studies show that AZO layers also fulfill these requirements [48],[49]. AZO films are usually deposited by sputtering (RF or DC), vacuum arc plasma evaporation, and pulsed laser deposition (PLD) [50], [51], [52], [53]. Among these techniques, magnetron sputtering has advantages in the low substrate temperature, good adhesion of films on different substrates, high deposition rates, high uniformity, and adoption to a large-scale fabrication [54]. Therefore, radiofrequency (RF) magnetron sputtering is the preferred technique for low-temperature deposition on PET and ultra-thin glass substrates in this study.

The aim is to optimize the deposition of low temperature (room temperature) AZO films on two different flexible substrates for photovoltaic applications. By changing deposition conditions such as deposition power and deposition pressure, optimum high conductive and high transparent AZO films are found. Also, a systematic comparative study is carried out for low-temperature AZO deposited on PET and ultra-thin flexible glass substrates.

The main objective of this thesis is to produce thin film silicon solar cells onto flexible substrates; for this purpose, different types of flexible substrates are compared. The first choice of the flexible substrate is a TCO-coated PET. It is a commercially available substrate with 60 Ω/sq sheet resistance. Later uncoated PET and ultra-thin flexible glass substrates are used. Since all the samples are transparent to visible light, superstrate configuration is preferred for deposition sequence. In addition to the superstrate configuration, AZO and silver (Ag) combinations are produced on ultra-thin flexible glasses and patterned by wet chemical etching.

Single-layer characterization of AZO is optimized for the front contact of thin film a-Si solar cell. A multi-layer AZO stack is also intended to be used in the same application, but it is applied to crystalline silicon for the proof of concept. Here in the following sections, these two different studies are presented.

4.1.1 Single Layer AZO

Production is done with the most widely used RF magnetron sputtering deposition method to produce the AZO layer. The aim is to optimize the process parameters of the AZO layer for the system GünEr. Sputter process parameters that will affect the AZO layer are plasma frequency (F), plasma power (Pw.), deposition pressure (Pr.), gas flow rate (Flw.), Oxygen/Argon (O_2/Ar) feed gas molar ratio (R), substrate temperature (T), and the distance between the substrate and the plasma source (d).

The plasma frequency and the distance between the substrate and the plasma source are constant due to the deposition system's characteristics. The plasma frequency is RF (13.56 MHz), and the distance between the substrate and the plasma source is 5 cm.

The main goal of this study is to optimize the layer of AZO according to the need for an optimum front contact layer for a solar cell application. Parameters such as oscillation number and the motor speed of the substrate holder affect the thickness and the uniformity of the film, respectively. Since one of the substrates is PET, low-temperature deposition is favorable. For this reason, layer optimization is done at room temperatures. In addition, a high-temperature process is also carried out for ultra-thin flexible glass substrates. Depending on previous experiences with deposition, the flow rate of Ar is fixed at 125 sccm in all optimization experiments. While the system uses the AZO source as a ceramic target, O_2/Ar does not need to be changed during deposition. Processes are done as non-reactive depositions. However, this ratio change is studied for further investigation on the bandgap and refractive index of the AZO layer.

4.1.1.1 System Process Parameter Optimization for AZO

The design of the experiment (DOE-1) set is prepared with two process parameters: the deposition pressure and the applied RF power. These two parameters are investigated on three levels. Thus, the total number of experiments will be 9.

All the depositions for the DOE-1 are conducted at room temperature (R.T.) and under 125 sccm Ar flow. DOE-1 experiments start at low temperatures. Later, the experiments with the best performance are repeated with relatively high-temperature values. The deposition parameters for DOE-1 are given in Table 4.1.

Table 4.1 AZO deposition conditions (DOE-1)

Parameter	Level 1	Level 2	Level 3
Ar flow rate	125 sccm	125 sccm	125 sccm
Temperature	R.T.	R.T.	R.T.
Power	300 W	400 W	500 W
Pressure	3 mTorr	5 mTorr	8 mTorr

As discussed before, different substrates and substrate orientations are present in this study. The first productions are planned to compare the differences created by these substrates. In Table 4.2, the resistivity results of DOE-1 are given. According to the results of the initial deposition of single-layer AZO of DOE-1, the resistivity of different oriented PET samples is not very different. Thus, the rest of the depositions are done on BS PET and ultra-thin flexible glass (UTFG), and the results are discussed accordingly.

Table 4.2 Resistivity of the same AZO layer on different flexible samples

MEASUREMENT	**PET (BS)**	**PET (OS-UP)**	**PET (OS-DOWN)**	**FLEX GLASS**
Thickness	310 nm	310 nm	310 nm	310 nm
Resistivity	1.1E-3 Ω.cm	1.1E-3 Ω.cm	1.1E-3 Ω.cm	1E-3 Ω.cm

Figure 4.1 shows the XRD pattern of PET and ultra-thin flexible glass substrates. In Figure 4.1, peaks denoted by numbers 1, 3, and 4 originated from PET substrate, and the peaks denoted by numbers 2 and 5 come from the AZO layer. Results show that the preferred orientation of the sputtered films is 002 (peak 2), and the second direction of 004 also appears with lower intensity (peak 5). The presence of the intense (002) peak (and also (004)) implies that the grains are dominantly c-axis oriented, which means that the deposited AZO films follow a columnar growth [55]. All of the films exhibit the same XRD pattern.

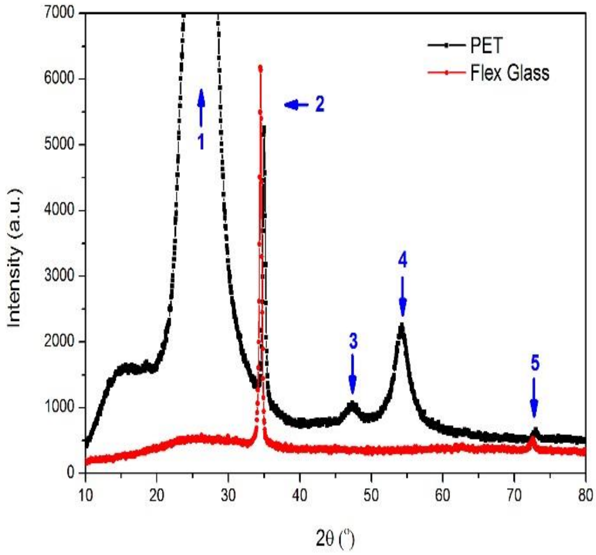

Figure 4.1 XRD pattern of AZO deposited on ultra-thin flexible glass (red) and PET (black) substrates

From the XRD measurement, grain size can be deduced. The peak position and grain size results of 3 mTorr, 5 mTorr, and 8 mTorr, which are deposited at the same power, are given in Figure 4.2.

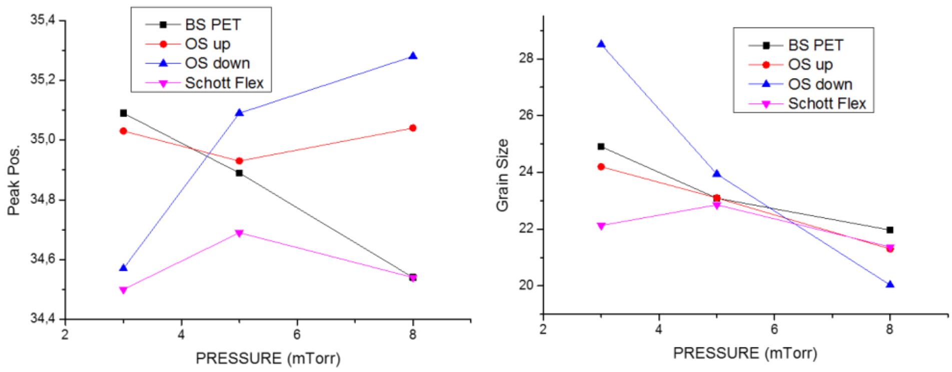

Figure 4.2 Grain size and peak position of XRD pattern with respect to pressure

Table 4.3 Peak Positions and Grain Sizes for different substrates

	3 mTorr		5 mTorr		8 mTorr	
	Peak Pos.	Grain Size	Peak Pos.	Grain Size	Peak Pos.	Grain Size
BS PET	35.09	24.91	34.89	23.09	34.54	21.97
OS UP	35.03	24.20	34.93	23.10	35.04	21.30
OS DOWN	34.57	28.51	35.09	23.94	35.28	20.03
Schott Felx	34.5	22.13	34.69	22.86	34.54	21.37
Reference	**34.45**	**23.76**	**34.45**	**23.76**	**34.45**	**23.76**

Results in Table 4.3 show that (002) Peak position shifts to higher values, implying compressive stress formation on the films (shift to lower values means tensile stress). For each run, the results are similar.

The influence of pressure on deposition rate, bandgap of the material, and conductivity is investigated. The deposition pressure varied from 3 to 8 mTorr, as seen from DOE-1 shown in Table 4.1. The following results are analyzed according to the deposition pressure change.

Table 4.4 The deposition rate and Resistivity of AZO films with respect to changing pressure

Power	500 W		
Pressure	3 mTor	5 mTorr	8mTorr
Thickness (nm)	310	315	300
Deposition Rate (nm/pass)	62	52.5	42.8
Resistivity of PET (Ωcm)	1.1×10^{-3}	1.4×10^{-3}	1.8×10^{-3}
Resistivity of UTFG (Ωcm)	1×10^{-3}	1.2×10^{-3}	1.7×10^{-3}

In this study, the thickness of the film is kept the same as the pressure changes to eliminate one parameter. The thickness of the film can be arranged with substrate movement during deposition. The deposition rate and the resistivity results are given in Table 4.4. As seen from the table, the deposition rate increases as pressure decreases. It is concluded that if the number of passes is kept constant, the thickness of the films increases with decreasing pressure.

In Figure 4.3, the dependency of deposition rate on deposition pressure is plotted for different RF power levels. Nanometers per pass (nm/pass) are used as the unit of deposition rate. Since the substrate does not face the plasma for the whole process, it is more appropriate to use the substrate holder movement (number of passes) instead of time. It was observed that increasing the pressure at constant power regimes resulted in lower deposition rates. This phenomenon is attributed to the fact that at lower deposition pressure, the concentration of less energetic molecules in the chamber becomes high, reducing the sputtering yield and thus resulting in lower deposition rates [56].

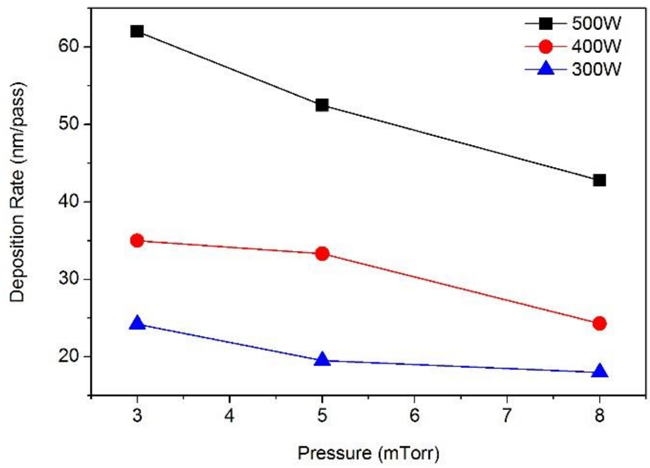

Figure 4.3 Effect of deposition pressure on AZO deposition rate for different deposition power. (Lines are drawn to guide the eye)

The influence of deposition pressure on the bandgap of the AZO films deposited on PET and glass substrate for different power levels is plotted in Figure 4.4. It is concluded that the deposition pressure has no significant influence on the bandgap of AZO for the selected DOE-1 range.

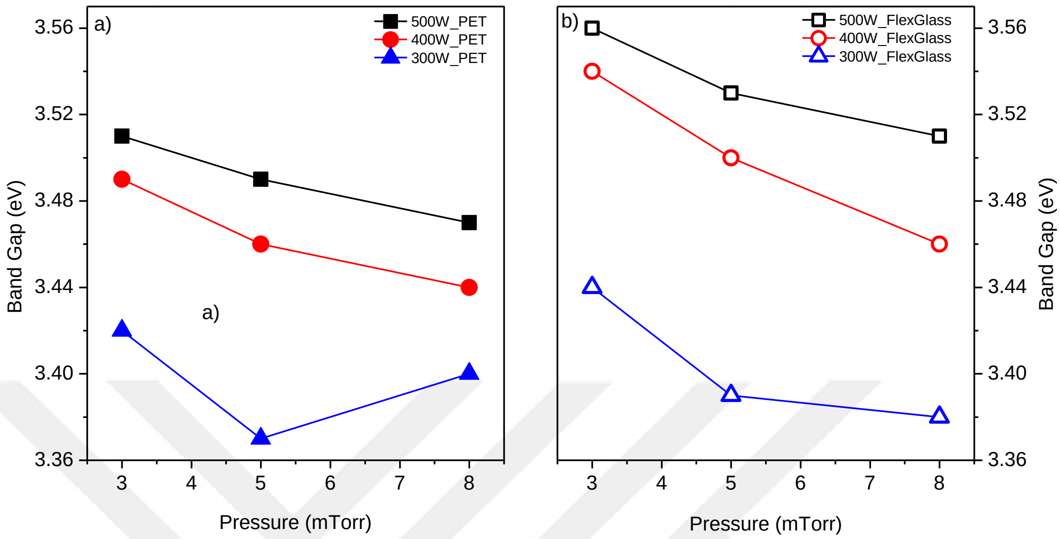

Figure 4.4 Effect of pressure on bandgap a) on PET substrates b) on flexible glass substrates (Lines are drawn to guide the eye)

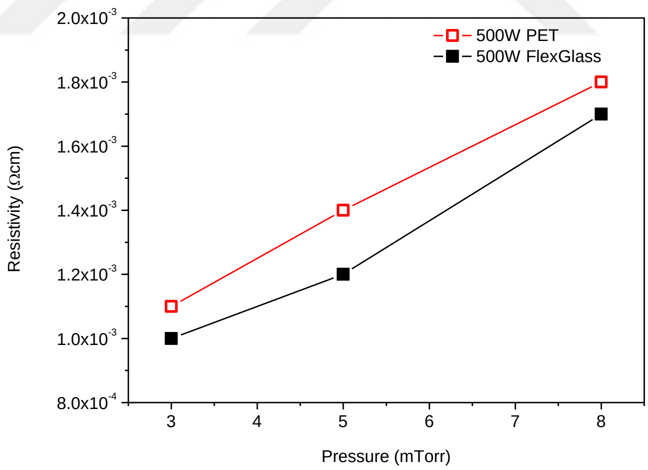

Figure 4.5 Effect of deposition pressure on measured resistivity of AZO films deposited onto ultra-thin flexible glass (black) and PET (red) substrates (Lines are drawn to guide the eye)

In Figure 4.5, calculated resistivity values are plotted with respect to three deposition pressure levels for the same RF power regimes. It was clearly shown that lowering the deposition pressure results in less resistive (more conductive) AZO films. At lower pressure levels with fixed power values, the radicals in the plasma medium have more energy; therefore, crystalline grains' continuity is higher, leading to fewer recombination centers [57].

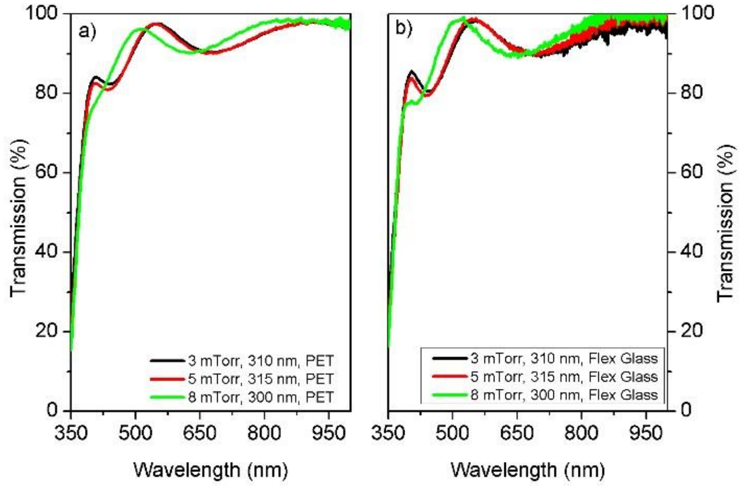

Figure 4.6 Effect of deposition pressure on the transmission of AZO films a) deposited onto PET b) deposited onto ultra-thin flexible glass

Transmission measurements can be seen in Figure 4.6. Deposition pressure improves the transmission of the AZO films in the UV region (between 350-450 nm). AZO films are optimized for the solar cell window layer in this study. This layer needs to have high transmission in the UV region to use the solar spectrum effectively. In Figure 4.6 b), the transmission of the film exceeds the 100% value, which can be explained by the systems tolerance values in these highly transmissive regions. Measurement systems have a 5% tolerance.

Depositions are also examined regarding changing deposition power with constant deposition pressure. RF power is varied from 300 to 500 W for the studied DOE-1, as seen in Table 4.1. The influence of power on deposition rate, bandgap of the material, and conductivity is investigated.

It is observed that RF power has a positive effect on deposition rate. Increasing the RF power at constant deposition pressure generates more energetic radicals and the energetic radicals in the plasma medium increase sputtering yield [30]. In Figure 4.7, this phenomenon is plotted.

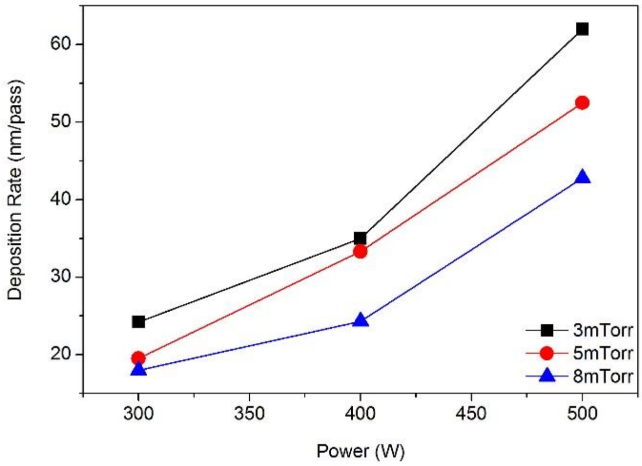

Figure 4.7 Effect of RF power on deposition rate (Lines are drawn to guide the eye)

Power dependency on deposition rate can be seen below in Table 4.5. Deposition rate increases with increased power, which results in more thick films

Table 4.5 The deposition rate and resistivity of AZO films with respect to changing power

Pressure	3 mTorr		
Power	300 W	400 W	500W
Thickness (nm)	145	210	310
Deposition Rate (nm/pass)	24.2	35	62
Resistivity of PET (Ωcm)	1.7×10^{-3}	1.6×10^{-3}	1.1×10^{-3}
Resistivity of UTFG (Ωcm)	1.3×10^{-3}	1.1×10^{-3}	1×10^{-3}

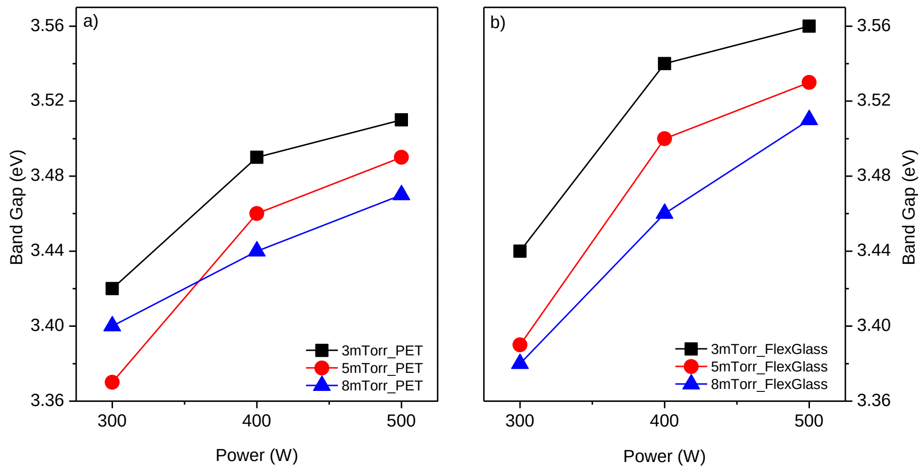

Figure 4.8 Effect of RF power on the bandgap of AZO films deposited on a) PET substrates b) ultra-thin flexible glass substrates (Lines are drawn to guide the eye)

In Figure 4.8, it is seen that the bandgap of the sputtered AZO increases with increasing the applied RF power. The carrier concentration increases at higher RF power levels, and thus the bandgap gets broadened. This phenomenon can be explained by the Burstein-Moss effect [58]. It is determined that the AZO films deposited onto ultra-thin flexible glass substrates showed slightly higher bandgap values when compared to the films deposited onto PET substrates.

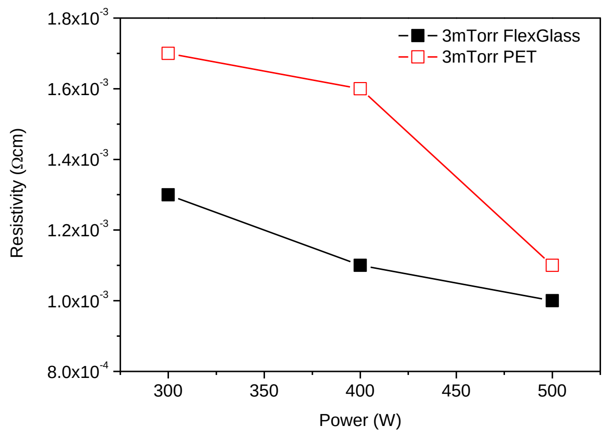

Figure 4.9 Effect of RF power on the resistivity of AZO films deposited on ultra-thin flexible glass (black) and PET (red) substrates (Lines are drawn to guide the eye)

The resistivity is related to the energy of the radicals in the plasma medium, as discussed before. As seen in Figure 4.9, the resistivity of AZO films reduces when applying higher deposition RF powers. The resistivity reduces dramatically, especially for AZO deposited on the glass substrate, when the applied RF power exceeds 400 W. It was observed that the AZO films deposited onto ultra-thin flexible glass substrates showed lower resistivity values compared to PET substrates. These resistivities in the order of 10^{-3} is compatible with literature [59][40][60].

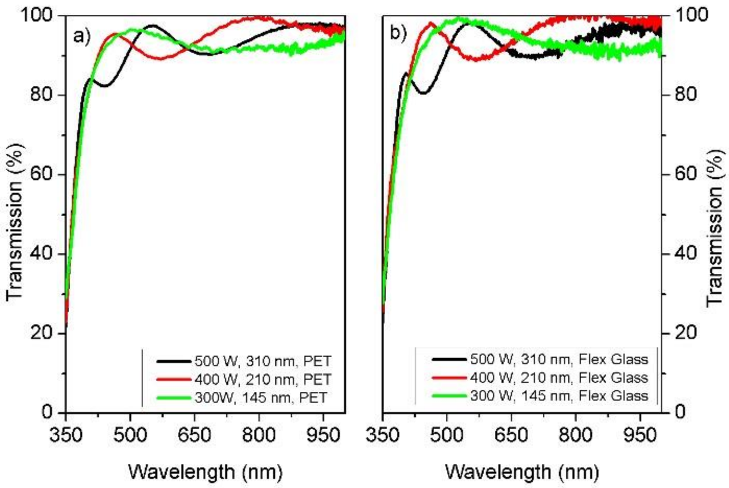

Figure 4.10 Effect of deposition power on the transmission of AZO films a) deposited onto PET b) deposited onto ultra-thin flexible glass

Transmission measurements can be seen in Figure 4.10. Since the thickness of the films is different, the effect of deposition power on transmission is not seen. However, if the films deposited at 500W and 400W are compared, films deposited at 500W are more transparent in the UV region. Figure 4.10 b), the transmission of the film exceeds the 100% value, which can be explained by the systems tolerance values in these highly transmissive regions. Measurement systems have a 5% tolerance.

4.1.1.2 Study of Different AZO Layer Thickness Characterization

Information obtained from the characterization of different AZO layers provides to optimize the device performance in the future. Characterization analysis includes optical and electrical analysis to gather optical and electrical properties of the films utilizing UV-Visible spectroscopy and four-point probe measurements. The thickness of the films was obtained by spectroscopic ellipsometry. Electrical characterization is done to find the conductivity of the thin film, and optical analysis is conducted to determine the bandgap of the AZO film and to investigate the transmissivity of the films. In this study, structural analysis is eliminated because the X-ray diffraction spectrometer is malfunctioning.

Samples are prepared as reported in Chapter 2. Previously optimized parameters for AZO deposition are used. Deposition parameters are given as follows;

- Fixed parameters: 500 W, 3 mTorr, 125 sccm Ar, Room Temperature

The only varying parameter is oscillation numbers, the number of passes under the AZO target. One number of the pass is that the sample passes under target twice and returns to its original position. AZO layers are deposited with 6 different thicknesses. Samples names are coded as AZO_t1 to AZO_t6. In order to obtain AZO layers with different thicknesses, holder movement is varied. The design of the experiment (DOE-2) and the number of passes are tabulated in Table 4.6.

Table 4.6 Varying deposition parameters of AZO for DOE-2

Sample Code	Number of Pass
AZO_t1	½ (Half pass)
AZO_t2	1
AZO_t3	2
AZO_t4	3
AZO_t5	5
AZO_t6	7

One forward and backward motion under the target during the deposition is called one oscillation. Half pass (one forward motion) is tried for the sample coded as AZO_t1.

The result of the characterization of thickness variation of AZO of DOE-2 is represented in Table 4.7. In this table, only the results from flexible glass substrate are given. Resistivity values are obtained from ellipsometry (SE) and four-point probe (4PP) measurements. In addition, SE measurements are also used to determine the thickness. Both measurements give similar results (except for the thinnest film).

Table 4.7 Comparison of spectroscopic ellipsometry and four-point probe for resistivity values

	Number of passes	Thickness (nm)	Resistivity (from SE) (Ω·cm)	Resistivity (from 4PP) (Ω·cm)	Bandgap (eV)
AZO_t1-2	1/2	32	2.3×10^{-5}	2.3×10^{-3}	3.319
AZO_t2-2	1	56	1.4×10^{-3}	3.4×10^{-3}	3.321
AZO_t3-2	2	115	1.2×10^{-3}	1.8×10^{-3}	3.465
AZO_t4-2	3	180	0.9×10^{-3}	1.4×10^{-3}	3.527
AZO_t5-2	5	304	0.7×10^{-3}	1×10^{-3}	3.518
AZO_t6-2	7	452	0.4×10^{-3}	1×10^{-3}	3.523

The dependence of resistivity on thickness is given in Figure 4.11. Resistivity decreases with increased layer thickness up to 100 nm, then stabilizes as expected, consistent with the literature.

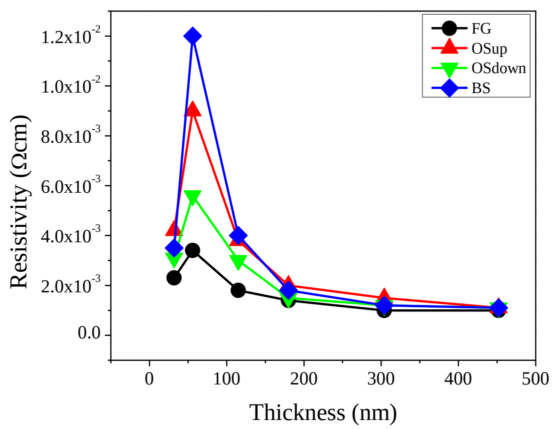

Figure 4.11 Relation between resistivity and thickness on different substrates

For optical analysis, the bandgap of each layer is calculated and reported in Figure 4.12. As seen from the results, when the thickness increases, the bandgap increases to a particular value, approximately 200 nm. After 200 nm bandgap of the films stays constant. It can also be concluded that resistivity is inversely proportional to bandgap; as the resistivity of the AZO layer decreases, bandgap increases. This change is not huge as expected since the doping concentration is not changing [61].

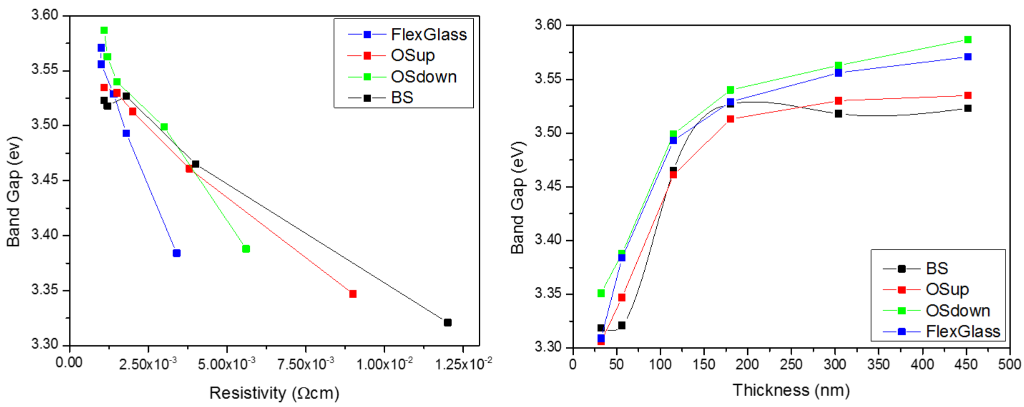

Figure 4.12 Bandgap relation with respect to resistivity and thickness

4.1.1.3 Study of Reactive Sputtering of AZO Layer

Another experiment set is designed to investigate whether the bandgap and refractive index of the material are changing with deposition gas changes. The change in refractive index is planned to be used in gradual refractive index change. The effective use of the solar spectrum that enters the solar cell can be adjusted by gradual refractive index change. Light entering the system and reducing its reflections, the refractive index of the mediums where the light passes is adjusted gradually.

Reactive sputtering is tested for the deposition of AZO layers. DOE-3 is given in Table 4.8. During the reactive sputtering experiment, oxygen is given as reactive gas for the first time in the GünEr system. Since this gas is used for the first time for deposition, there are unexpected circumstances such that the MFC of oxygen does not work correctly, so the flow rate cannot be set for the designed gas ratio.

Table 4.8 Design of experiments (DOE-3)

CODE	POWER	PRESSURE	TEMPERATURE	R (O_2/AR)
a1	400 W	5 mTorr	Room Temp.	0.1
a2				~~(0.5)~~ 0.23

For the first experiment, the temperature is set to room temperature. Power and pressure are fixed according to the previous AZO DOE-1 results. The gas ratios are obtained as follows; R=0.1, O_2:13 sccm, Ar: 125 sccm, R=0.5, is designed with flow rates of O_2:13 sccm, Ar: 125 sccm. The mass flow controller (MFC) for O_2 has a maximum range fixed at 50 sccm. After the second run, it is understood that the MCF of O_2 does not work correctly; thus, R=0.5 is changed. The second run is done at R=0.23 with flows O_2:23 sccm, Ar: 100 sccm.

The results of the reactive sputtering study are given in Table 4.9. Results show that the deposition rate reduces conductivity drastically when oxygen is introduced to the sputter. Also, the resistivity of the layers increased so that layers became non-conductive. It is concluded that the oxygen incorporation of the film changes the electrical properties of the Al:ZnO layers.

Table 4.9 The deposition rate and Resistivity of AZO films with respect to changing the gas ratio

Pressure	5 mTorr	
Power	400 W	
R (O_2/Ar)	0.1	0.23
Thickness (nm)	81.8	86.1
Deposition Rate (nm/pass)	13.6	14.4
Resistivity of PET (Ωcm)	21.6	NOT CONDUCTIVE
Resistivity of UTFG (Ωcm)	NOT CONDUCTIVE	NOT CONDUCTIVE

4.1.2 Multi-layer AZO

An antireflection coating for crystalline silicon solar cells reduces the loss of light. The loss mechanism of light can be managed by index matching. Multi-layer AZO is designed for matching the refractive index of air to the device. A gradient change of index will help to reduce the loss of light incoming to the solar cell.

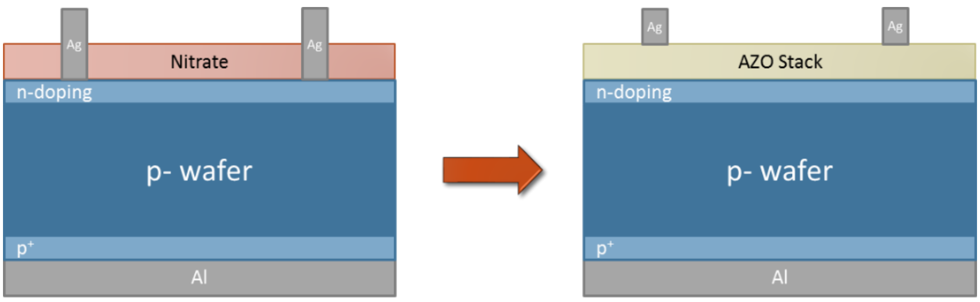

Figure 4.13 Schematic representation of the proof of the concept of multi-layer AZO applied on c-Si solar cell

A schematic representation of the proposed structure is seen in Figure 4.13. The nitrate layer is first replaced with a single layer of AZO layer. Then multi-layer structure concept is applied to the c-Si solar cell to see the graded refractive index effect. The refractive index of silicon is 3.1, and the refractive index of air is 1. A smooth transition from 1 to 3 can be achieved by varying the AZO refractive index with different layers.

This effect can be seen by investigating the reflection of the system. Reflection measurement simulation of single and multi-layer AZO on top of the c-Si cell is shown in Figure 4.14. (This simulation is done on web base calculator given in this link https://www.filmetrics.com/reflectance-calculator) The thickness of layers is decided according to the result of the simple simulation.

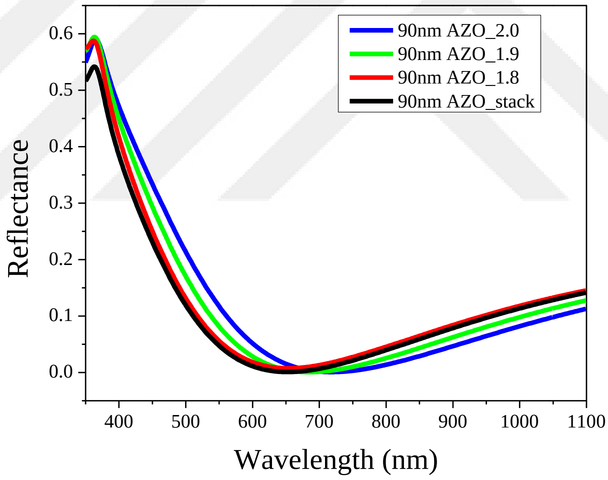

Figure 4.14 Reflection simulation of AZO layer on c-Si

The Refractive index of the AZO layer can be found from spectroscopic ellipsometry measurement. Three different layers are determined for the multi-layer stack from the previous single-layer characterization, as shown in Figure 4.15.

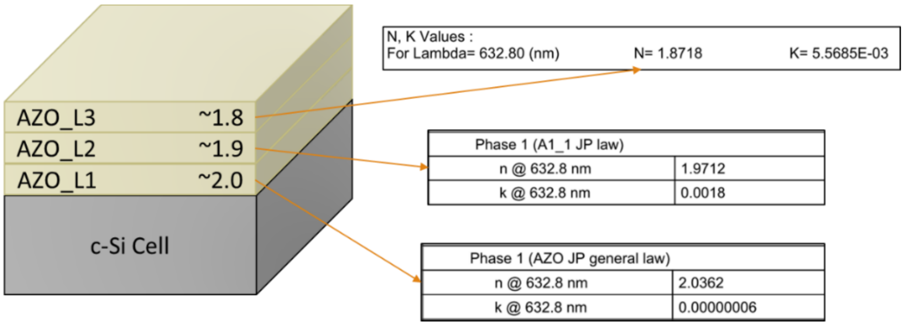

Figure 4.15 Multi-layer AZO design with different refractive indices

First, each layer is deposited on the c-Si wafer as a single layer. Then the multi-layer stack is produced and analyzed. The results of single-layer production are given in Figure 4.16. Results show that the thicknesses and refractive index of each layer changed.

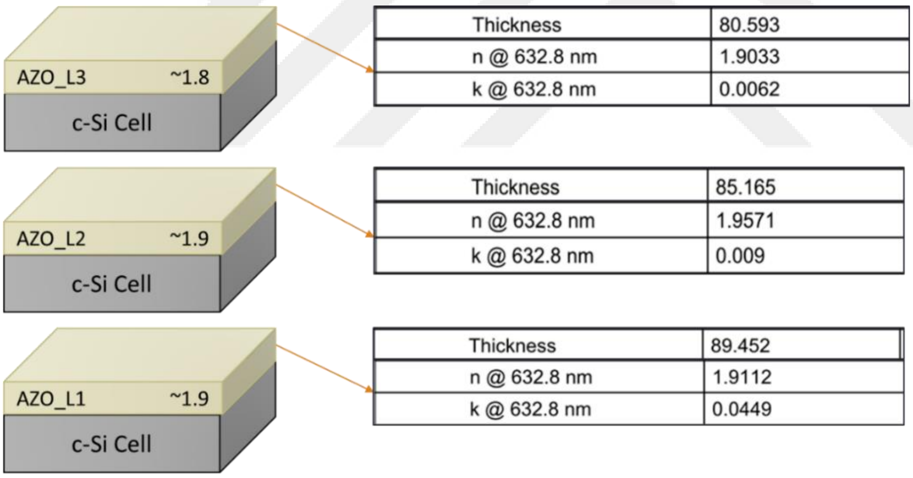

Figure 4.16 Thickness and refractive index of different single-layer AZO on c-Si cell

Reflection measurements are promising even if the refractive indices are not as expected. The reflection measurement of the multi-layer stack deposited on c-Si is given in Figure 4.17. The stack gives lower reflection results than single layers in the wavelength range between 700 and 1000 nm.

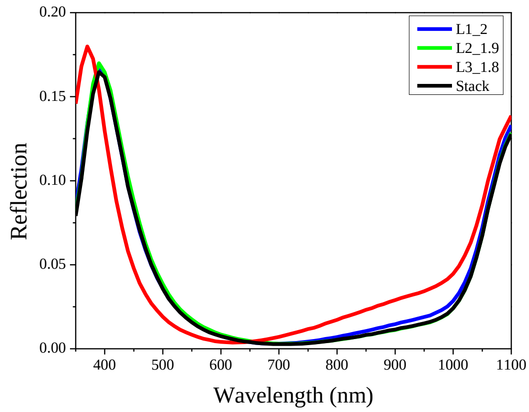

Figure 4.17 Reflection measurement of the multi-layer stack deposited on c-Si

4.1.3 Results and Discussion AZO Layer Optimization

As discussed in the previous section, all samples are analyzed to characterize different film properties. The following methods are used to examine thin films produced at GünEr:

AZO films are deposited onto ultra-thin flexible glass and PET substrates via RF magnetron sputtering with different deposition pressure and RF power levels. XRD analyses revealed that films deposited onto both substrates are c-axis oriented. It is observed that deposition pressure has a reciprocal effect on the deposition rate and material conductivity, whereas applied RF power has the opposite effect. Moreover, increasing RF power leads to the broadening of the bandgap of the material. The optimum deposition pressure and RF power are determined as 3 mTorr and 500W, respectively. The films deposited onto ultra-thin flexible glass substrates showed higher conductivity values. Thus, it is concluded that ultra-thin flexible glass is superior to PET in terms of AZO properties and also considering that withstanding higher substrate temperatures makes the ultra-thin flexible glass more preferable than PET flexible substrate in thin film solar cell fabrication.

The results obtained from the multi-layer study reveal that the thickness variation should be investigated according to the changing deposition parameters.

AZO films deposited onto ultra-thin flexible glass and PET substrates via RF magnetron sputtering were characterized by the different thicknesses of the films. Electrical analysis showed that increasing film thickness leads to a decrease in the resistivity of the films. It can also be concluded that resistivity is inversely proportional to bandgap; as the resistivity of the AZO layer decreases, bandgap increases.

State-of-the-art AZO thin films are deposited on thick glass substrates at a temperature exceeding 200 °C to obtain films with high transparency and low resistivity. However, it is a big challenge to obtain AZO thin films with superior electrical (in the order of 10^{-3}) and optical properties (high transparent in UV region) for PV application at low deposition temperature compatible with the used flexible glass and plastic substrates. Results show that AZO thin films can be deposited with superior optical and electrical properties at low temperatures (room temperature) without affecting the considered flexible substrates.

4.2 Texturing of AZO

Light management done at the device entrance enhances the light absorption of a thin film solar cell. The first layer, the transparent conductive oxide layer, is textured, or the substrate can be textured. Texturing helps to reduce scattering and enhance light entering the absorber layer. Parameters such as texture size and periodicity are essential features for texturing.

Conventionally the texturing of AZO is done by wet chemical etching [49]. Wet chemical texturing has the advantage in the applications of large-area samples. Various etchants such as HCl, HNO_3, HF, HN_4C are used for texturing the surface [62], [63], [64]. The etchants used for texturing can be used for substrates such as glass. However, most of the etchants damage the substrate itself for plastic substrates. Thus alternative methods are used for plastic substrates. Texturing with a laser has the advantage of minor substrate damage. In addition to that, periodicity control gives the freedom for texture patterns. Different patterns are used in literature for light trapping. Typical usage of industrial laser applications makes it possible for large-scale applications [65], [66], [67], [68].

Here in this report, the main focus is to obtain surface texturing of AZO films deposited on two different flexible substrates for photovoltaic applications. First, surface texturing of the back contact layer is studied by wet chemical etching.

4.2.1 Wet Chemical Texturing of AZO by Hydrochloric Acid (HCl)

Several light management techniques do enhancement of light absorption in thin film solar cells. Surface texturing is one of the most common techniques utilized in light management. TCO layer and/or the substrate itself can be textured to reduce scattering and thus enhance the optical path length of incoming light in the absorber layer.

Silver and aluminum-doped zinc oxide layers are deposited in the sputter system; the details of depositions are given in Table 4.10. Samples are prepared on ultra-thin flexible glass. 600 nm of AZO is deposited onto 100 nm of Ag.

Table 4.10 Deposition Parameters of Ag and AZO Back Reflector

Deposition Parameters	***Silver***	***AZO***
Ar Flow rate	175	125
Dep. Pressure	5 mTorr	3 mTorr
Dep. Power	300 W	600 W
Dep. Temperature	R.T.	150°C

Experiments are designed such that the AZO layer is textured in %1.8 HCl solution for 5, 10, 15, 20, and 30 seconds. Textured samples are analyzed optically to determine the effectiveness of the resulting texture. The effectiveness of the textured surface is analyzed via transmission and haze measurements. In addition, layers are also characterized structurally via SEM and AFM. Results of structural analysis are given in Figure 4.18, and optical analysis results are given in Figure 4.19.

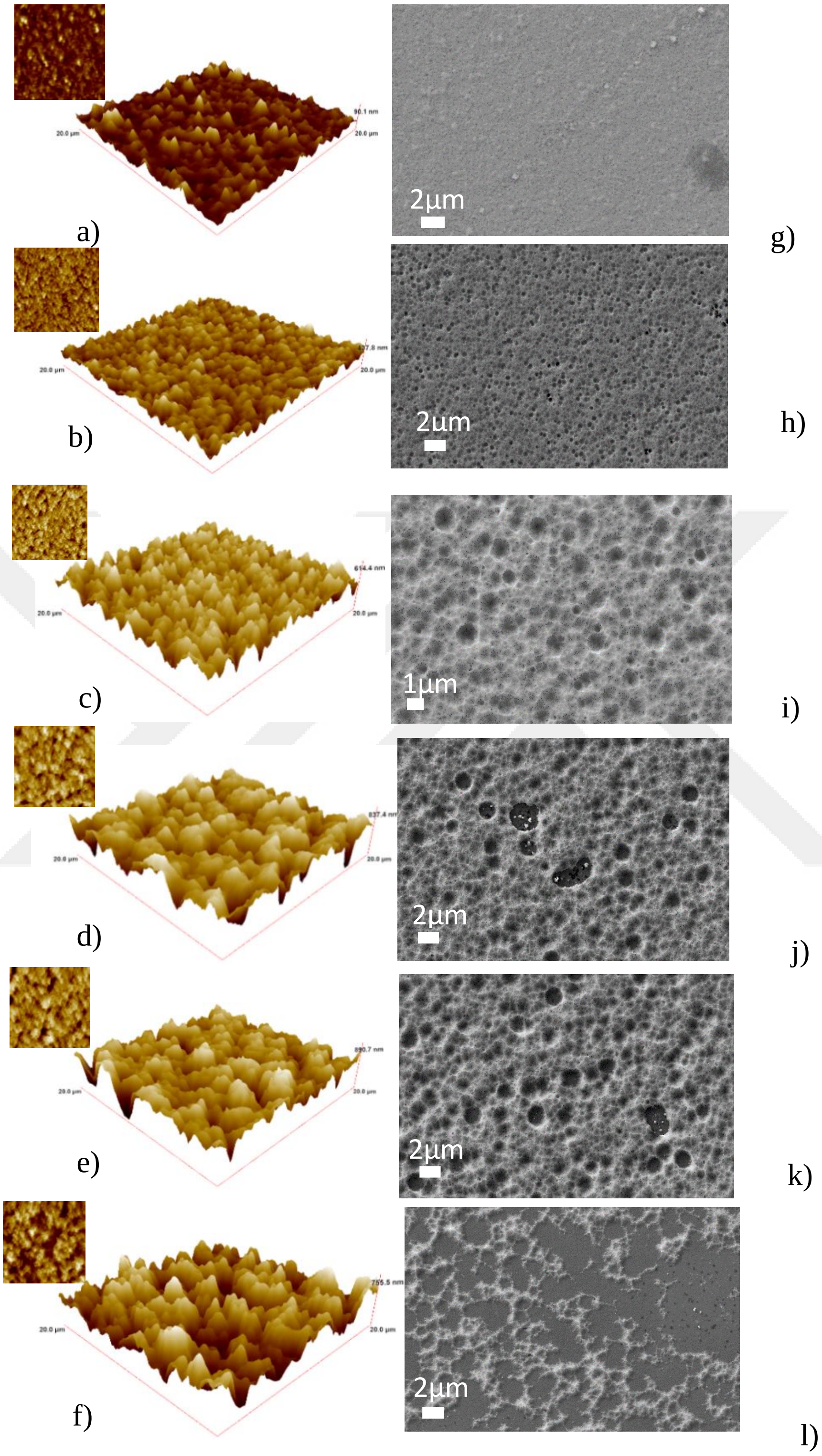

Figure 4.18 a-f) AFM images of the reference sample and etched 5s, 10s, 15s, 20s, 30s samples, respectively g-l) SEM images of the reference sample and etched 5s, 10s, 15s, 20s, 30s samples, respectively

Surface analysis results are given in Figure 4.18 a-f) AFM images of the reference sample and etched 5s, 10s, 15s, 20s, 30s samples, respectively, wherein Figure 4.18 g-l) SEM images of the reference sample and etched 5s, 10s, 15s, 20s, 30s samples respectively. The top left image in AFM images is the top view of the surface. The surface roughness of the reference (as deposited) sample is 9.6 nm. Surface roughness is increased with increasing etching time. As the etching time increases, the size of the features goes deeper and broader. After a particular time, features start to cluster. 30 s etching time shows that clusters that appear on the surface are etched through to the silver layer. It also explains the high reflectance measurement obtained from that sample.

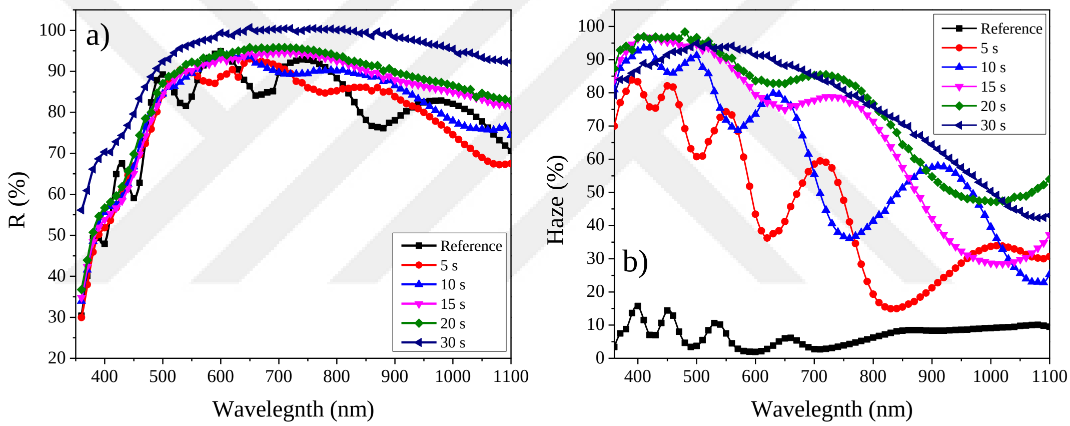

Figure 4.19 a) Total reflectance b) Haze vs. wavelength of wet chemical texturing of AZO

Total and diffuse reflectance measurements are done with the integrated sphere—results as shown in Figure 4.19, more than 90% of haze can be obtained by this method. However, reflectance values should be compared with the surface analysis to explain more than 95% haze. Samples etched for 5 and 10 seconds show interference peaks since the thickness of the AZO layer is relatively high. Also, samples etched for 15 and 20 seconds show broadening in the visible region, desired for a back reflector.

Surface roughness can be incorporated with haze values obtained from the optical analysis. Results are given in Figure 4.20.

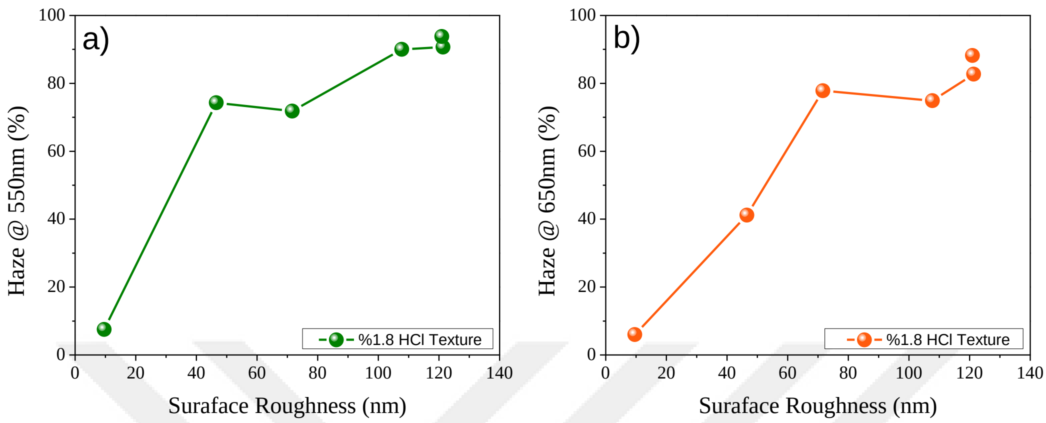

Figure 4.20 Effect of surface roughness on haze a) at 550nm b) at 650 nm

Conventional wet chemical etching is applied to silver aluminum-doped zinc oxide back reflectors to have high reflectance in the visible range of the spectrum. Optical analysis showed that 43% of haze value could be obtained by laser texturing. More than 90% of high haze is obtained from the HCl texturing of the back reflector. A reflection improvement is observed in between the range 600-800 nm.

4.2.2 Laser Texturing of AZO

The focus of this study is to compare the surface texturing of AZO thin films deposited on ultra-thin flexible glass (<100 µm) substrates by RF magnetron sputtering for thin film photovoltaic applications obtained with different laser parameters operating at different wavelengths. The laser source used in this study is HIPPO Spectra-Physics laser, which is a diode-pumped solid-state (DPSS) Q-switched laser. The laser system operates in three different wavelengths, which are ultraviolet (UV-355 nm), green (532 nm), and infrared (IR-1064 nm). The laser beam operates at TEM00 spatial mode with less than 15 ns pulse width at 50 kHz. The repetition rate of the laser can be varied from 15 kHz to 300 kHz. Average laser power at 50 kHz is 5 W, 11 W, and 17 W for UV, green, and IR.

The sample is placed on a moving stage (y-axis) which is stationary during the process. The focusing optics are placed on another stage controlled by a linear motor with speed varying between 1 to 600 mm/s.

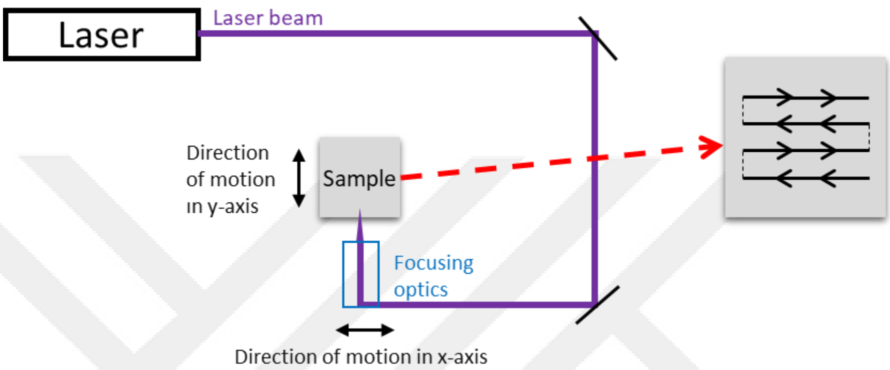

Figure 4.21 Laser system used for AZO texturing

Figure 4.21 shows the schematic of the laser system used in this study. Textures are obtained by scanning the sample surface with a motor-controlled stage. The motor stage carries the focusing optics. Focusing optics move only on one axis while the sample moves in the other direction so that a specified area is scanned line by line. Vertical periodicity is obtained by determining the distance between each scan line.

AZO surfaces are imaged by a Scanning Electron Microscope, SEM (ZEISS, EVO HD15). Average surface roughness values of laser processed AZO are obtained using an optical surface profiler (Zygo ZeGage Plus). Transmission measurements are done using an in-house optical setup containing an integrating sphere, a monochromator, and a silicon detector, as described in Chapter 2. Total and diffuse transmission measurements are performed using an optical setup built around an 8-inch, 5-port integrating sphere (Oriel 70679NS). The transmittance haze (H), defined as the ratio of diffuse to total transmittance, is calculated by post-processing the diffuse and total transmission data from each laser processed AZO.

The laser parameters (i.e., diode current, repetition rate, motor speed) are tuned to change the incident power on the sample. Incident power is arranged such that no damage forms on the substrates. From initial studies, it is deduced that incident power should be as low as possible. Since the power of the laser is too high, a green laser is used with an attenuator to decrease laser power more. The green laser is used to study drilling mode and single layer scan through textured glass. All other types of laser, together with green, are used for dual laser scans.

The laser follows a straight line as it moves during the scribing mode to obtain uniform ablation along the line. However, single spots along the scribe line can be obtained by arranging laser repetition rate and motor stage. Increasing repetition rate (RR), which is the frequency of the laser spot (f), can decrease the distance (d) between each spot at a particular motor speed (v). A schematic illustration of pulsed laser patterning of laser lines can be seen in Figure 4.22. The relation between the parameters is given as d=$\frac{v}{f}$ [69].

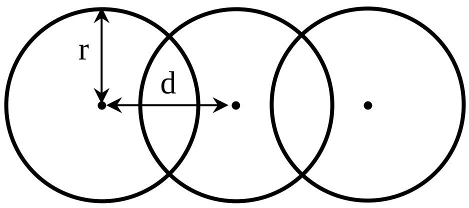

Figure 4.22 Schematic illustration of pulsed laser patterning of laser lines

Separated spots instead of a continuous line can be obtained by arranging parameters of RR, and v. Scan line is limited by RR and the maximum speed of the motor stage, which is 600 mm/s. According to this limitation, RR is fixed to 20 kHz. To reduce thermal damage and remain residues on the substrates, the power of the laser is arranged as low as possible. An attenuator helps to reduce the laser power. In addition to that, another option to change/reduce laser power in the system is to change polarization since laser sources produce polarized light. After these main adjustments, power can be varied by changing current values. Another parameter that can affect the power indirectly is the repetition rate.

4.2.2.1 Drilling Mode (t-DOE-1)

Drilling mode experiments are designed to obtain periodic structures. The first experiment set is designed to optimize laser parameters affecting power during drilling. Laser shooting time and current supplied to the diode are varied. The design of the experiments is given in Table 4.11. However, the processing time for the drilling mode takes too much time, so it takes approximately 1 hour to scan a 1x1 cm^2 area. The application of such a process on a large scale is not feasible.

Table 4.11 Design of experiments for drilling mode (t-DOE-1)

Repetition Rate (kHz)	Current (A)	Laser Shooting Time (ms)
20	36-38	8
20	26-28	8
20	26-28	10

Investigation and characterization of these holes are done via SEM, and results are given in Figure 4.23. As can be seen from the images, the shape of the holes is not perfectly circular. The spots shown in Figure 4.23 are three consecutive spots processed in one step. The laser hits several times; thus, it damages the substrate surface. In addition, the power transferred to the layer changes during the process, resulting in different ablation. In Figure 4.23 b) the third spot did not even form. The approximate diameter of the holes varied from 30 μm to a minimum value of 11μm.

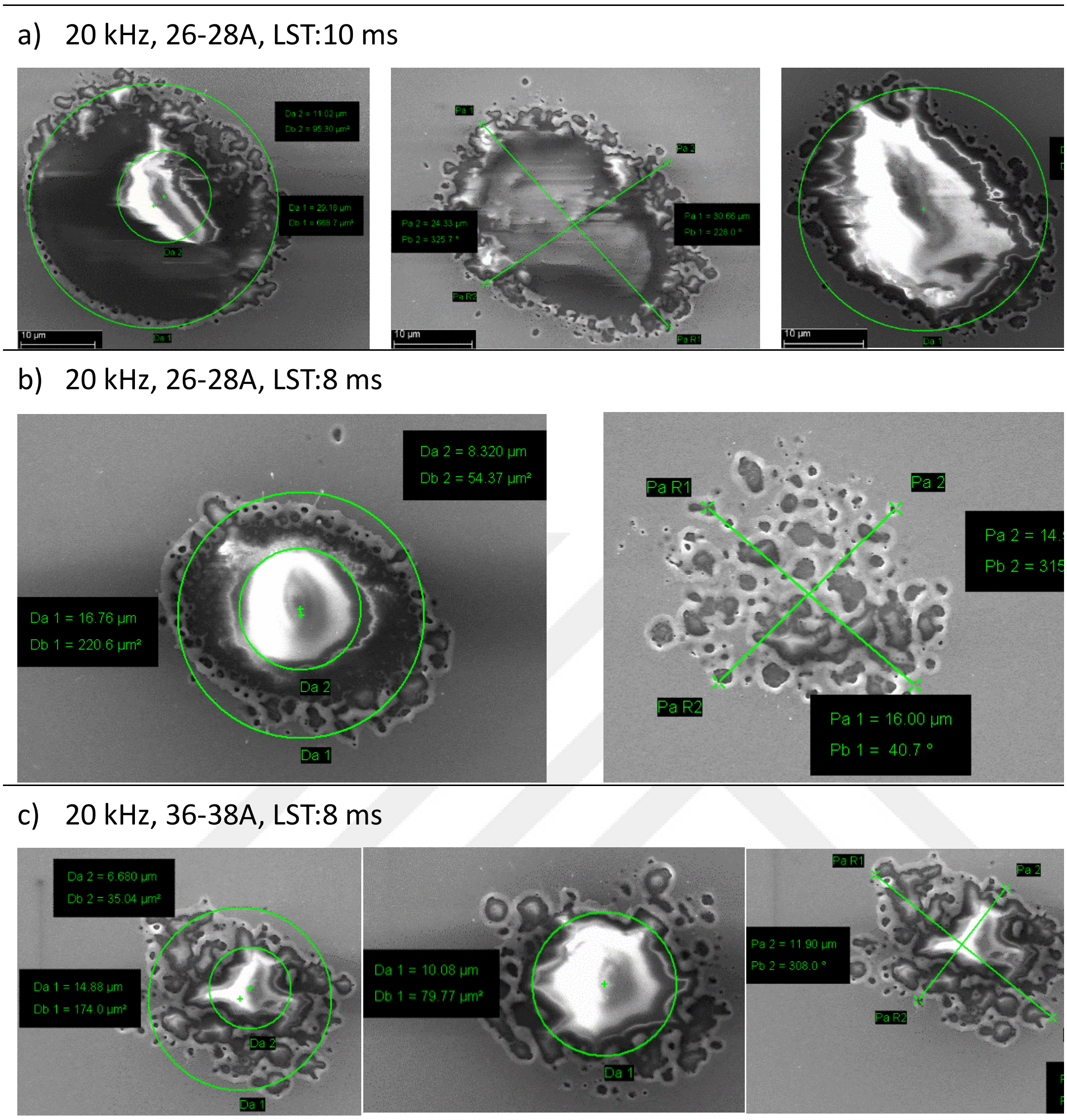

Figure 4.23 Results of t-DOE-1 concerning the changing parameters

4.2.2.2 Scribing Mode (t-DOE-2)

Laser texture through already textured glass study

From the results of the drilling study, it is seen that laser damage done by the laser to the substrate is very high. Two other concepts are proposed and experimented with scribing mode. The first study proposes further reducing laser power by placing a material that will enter the light path but not block the light's passage. A piece of glass is used for this purpose since the wavelength of the laser is 532 nm is used. A glass piece is used and placed in front of the sample. Already textured glass is used to see the effect on laser texture. The textured surface is placed on the AZO layer, and the laser focuses on the interface. The concept can be visualized in Figure 4.24.

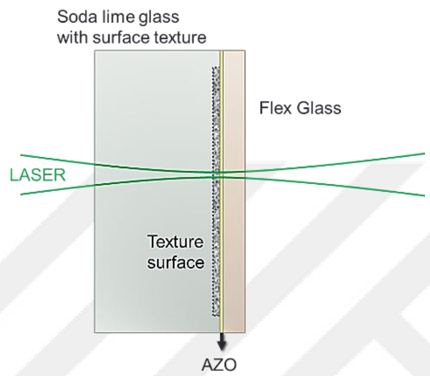

Figure 4.24 Schematic of laser texture through the already textured surface

The second proposed concept is targeted to reduce/eliminate laser damage. After opening periodic holes through the first thin AZO layer, another relatively thick AZO layer is deposited onto the first layer. Process steps can be seen in Figure 4.25. Structural, optical, and electrical analysis of layer characterization is done. Total transmission and direct transmission are measured for haze calculation, and the results are represented in the next section.

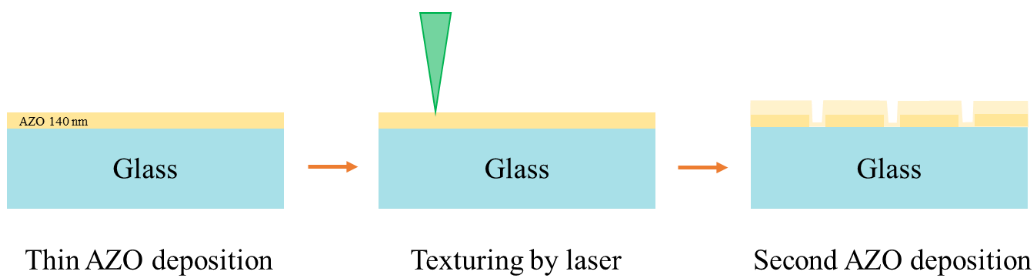

Figure 4.25 Process flow of AZO laser texture

t-DOE-2 set according to frequency (repetition rate), diode current, and motor stage speed is given in Table 4.12.

Table 4.12 Design of experiments for scribing mode (t-DOE-2)

FREQUENCY	CURRENT	M. S. SPEED
20 kHz	24-26 A	600 mm/s
		300 mm/s
		100 mm/s
20 kHz	22-24 A	600 mm/s
		300 mm/s
		100 mm/s
		5 mm/s

After laser parameters are optimized for AZO laser texturing, a glass substrate area of 1x2.5 cm^2 is scanned. The sample used for this study is ultra-thin flexible glass. Since the laser ablates all the layers up to the glass, another layer is deposited onto the textured layer. Mounting plastic substrates to the laser system is an issue because of the curved surface of samples. During the laser process, bent structures become out of focus, resulting in non-uniformities along the scribe line. Plastic substrates will be studied after finding a proper mounting system.

Parameters in terms of line distances are optimized to have periodic holes. The optimum diameter of the holes is ~20μm, and the pitch is 30 μm. For this laser, parameter pitch is fixed; however, hole diameter can be changed by changing the thickness of the deposited AZO layer. Thickness optimization should be done for the second AZO layer deposition.

A power variation study is done on a 140 nm thick AZO layer. Samples used here are 6 months old AZO samples deposited for layer characterization and are used as-deposited (without any cleaning). Diode current is varied from 36-38A to 24-26A with the polarizer. The optimum polarizer angle is found at 36°. Repetition rate (frequency) is varied from 15 kHz - to 30 kHz, and motor stage speed is used in two steps, 600 mm/s and 300 mm/s. Frequency and motor speed are arranged as discussed in Section 2.2.1.

After some of the laser parameters are fixed, already textured glass is used. During the laser texturing process, it is observed that residues coming out of laser ablation are stuck on the textured glass. The textured glass needs to be cleaned after each laser process. For only one line, process cleaning is not an issue. However, after scanning a large area, some of the residues stuck on the textured glass cannot be removed by simple cleaning (acetone, alcohol, and DI water cleaning). Cleaning with other etchants can affect already textured glass surfaces so that it impinges on reproducibility. As a consequence of reproducibility, laser texture through the already textured glass concept is not carried on, even though SEM analysis is promising.

An optical microscope or the camera of the laser system is used at first glance. The surface image is taken via the camera of the laser system. A sample is illuminated with infrared light to take a clear image. Scribe lines of laser texture through already textured glass are seen in Figure 4.26. The first five lines are examples of laser texture through the already textured glass concept. The last two lines are trials for direct laser texture. Some of the lines are not visible to visible light; thus, further characterization of these structures is done via SEM.

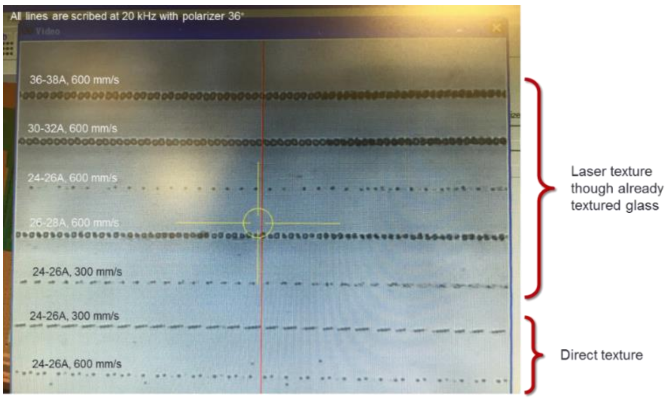

Figure 4.26 Screenshot of the camera image of the laser system of scribe lines after laser texture

SEM images show that texture though already textured glass concept, is promising, as seen in Figure 4.27. By this concept, random texturing can be possible instead of periodic texture. At the interface, focused laser light is scattered with the help of a textured surface and ablate layer accordingly. In different power conditions, laser damage to the layer differs. The damage is more at the center of the focused beam for high power settings and gets less for the scattered light (see Figure 4.27-c). By reducing power, the focused beam can scatter more, and the effect of scattering light on the layer gets wider (see Figure 4.27-d). Effects of different parameters can be seen in Figure 4.27-b, where the surface characterization of laser scribes is done through the textured surface.

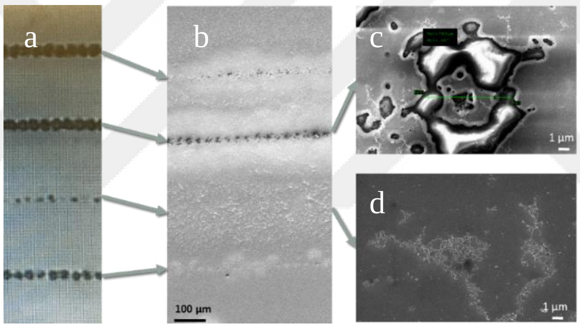

Figure 4.27 a) Laser camera image b) SEM image c-d) detailed SEM images of the laser scribe lines

Direct Laser Ablation and HCl cleaning study

The previous study concluded that 20 kHz frequency and 24-26A current at 532nm wavelength are the optimum parameters for texturing. The influence of motor stage speed on laser spots can be seen in Figure 4.28. In Figure 4.28 a), the center to center distance is 15 µm, and the pitch is ~7 µm. Hole diameter varies in the range of 10-15 µm. However, the texture is not consistent throughout the scribe line. The most unstable condition is the hole depth. In Figure 4.28 a) below, holes are not reaching through the glass, which is favorable. Another issue is the discontinuity of the spots.

Spot depth is also affected by the film thickness. In Figure 4.28 b) bright areas are seen in the image are the glass, which is due to its charging property. It means that holes are reaching the glass substrate.

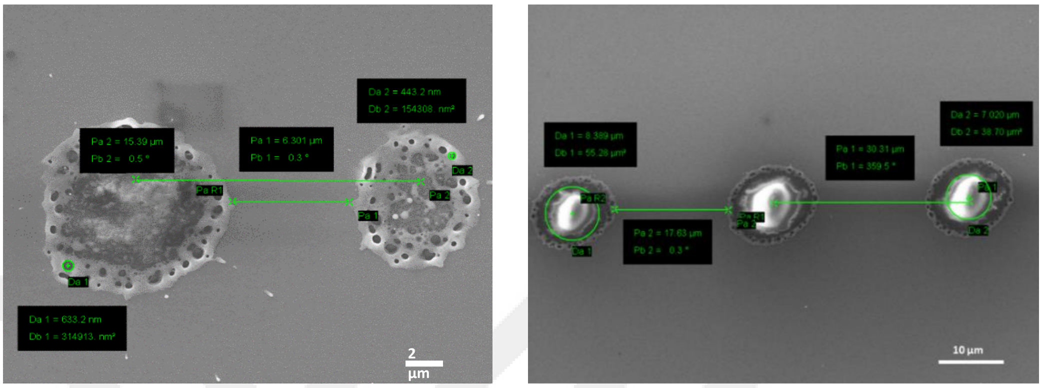

a) *20 kHz, 24-26A, 300 mm/s* **b)** *20 kHz, 24-26A, 600 mm/s*

Figure 4.28 SEM images of the textured surface of 140 nm thick AZO showing variation of motor speed

The structural and electrical analyses and SEM images are given in Table 4.13. According to the results obtained from the power variation study, the best holes are achieved with a repetition rate at 20 kHz, diode current at 24-26A, and motor stage at 600 mm/s. By using these parameters, two areas are scanned with different line spacing. In order to arrange periodicity, two different line spacing is applied. Line spacing is 30 µm and 200 µm for areas 1 and 2, respectively. Center to center hole spacing is the same for both scanned areas that are 30 µm for fixed frequency and the motor stage speed. Both samples also have the same hole diameters of 20 µm. Sheet resistances are increased after the laser process. This phenomenon is due to nonuniformity and misconnections formed by holes that reach the glass substrate.

Table 4.13 Results of structural and electrical analysis of scanned areas

	AREA-1	AREA-2
	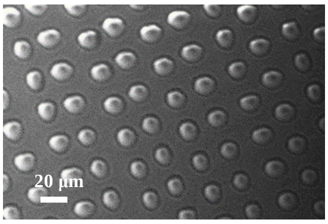 	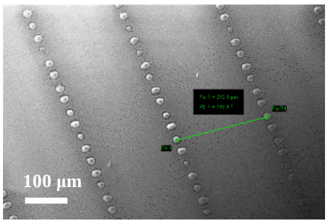
Hole diameter	~20 µm	~20 µm
Hole spacing	30 µm	30 µm
Line spacing	30 µm	200 µm
Sheet Resistance	Before Texture: 59 Ω/□ After Texture: 100 Ω/□	Before Texture: 55 Ω/□ After Texture: 61 Ω/□

Textured areas are analyzed optically via the integrating sphere (IS). Here in Figure 4.29, results are given in two different IS set-ups. IS system can be arranged in two different configurations since it has two ports. One of the ports is near to detector. Two measurements from two different set-up configurations are compared to see the effects on results. Results show that both systems can be used for low haze measurements.

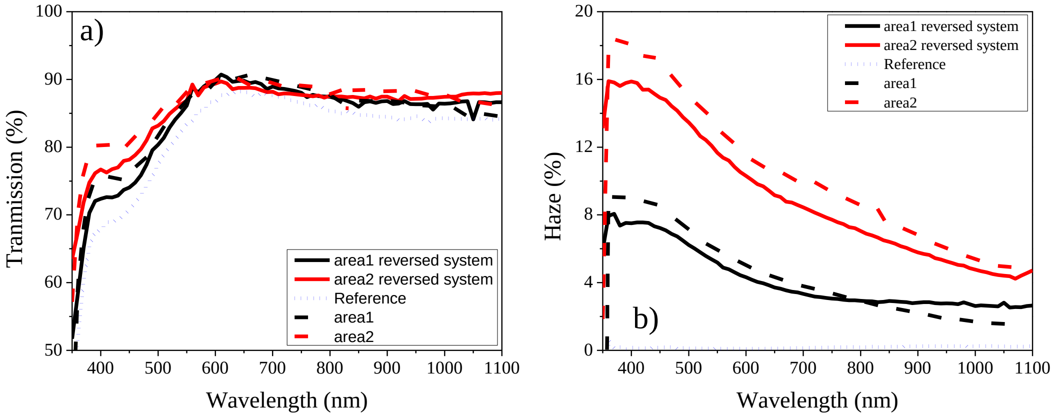

Figure 4.29 Measurements obtained from two different IS configurations a) total transmission b) haze

From the surface characterizations, it is observed that after laser ablation, residues remain at the edges of the holes, as seen in Figure 4.30 a). HCl cleaning is done for scanned samples with the best laser parameter as Area-1. 0.25% HCl solution is prepared for cleaning. Dipping time is varied in four steps: immediate dipping (DIP), 5, 10, and 15 seconds. Residues are cleaned for the sample that is dipped for 15 sec. Crack formation is started at the edges of the holes, as seen in Figure 4.30 b) in addition, after 10 sec. AZO layer starts etched by HCl. Direct and indirect transmission is measured given in Figure 4.30 to see their contribution to haze

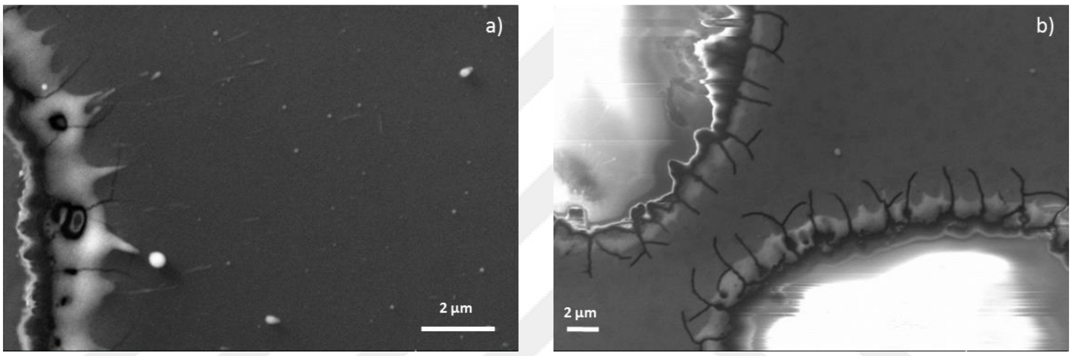

Figure 4.30 Residues after laser process are cleaned by HCl a) reference as textured b) after 15 sec. HCl cleaning

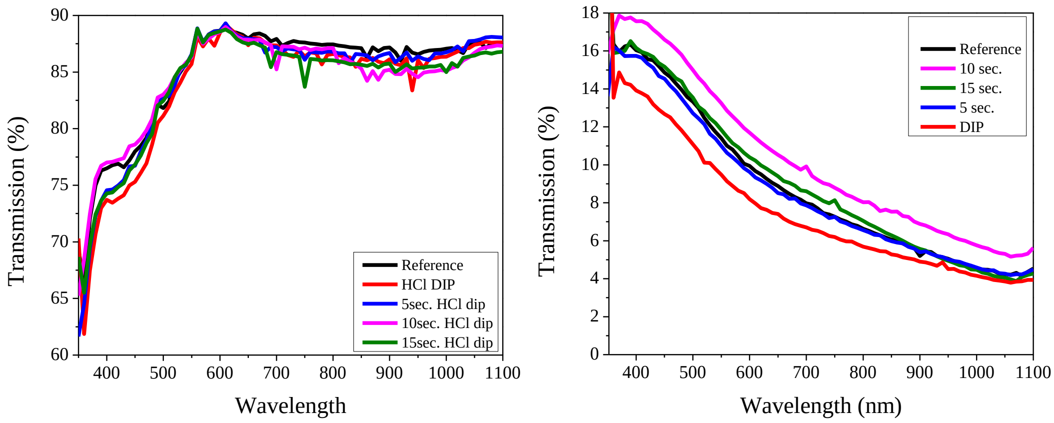

Figure 4.31 Transmission measurements for sample cleaned in HCl solution after laser texture

Double layer AZO deposition is studied in two steps. The first step is to deposit a thin (~140 nm) AZO layer and direct laser texture. It is then depositing a relatively thick AZO layer on top to reduce surface deficiencies and enhance the resistivity of the TCO layer.

The same samples are used here for comparison. A comparison study of electrical analysis is done for this experiment set. Sheet resistances are measured before laser texture (as deposited). Then laser texture is applied before the second AZO deposition. Another measurement is done after the thick AZO layer is deposited. The results of the electrical analysis are given in Table 4.14. Also, the transmission measurement results are shown in Figure 4.32, even though the sheet resistances reduction results in a loss of film transparency.

Table 4.14 Sheet resistance values before texture as-deposited single layer and after 400 nm AZO deposition

	Reference	*HCl DIP*	*5 sec.*	*10 sec.*	*15 sec.*
Single-layer as dep.	60 Ω/□	55 Ω/□	57 Ω/□	58 Ω/□	57 Ω/□
After second layer dep.	6.6 Ω/□	8 Ω/□	7.6 Ω/□	7.1 Ω/□	7.5 Ω/□

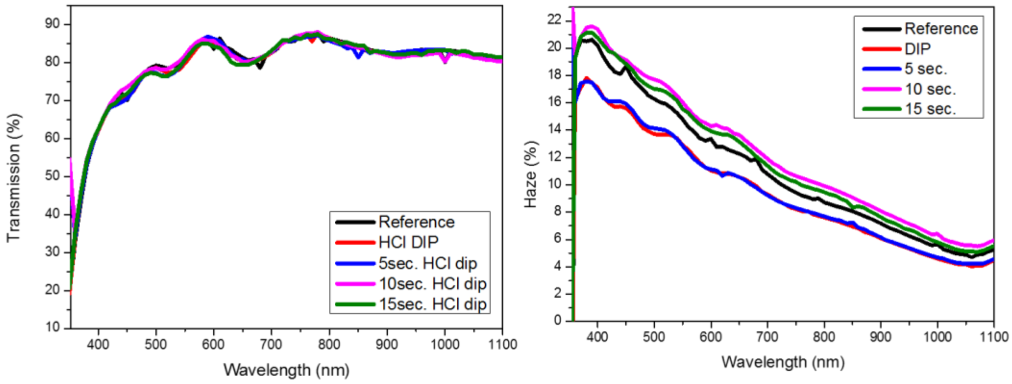

Figure 4.32 Transmission measurements after second AZO layer deposition

Different studies are conducted to improve the quality of the laser process. Results reveal that additional HCl cleaning is not necessary. Such an application can be considered after optimizing all other parameters like the thicknesses of the films. HCl cleaning will introduce more complexity to the whole texturing process. In a second study for texturing, results showed that second layer deposition is essential in reducing the value of sheet resistance of the TCO layer. In addition to that, by controlling thicknesses, transparency can be arranged for a conductive layer.

4.2.2.3 Scribing Mode (t-DOE-3)

Laser texturing is studied on 1.2 micron thick AZO samples. AZO is deposited on a 25x25 cm^2 ultra-thin flexible glass substrate.

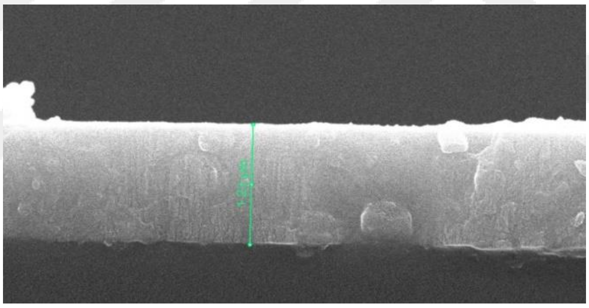

Figure 4.33 AZO deposited on the flexible glass substrate

A 1.1 mm thick dummy glass is placed onto the sample holder to support the flexible glass. It is observed that the dimensions of the flexible glass substrates ordered from Schott are greater than 25x25 cm^2 during the first time of the full-size AZO deposition. The ultra-thin flexible glass is resized and used as one piece for the deposition. After the deposition process, the AZO layer is cut into small pieces and used for laser applications. Deposition parameters are given in Table 4.15.

Table 4.15 Deposition Parameters of thick AZO samples

Deposition Parameters	***AZO***
Ar Flow rate	125
Dep. Pressure	3 mTorr
Dep. Power	600 W
Dep. Temperature	R.T.

Surface analysis is carried out to investigate feature size and surface condition before and after the laser process.

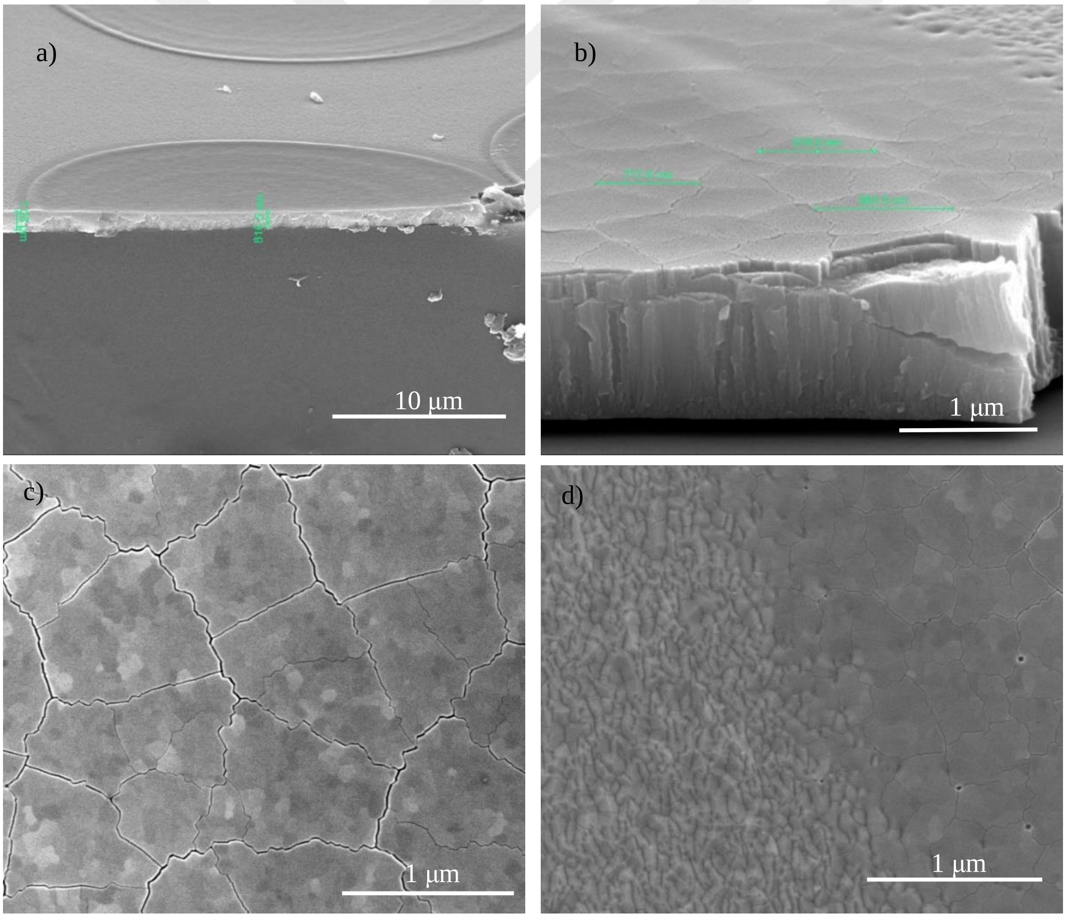

Figure 4.34 a) Cross-section view of the laser spot b) Surface of the laser-treated area c) top view of laser spot d) edge of the laser spot

Right after laser irradiation, the surface of the samples is examined in detail via an optical microscope. After initial surface analysis with an optical microscope, selected parameters are used to scan an area of 0.9x3 cm^2.

Table 4.16 Design of Experiments for Laser Texture Optimization Set (t-DOE-3)

Line #	***Frequency***	***Current***	***Motor S. Speed***	***Line Separation***
1	15 kHz	18-20 A	600 mm/s	20 µm
2			450 mm/s	20 µm
3		20-22 A	600 mm/s	30 µm
4			450 mm/s	30 µm
5		26-28 A	600 mm/s	30 µm
6	20 kHz	24-26 A	600 mm/s	30 µm
7		26-28 A	600 mm/s	30 µm
8		28-30 A	600 mm/s	30 µm
9	30 kHz	20-22 A	600 mm/s	20 µm
10			450 mm/s	20 µm
11			300 mm/s	20 µm
12			100 mm/s	20 µm
13		22-24 A	600 mm/s	30 µm
14			600 mm/s	20 µm
15			450 mm/s	15 µm
16		24-26 A	600 mm/s	30 µm
17		26-28 A	600 mm/s	30 µm
18	50 kHz	24-26 A 24-26 A	600 mm/s	30 µm
19			600 mm/s	20 µm
20	100 kHz	26-28 A	600 mm/s	30 µm

After laser illumination, as seen in Figure 4.34 a), 33% of the layer is etched by laser. Etching of AZO layer depends on laser parameters such as diode current, in other words, incident light power. After laser texturing, minor cracks are observed on the surface of the film. These cracks can be seen in Figure 4.34. The cracks are formed as a result of absorbed energy. If the cracks are deep enough, those cracks can cause delamination or discontinuities of the film. The best way to determine whether the crack is deep enough to cause delamination is to measure the resistivity (or calculate conductivity). Thus sheet resistance values are checked after each process.

Scan areas are further analyzed optically via SEM imaging. According to the t-DOE-3 given in Table 4.16, 20 different scans are applied by laser. The total and the diffuse transmission is measured from the scanned area to calculate the haze value of the textured AZO layer.

After the surface analysis, a 1x3 cm^2 area is scanned with selected laser parameters. Each scanned area is optically investigated to obtain the maximum haze value. A comparison of current, frequency, and line separation is studied. The results of t-DOE-3 are given in Figure 4.35 and Table 4.17.

Table 4.17 Effect of Frequency on texturing

	26-28 A, 600 mm/s, 30 μm separation		
Sheet Resistance	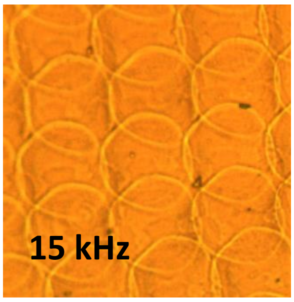	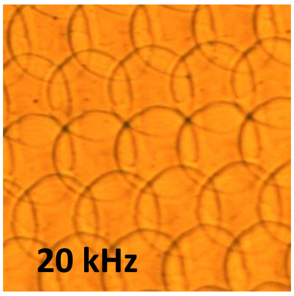	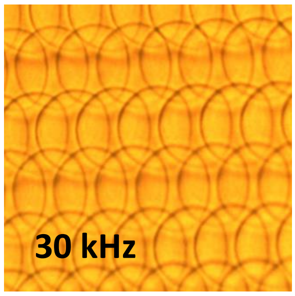
Before	4.3 Ω/□	3.7 Ω/□	3.4 Ω/□
After	5.6 Ω/□	5.4 Ω/□	5.4 Ω/□

Sheet resistance values given in Table 4.17 show that film thickness is slightly reduced but still in low values. The haze value is increased with increasing frequency. Since the separation is constant, increasing the frequency decreases the distance between consecutive laser pulses. A decrease in the distance between pulses means an increase in the pulse overlap

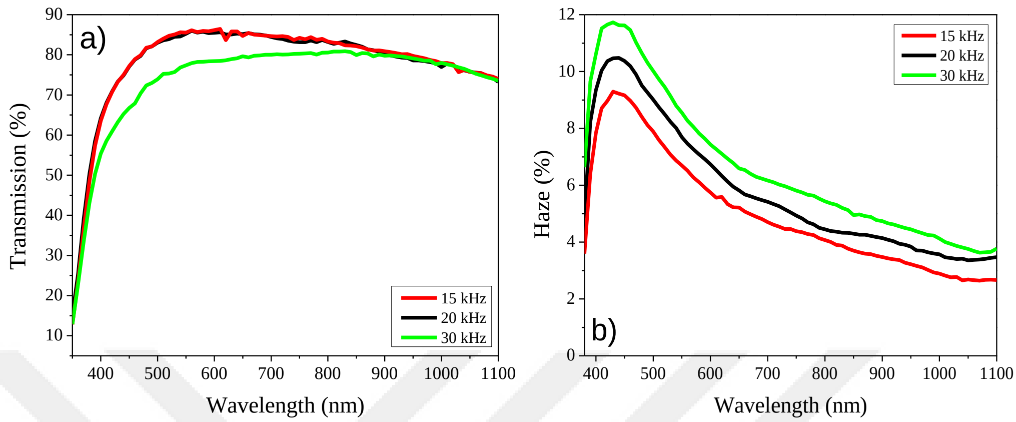

Figure 4.35 a) Transmission b) Haze value of frequency comparison set

Further study is done to analyze the diode current comparison with the best result obtained from the frequency study. Here 24-26A and 26-28A current results are represented in Table 4.18 and Figure 4.36. 30 kHz frequency is used with different diode current values.

Table 4.18 Comparison of diode current

	30 kHz, 600 mm/s, 30 μm separation	
Sheet Resistance	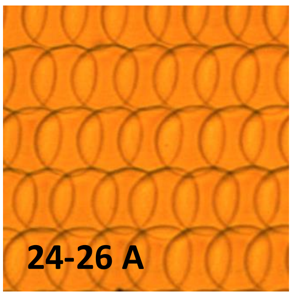	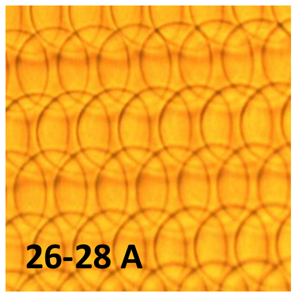
Before	3.5 Ω/□	3.6 Ω/□
After	5.6 Ω/□	5.4 Ω/□

Various parameters have been studied in t-DOE-3. As discussed before, deposition of AZO layer was produced on full-size flexible glass and cut into small pieces. More than one sample is used for laser application for repeatability. However, areas scanned with these values are not consistent in delamination. Thus current values lower than 24-26A are omitted.

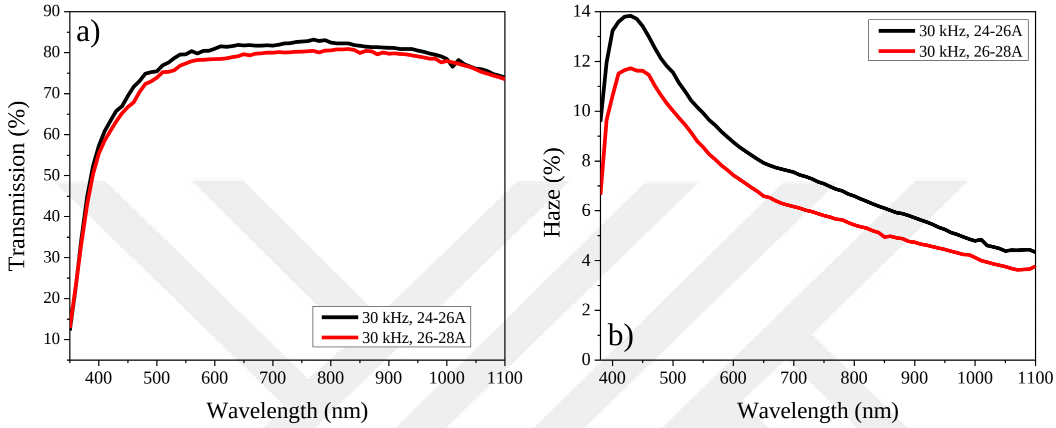

Figure 4.36 a) Transmission b) Haze value of power comparison set

The increase in current increases the overlapping of the laser pulses. In addition, an increase in current results in an increase in spot size. Since the feature size of the laser spots is already oversized for optimum light management, getting a more prominent spot is not desired. In other words, the growing laser spot flattens the surface instead of roughening it. As a result, in Figure 4.36 b), the haze value has dropped to lower values when the current increases. As seen in Figure 4.36 a), the transmission value is dropped slightly because a higher current value removes more material from the surface, as observed from the sheet resistance value.

The area examined for increasing the overlap, line spacing, reducing the scanning speed (motor step speed), and double scanning are given in Table 4.19.

Table 4.19 Comparison of line spacing

	50 kHz, 24-26A, 600 mm/s	
Sheet Resistance	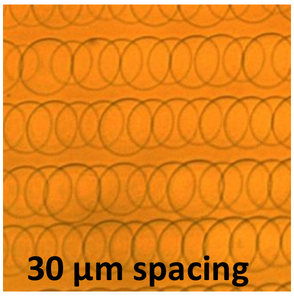	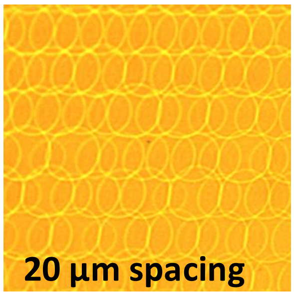
Before	3.5 Ω/□	3.6 Ω/□
After	4.2 Ω/□	4.5 Ω/□

The increasing frequency and line spacing introduce more laser spot overlap, resulting in more randomized texturing. Increasing line spacing increases the overlapping without changing feature size; thus, the haze value slightly increases, as seen in Figure 4.37 b).

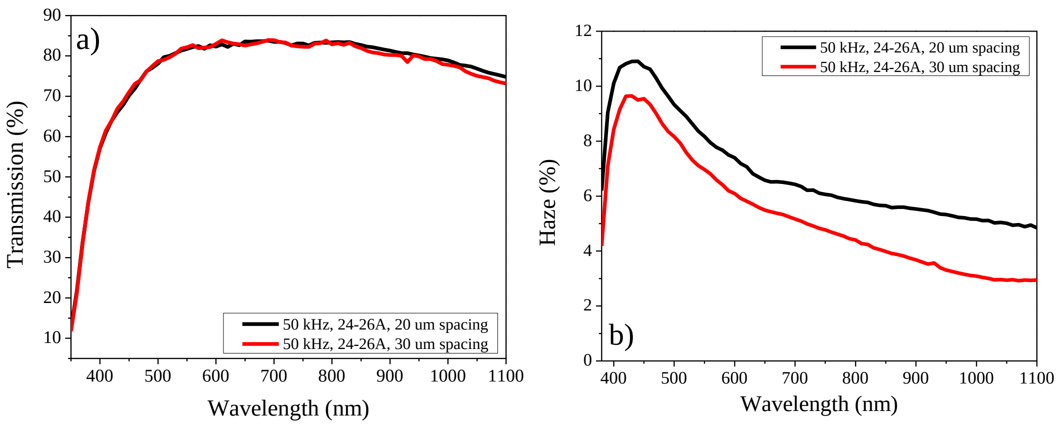

Figure 4.37 a) Transmission b) Haze value of line spacing comparison set

Table 4.20 Increasing overlapping by double scan

	15 kHz, 20-22A, 450 mm/s, 30 μm separation	
Sheet Resistance		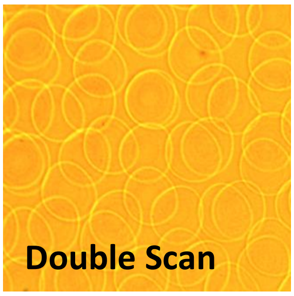
Before	3.5 Ω/□	3.5 Ω/□
After	4.2 Ω/□	4.6 Ω/□

Results show that the increase of high haze value can be achieved by introducing features having a different size to the layer. Up to now, it is obtained by the overlapping of the laser pulse. A laser pulse can overlap by multiple scanning. Results of dual scanning are given in Table 4.20 and Figure 4.38.

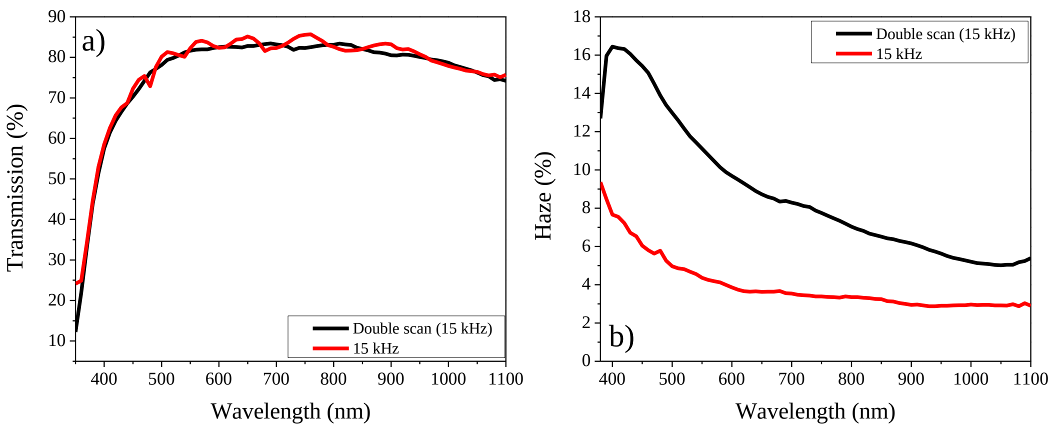

Figure 4.38 a) Transmission b) Haze value of double scan comparison set

The laser is focused on the surface of the samples for all of the laser parameters tested for t-DOE-3. A new experiment set is designed to test the focus position change in the t-DOE-4 study. Parameters for t-DOE-4 are given in Table 4.21. Focus position can be adjusted by either inserting different thickness values into the laser software or inserting defocus parameters at fixed thickness—either method results in the same way.

Table 4.21 Design of Experiments for Defocus Study (t-DOE-4)

Frequency	***Current***	***Motor S. Speed***	***Line Separation***	***Thickness***
30 kHz	24-26 A	600 mm/s	30 µm	1.1 mm
				3.1 mm
				4.1 mm
				5 mm

The laser system use the thickness value entered into the software to adjust the focus of the laser beam, which means the laser is focused on the surface by putting original (actual) thickness values. Results of the optical analysis are given in Figure 4.39. the laser should be defocused 1 mm to obtain higher haze values due to the focusing study. As a result of this study, it is seen that a high haze value is obtained at 3.1 mm. On the other hand, it can be concluded as the laser is not correctly aligned such that it is not focusing on the surface with absolute values.

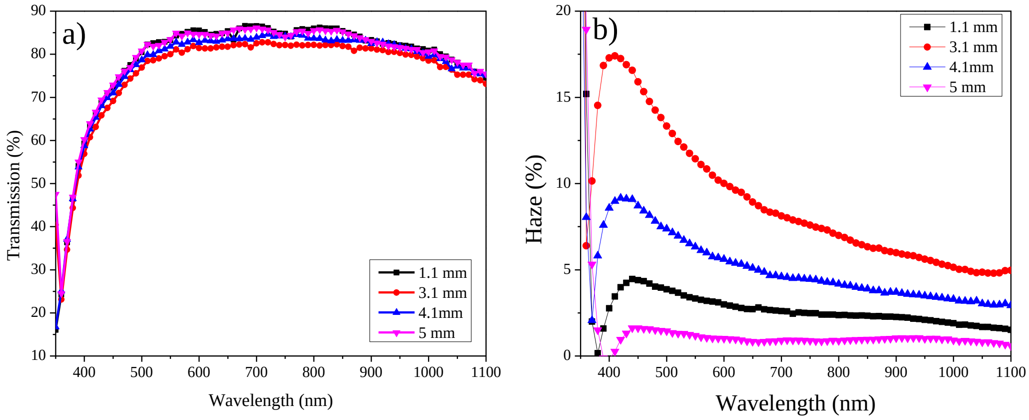

Figure 4.39 a) Transmission b) Haze value of DOE-4 (defocus study)

Having this information gathered from the DOE-3 and DOE-4, other laser texturing is studied to obtain a high haze value of front contact texturing for solar application. After obtaining the best parameters for two different frequencies, the subsequent study is to double scan an area with these parameters having different scan angles between them, and a comparison study is conducted. The detail of this study is tabulated in Table 4.22.

Table 4.22 Design of experiment for double Scan for surface texturing (DOE-5)

Scan Area #	***Tilt Angle***	***Line #***	***Frequency***	***Current***	***Scan Speed***	***Line Separation***
DS-1	45°	1st	15 kHz	20-22 A	600 mm/s	30 µm
		2nd	SAME PARAMETER			
DS-2	45°	1st	15 kHz	20-22 A	600 mm/s	30 µm
		2nd	30 kHz	20-22 A	600 mm/s	30 µm
DS-3	0°	1st	15 kHz	20-22 A	450 mm/s	30 µm
		2nd	SAME PARAMETER			
DS-4	45°	1st	15 kHz	20-22 A	450 mm/s	30 µm
		2nd	SAME PARAMETER			
DS-5	90°	1st	15 kHz	20-22 A	450 mm/s	30 µm
		2nd	SAME PARAMETER			
DS-6	90°	1st	15 kHz	20-22 A	450 mm/s	30 µm
		2nd	30 kHz	24-26 A	450 mm/s	30 µm
DS-7	45°	1st	30 kHz	20-22 A	600 mm/s	30 µm
		2nd	SAME PARAMETER			

Table 4.23 Surface analysis of double scan textures

DS-3	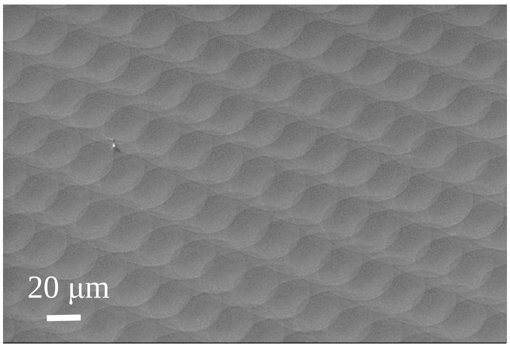
DS-5	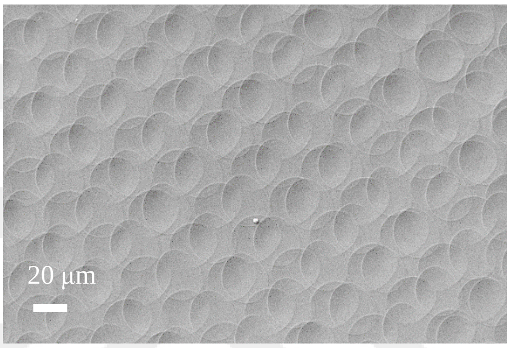
DS-6	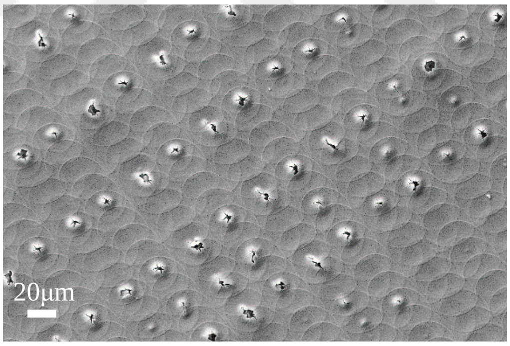
DS-7	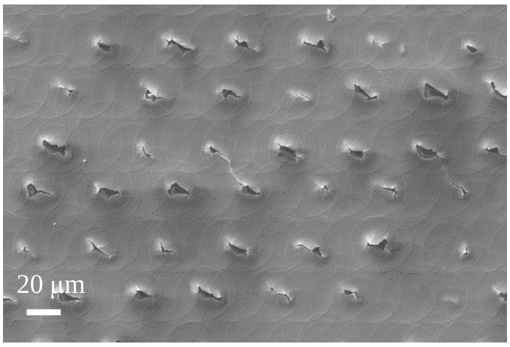

.

Surface analysis revealed deeper cracks on the surface resulting from the double scanning. However, there is no significant increase in sheet resistance, which means the crack does not go deeper so that it is separated and creates discontinuities through the film. After the laser process, ultrasonic cleaning can remove the residues. In addition, a thin layer of AZO can be deposited after texturing, as disgusted previously.

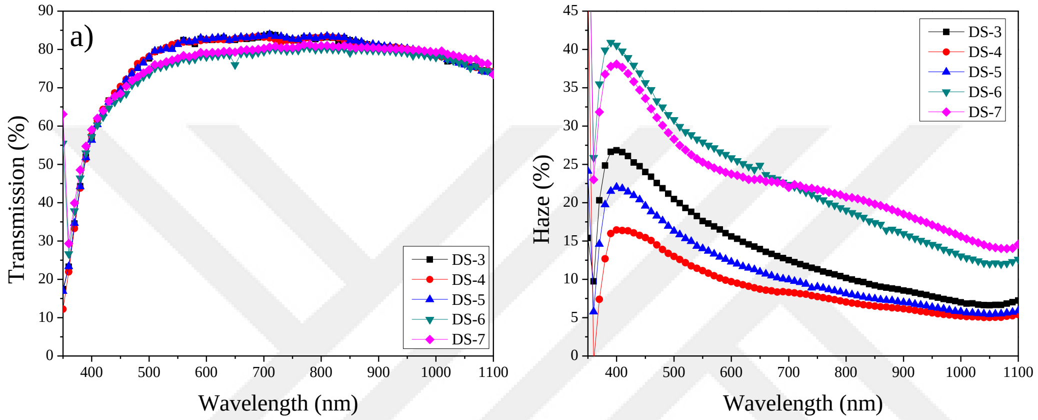

Figure 4.40 a) Transmission b) Haze value of DOE-5 (UV laser texture)

The haze value of 42% is obtained, as seen in Figure 4.40. The surface of these samples is further investigated via AFM and SEM. Results show that AFM analysis is not appropriate for such big features. Further analysis is done by SEM imaging and represented in Table 4.23.

4.2.2.4 Scribing Mode – Double scan study (t-DOE-6)

The new design of the experiment is studied on 1.2 micron thick AZO samples produced at the beginning of the t-DOE-3. In the previous laser texturing studies, it is concluded that dual scanning introduces more random texturing. Random textures create small and big features simultaneously, which results in higher haze values. New laser parameters with UV laser are studied accordingly. The details of this study are tabulated in Table 4.24.

Table 4.24 Design of experiment for double Scan for surface texturing (t-DOE-6)

Scan Area #	***Tilt Angle***	***Line #***	***Frequency***	***Current***	***Scan Speed***	***Line Separation***
UV1-1d	90°	1st	15 kHz	20-22 A	450 mm/s	30 µm
		2nd	30 kHz	24-26 A	450 mm/s	20 µm
UV1-2d	90°	1st	30 kHz	24-26 A	450 mm/s	20 µm
		2nd	SAME PARAMETER			
UV2-1d	0°	1st	30 kHz	24-26 A	600 mm/s	15 µm
		2nd	30 kHz	24-26 A	450 mm/s	15 µm
UV2-2d	45°	1st	30 kHz	24-26 A	450 mm/s	15 µm
		2nd	SAME PARAMETER			
UV3	45°	1st	15 kHz	20-22 A	450 mm/s	30 µm
		2nd	30 kHz	24-26 A	450 mm/s	20 µm
UV4-1	-	-	30 kHz	22-24 A	400 mm/s	20 µm
UV4-2	-	-	30 kHz	22-24 A	600 mm/s	30 µm
UV5-1	-	-	19 kHz	22-24 A	400 mm/s	31.5 µm
UV5-2	-	-	18 kHz	22-24 A	400 mm/s	33.5 µm
UV6-1			19 kHz	22-24 A	600 mm/s	31.5 µm
UV6-1			18 kHz	22-24 A	600 mm/s	33.5 µm

The samples are manually rotated by 90° after the first laser processing for the double laser processing. Single spots can be obtained along the scribe line by adjusting the laser repetition rate and motor stage speed parameters. Thus, horizontal periodicity can be obtained by adjusting the laser repetition rate and the motorized stage speed. After obtaining the best parameters for two different frequencies, the following study is to double scan an area with these parameters having different scan angles between them, and a comparison study is conducted.

After the surface analysis of r-DOE-6, the 1x3 cm2 area is scanned with selected laser parameters. In order to obtain a high haze value, each scanned area is optically investigated via SEM imaging. The double scan texture results reach haze values as high as 60%, given in Figure 4.41.

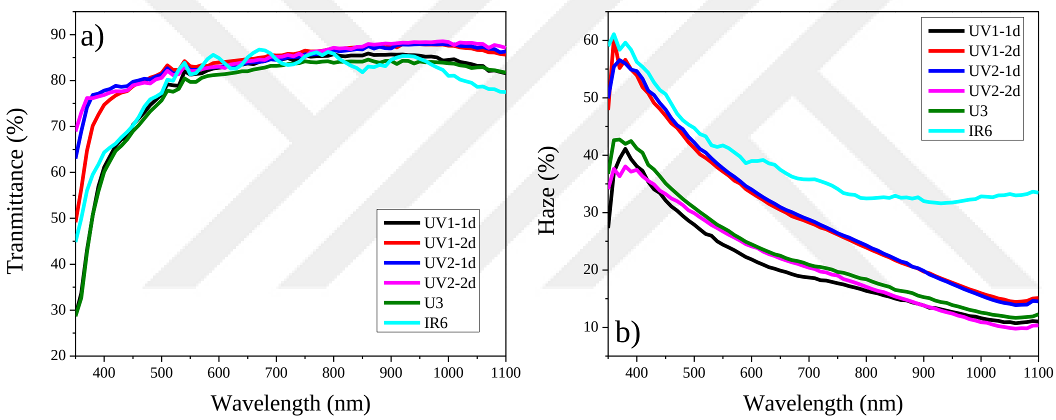

Figure 4.41 a) Transmittance b) Haze of double scan textures of DOE-6 (UV laser texture and one of the IR laser textures for comparison)

Surface analysis of best textures is given in Figure 4.42. Unlike the previous UV texture study, SEM images of sample UV1-2 given in Figure 4.42 a) show that the samples' surface is smooth and free of any flakes. Surface analysis is also carried out with AFM, and measurements are given in Figure 4.42 b). The surface of the films has a roughness of 84 nm. Roughness is in the order of nm; however, the texture size is in the order of microns; thus, the roughness values will not affect the film quality of the next layer deposited for solar cell application.

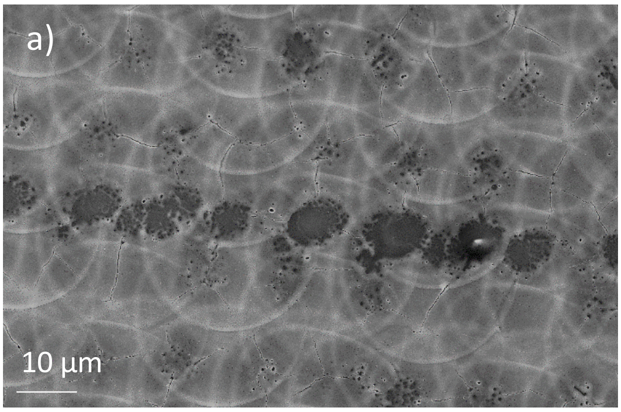

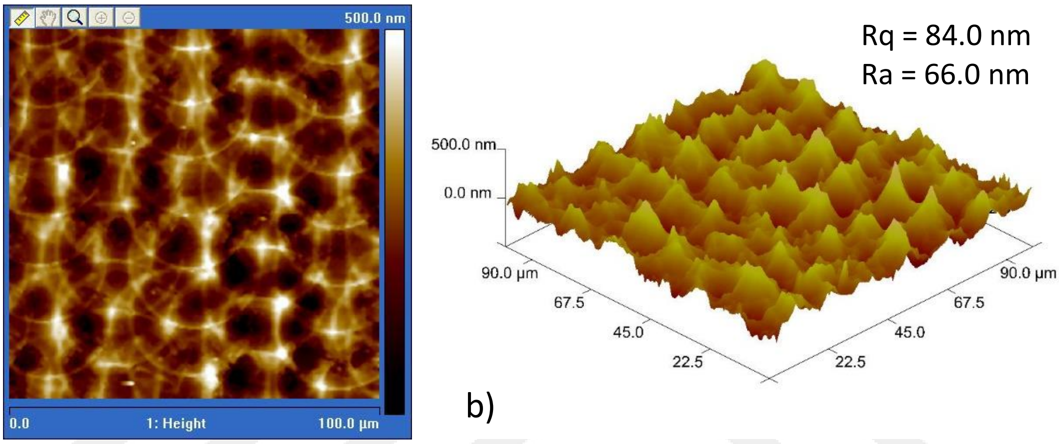

Figure 4.42 a) SEM image of the UV1-2 double scan texture b) AFM image of the UV1-2 double scan texture

In the case of IR texture, the laser is coming from the glass side. Meaning loos some of its energy inside the glass substrate and focus on the surface of the AZO layer. Because of this reason, after laser texturizing, there appear two different regions on the surface. Since the glass fabrication includes stretching glass from large pieces, there appear mutual waves on the surface; this is also called surface form error. The laser passes through these regions and diffuses inside the glass, which enhances/helps the texture. Surface texture results of IR texture are given in Figure 4.43.

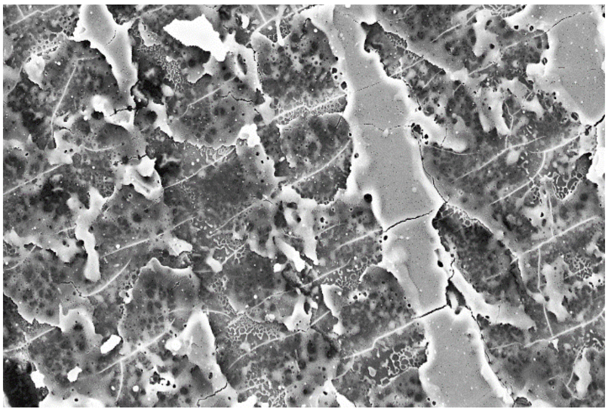

Figure 4.43 Surface of AZO layer after IR texturing

4.2.2.5 Scribing Mode – Double scan study (t-DOE-7)

Overlapping of laser pulses is examined after the direct laser writing process by the camera installed in the laser system. A matrix is designed for texturing after obtaining the best parameters at two different frequencies and two different motor stage speeds. The first parameter double scans an area with these parameters having different scan angles between them, and a comparison study is conducted. The details of this study are tabulated in Table 4.25 and Table 4.26.

Texturing and patterning of AZO-coated glass substrates studied in this thesis are produced by direct laser processing using two different wavelengths. AZO is deposited on 25 cm x 25 cm flexible ultra-thin glass (~100μm) using RF magnetron sputtering process of 2% AZO ceramic target. The process parameters such as the deposition temperature of 250°C, deposition time, Ar flow rate of 125 sccm, RF power of 600 watts, and deposition pressure of 3 mTorr are used to obtain a film thickness of 1.2 μm with the desired sheet resistance and film crystallinity [4].

Table 4.25 Design of experiment for double Scan for surface texturing at 532 nm

Scan Area #	***Tilt Angle***	***Line #***	***Frequency***	***Current***	***Scan Speed***	***Line Separation***
G3-area1	-	-	30 kHz	30-32 A	450 mm/s	10 µm
G3-area2	90°	1st	30 kHz	30-32 A	450 mm/s	10 µm
		2nd	30 kHz	31-33 A	450 mm/s	10 µm
G3-area3	90°	1st	15 kHz	28-30 A	450 mm/s	20 µm
		2nd	30 kHz	31-33 A	450 mm/s	10 µm
G3-area4	-	-	15 kHz	28-30 A	450 mm/s	20 µm
G4-area1	-	-	30 kHz	31-33 A	600 mm/s	15 µm
G4-area2	90°	1st	30 kHz	31-33 A	600 mm/s	15 µm
		2nd	30 kHz	31-33 A	450 mm/s	15 µm
G4-area3	-	-	30 kHz	31-33 A	450 mm/s	15 µm

Table 4.26 Design of experiment for double Scan for surface texturing at 1064 nm

Scan Area #	***Tilt Angle***	***Line #***	***Frequency***	***Current***	***Scan Speed***	***Line Separation***
IR1-area1	-	-	15 kHz	18-20 A	450 mm/s	15 µm
IR1-area2	-	-	30 kHz	19-21 A	450 mm/s	20 µm
IR1-area3	90°	1st	30 kHz	19-21 A	450 mm/s	20 µm
		2nd	SAME PARAMETER			
IR1-area4	90°	1st	15 kHz	18-20 A	450 mm/s	15 µm
		2nd	30 kHz	19-21 A	450 mm/s	20 µm
IR2-area1	-	-	30 kHz	18-20 A	450 mm/s	25 µm
IR2-area2	90°	1st	30 kHz	18-20 A	450 mm/s	25 µm
		2nd	SAME PARAMETER			

Surface analysis of the best green laser textures is given in Figure 4.44. Different than the previous UV texture study surface of the samples is defect-free. Surface analysis is also carried out with ZygoZegage optical profiler. The surface of the films has a roughness of 100 nm to 400 nm. Roughness is in orders of nm; however, the texture size is in the order of microns; thus, high roughness values will not affect the film quality of the next layer deposited for solar cell application.

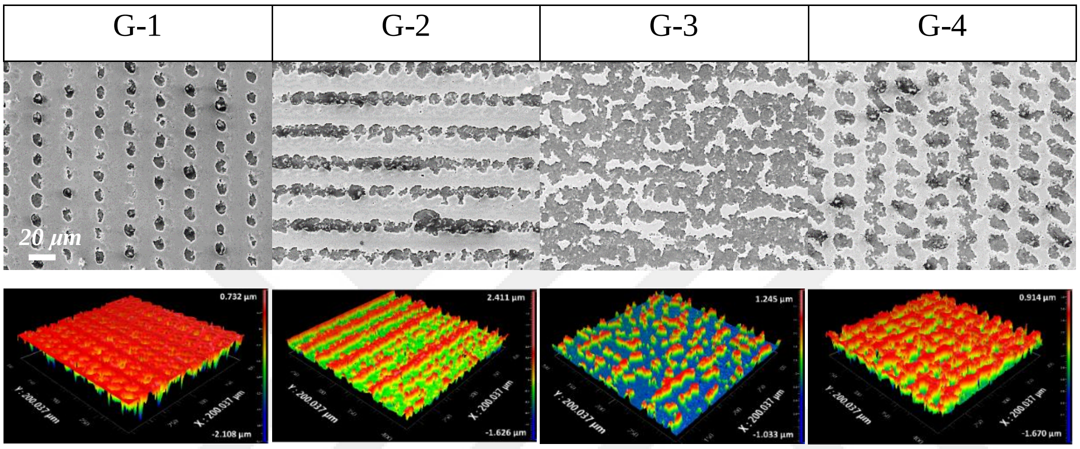

Figure 4.44 SEM and optical profiler image of the green-laser textured samples

AZO is a degenerated semiconductor with a direct bandgap ranging from 3.2 to 3.7 eV. In the case when a green-laser is utilized, the incident light energy is mainly absorbed by the AZO band electrons and is transferred to its lattice and heats it rather than effectively ablates the film and/or dramatically reduces its thickness since the green light energy (~2.3 eV) is much smaller than the bandgap of AZO.

Each scanned area is optically investigated to obtain a high haze value. Results of green-laser texture reach haze values as high as 64% are given in Figure 4.45. As seen in Figure 4.45, enhancement of transmission of the layers in the blue region of the spectrum is observed. In addition, apart from UV-laser texturing, green-laser texturing covers the entire spectrum.

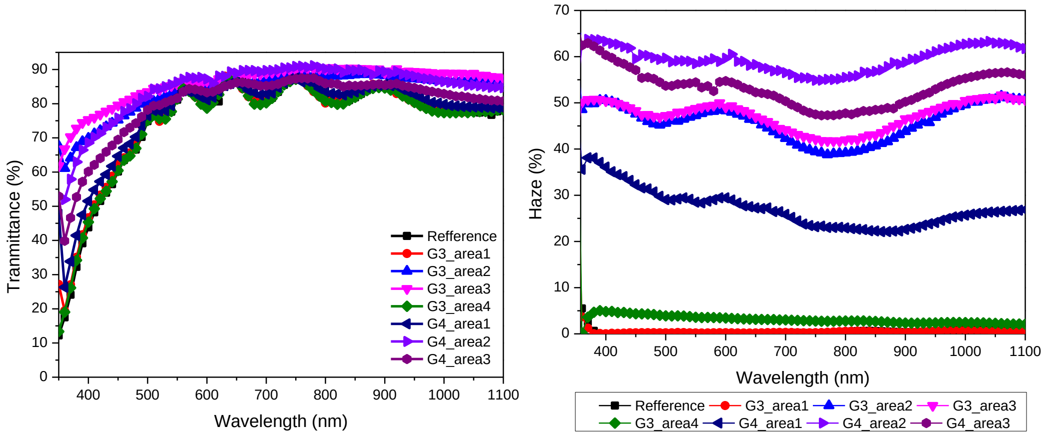

Figure 4.45 a) Transmittance b) Haze of the green-laser textured samples

Surface analysis of the best IR laser textures is given in Figure 4.46. Surface analysis is also carried out with ZygoZegage optical profiler. The surface of the films has a roughness less than 100 nm. Roughness is in orders of nm; however, the texture size is in the order of microns; thus, high roughness values will not affect the film quality of the next layer deposited for solar cell application.

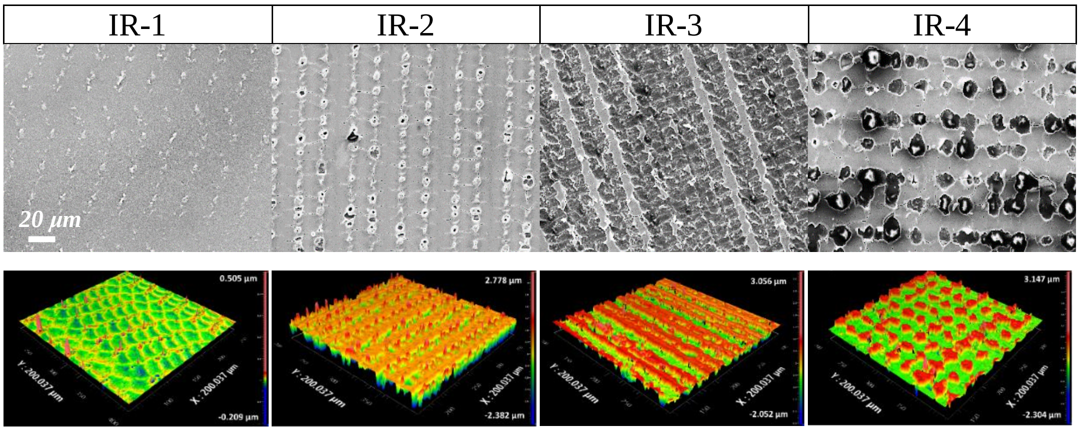

Figure 4.46 SEM and optical profiler image of the IR-laser textured samples

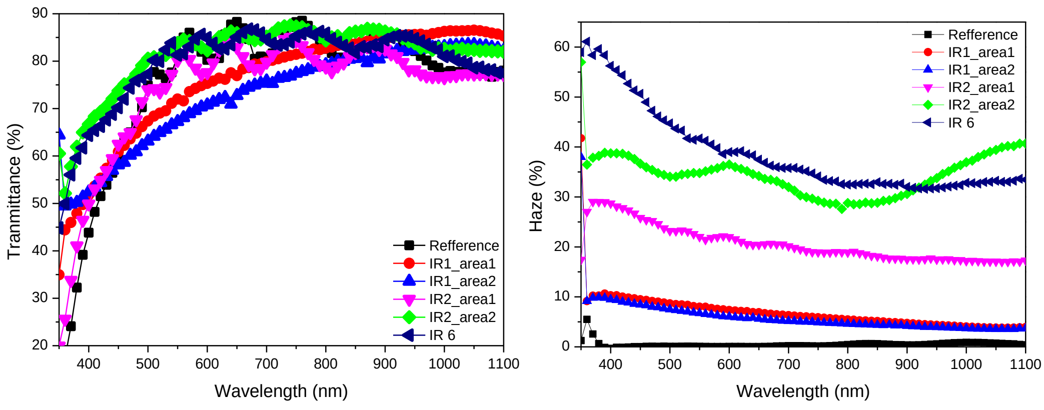

Figure 4.47 a) Transmittance b) Haze of IR-laser textured samples

With IR texture, it is hard to achieve defect free surface which means less parameters are available. Through optimizing the laser parameters, high conductive, high transmittance, and desirable high haze at 1064 nm laser wavelength was reached up the 60% in the visible region. Results of IR lser texture are given in Figure 4.47.

CHAPTER 5

AMORPHOUS SILICON THIN-FILM SOLAR CELLS ON FLEXIBLE SUBSTRATES

Single junction solar cells are produced onto ultra-thin flexible glass substrates in the superstrate configuration. In this study, p-i-n type single-junction solar cells are also produced on the laser textured aluminum-doped zinc oxide (AZO) layers. This chapter shows the results of amorphous silicon thin film solar cell production on ultra-thin flexible substrates.

The following sections present the results of single-junction p-i-n type amorphous silicon thin film solar cells. First, a preliminary deposition of p-i-n type amorphous silicon is presented as a reference sample before optimizing each layer. Then, solar cell results produced with optimized layers are given. Second, the solar cells produced on the textured TCO layer are presented. Finally, the results of thin film production of flexible modules connected in series via direct laser writing are given.

5.1 Device Structure of Reference Sample

Here in this section, three different p-i-n depositions are conducted. In each deposition, the most straightforward cell structure is used with layers of AZO / p-a-Si:H / i-a-Si:H / n-a-Si:H / Ag in superstrate cell configuration. All the thin film solar cells represented in this chapter used the given configuration. The thin film a-Si:H solar cell structure can be seen in the schematic representation shown in Figure 5.1.

First, light passes through the transparent plastic substrate. Then passes through the transparent conductive oxide (TCO) layer. This layer is also used as front contact. Aluminum doped zinc oxide (ZnO:Al) is one of the suitable materials for the TCO layer with the advantage of good adhesion and a comparable refractive index with silicon. After the TCO layer, light reaches the silicon layer, denoted as the active photovoltaic (PV) area

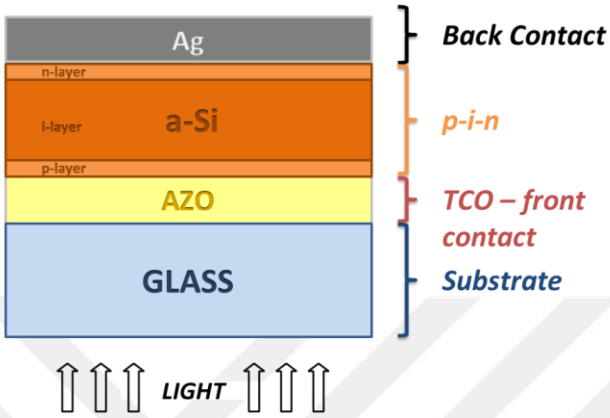

Figure 5.1 Layer by layer p-i-n type device structure

The active PV area in the structure consists of three main layers. Intrinsic silicon material is placed between two doped layers. When the light is reached this layer stack, it is absorbed, and electron-hole pairs are created in the intrinsic layer. An intrinsic layer between the two doped layers is needed for silicon-based thin film solar cells since the defect density of the amorphous silicon layer is too high for doped layers. The created minority carriers have a very short lifetime in defective layers. In order to collect these carriers, p-i-n type structure is used. After the silicon layers, light is reflected from the back reflector. The critical role of this layer is to collect charge carriers from the system [13].

The solar cells are characterized electrically, as discussed in Chapter 2. The key performance parameters (FF, V_{OC}, J_{SC}, η) are deduced from the I-V measurements. The theoretical limit of J_{SC} for a p-i-n type single-junction solar cell having a 1.75 eV optical band gap intrinsic layer is 21 mA/cm^2. The theoretical limit of V_{OC} is 1.3 V for the same conditions.

5.1.1 Thin Film Silicon Solar Cell on Ultra-thin Flexible Glass Substrates

5.1.1.1 Preliminary Studies on Thin Film Silicon Solar Cells

A single-junction solar cell is deposited by plasma-enhanced chemical vapor (PECVD) on various glass substrates. A 2x2 mm^2 contact mask is used when evaporating the back contact (silver). Superstrate cell configuration is used as the device structure. 1 µm thick AZO deposited on both thick (1.1mm) and ultra-thin (<100 µm) glass. A comparison study is conducted.

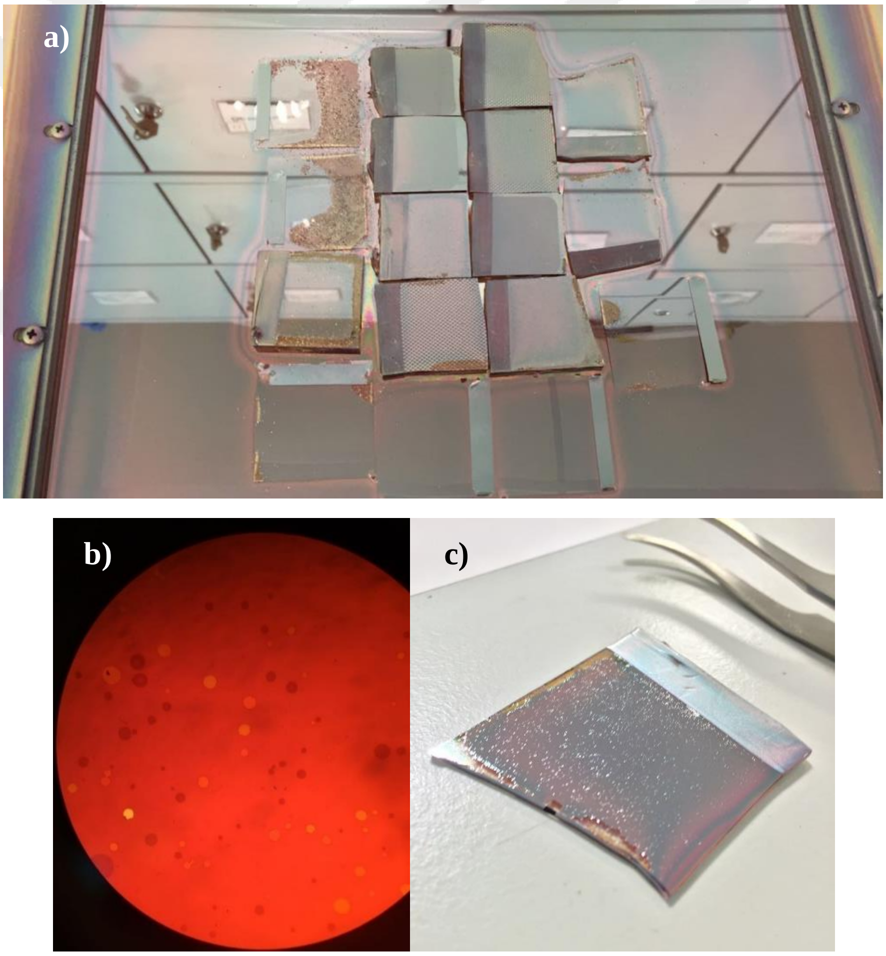

Figure 5.2 Process problems after p-i-n deposition a) delamination after deposition b) microscope image showing pinholes c) sample surface having both problems

Processes are not reproducible, films were delaminating after each process, and there were lots of pinholes in the films, see Figure 5.2. Pinholes are mainly observed after p-type a-Si deposition. During the investigation of this study, it is realized that doping gases decompose sufficiently for their concentration to fall out of tolerance value. As a result of this concept, sufficient doping can not be obtained. After this study, diborane is replaced with a new one.

As a result of the solar cell fabricated on ultra-thin and thick standard glass, photo-production increases as the ultra-thin flex glass blocks less light, resulting in a slightly higher current density. This study compares the productions on different substrates. I-V is given in Figure 5.3, and essential values are summarized in Table 5.1.

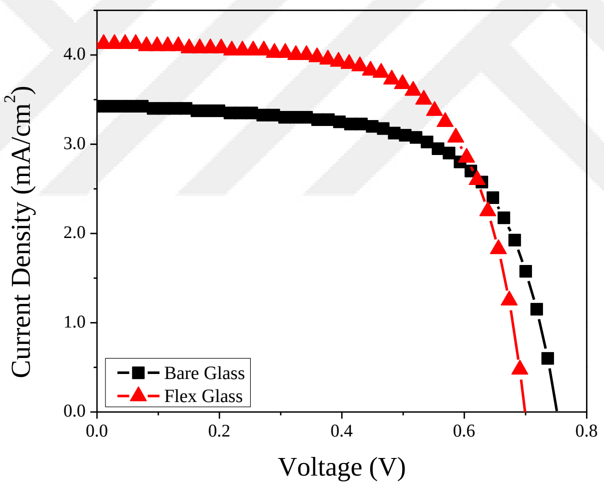

Figure 5.3 I-V characteristics of preliminary production

Table 5.1 Preliminary p-i-n device deposition parameters

	Voc (V)	*Jsc (mA/cm^2)*	*Efficiency (%)*	*Fill Factor (%)*
Bare Glass	0.751	3.43	1.85	64.56
Flex Glass	0.699	4.12	2.08	65.01

5.1.1.2 Thin Film Silicon Solar Cells with optimized layers: TYPE-1

The solar cell is obtained with the best parameters resulting from each layer's optimization. Parameters used in the device production are given in Table 5.2. Deposition temperature, power, and pressure are fixed for all layers as 175°C, 50 W, and 1 Torr. Simplest cell structure is used in this process with thickness of AZO 600 nm / p-a-Si:H (12 nm) / i-a-Si:H (250 nm) / n-a-Si:H (17 nm) / Ag 300 nm. AZO was used as as-deposited. Metal contact of the cells is thermally evaporated.

The solar cell deposited with the given parameters is denoted as a "TYPE-1" thin film silicon solar cell.

Table 5.2 Deposition parameters used in the TYPE-1 p-i-n

Parameters	p-layer	i-layer	n-layer
Deposition Power	50 W		
Deposition Pressure	1 mTorr		
Temperature	175°C		
$R=[H_2]/[SiH_4]$	18	9	18
$D=[Dopant]/[SiH_4]$	0.055	-	0.015

The sample is shown in Figure 5.4 a). The I-V curve of this sample is measured from each square contact point. Since no pinholes are detected in this run, all the contacts are adequately working. Only one contact was not working, and that was the one scratch placing the sample for measurement. The average and the best cell performance parameters are summarized in Table 5.3.

A counter color map is plotted in Figure 5.4 b) to visualize the efficiency map of the sample. The blue color indicates the low cell efficiencies at the bottom of the 2 x 2 cm^2 area. Higher efficiencies are obtained from top and side contacts of the 2 x 2 cm^2 square area. These variations in observed efficiencies correlate with the sample's banding resulting from deposition stress.

a) 

b) 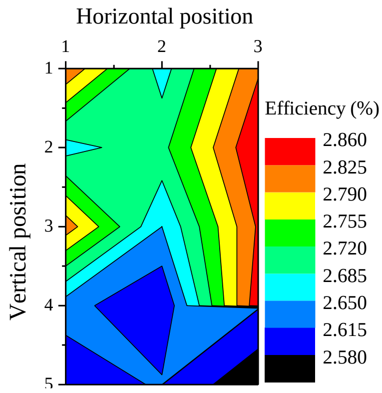

Figure 5.4 a) Sample image of TYPE-1 deposition b) Efficiency mapping of the sample

Table 5.3 Best performance results of TYPE-1 p-i-n solar cell

	Voc (V)	***Jsc (mA/cm^2)***	***Efficiency (%)***	***Fill Factor (%)***
Best TYPE-1	0.724	6.88	2.88	56.77
Average	0.708	6.84	2.75	55.66

After measuring the I-V of the sample, the sample is annealed to see the annealing effect on the sample. The sample is annealed at 150°C under N_2 flow for 20 minutes. After annealing, the V_{oc} value is increased. This increase in open-circuit voltage can be explained by the decrease in resistance of the back contact. In addition to that, the series resistance is reduced due to annealing the contact of the solar cell.

From this point on, all samples are annealed after p-i-n deposition. The I-V results given in Figure 5.5 are the results of the annealed samples. Annealing is essential in our device structure since another AZO cannot be deposited without shorting between back contact and n-layer.

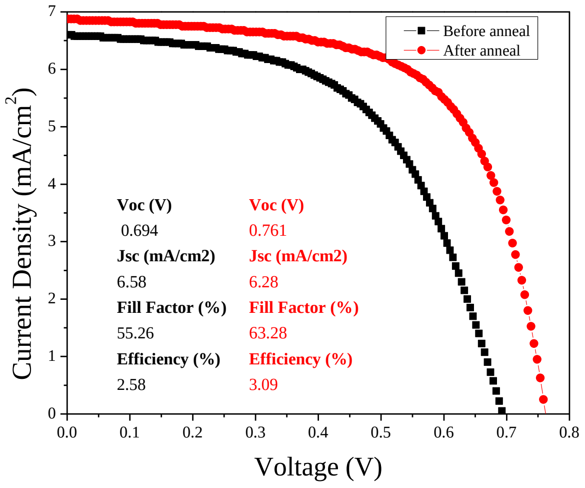

Figure 5.5 I-V characteristics of TYPE-1 production

5.1.1.3 Thin Film Silicon Solar Cells with optimized layers: TYPE-2

Parameters used in the device production are given in Table 5.4. In this run, the deposition power of the intrinsic layer is reduced to 30 W. Deposition temperature, power, and pressure are the same for doped layers, respectively, at 175°C, 50 W, and 1 Torr. Metal contact of the cells is thermally evaporated.

AZO 600 nm / p-a-Si:H (12 nm) / i-a-Si:H (250 nm) / n-a-Si:H (17 nm) / Ag 300 nm.

Table 5.4 Deposition parameters used in the TYPE-2 p-i-n

Parameters	p-layer	i-layer	n-layer
Deposition Power	50 W	30 W	50 W
Deposition Pressure	1 mTorr		
Temperature	175°C		
$R=[H_2]/[SiH_4]$	18	9	18
$D=[Dopant]/[SiH_4]$	0.055	-	0.015

The sample of TYPE-2 is shown in Figure 5.6 a). Results are given after the annealing of the sample. The best I-V curve obtained from this deposition is plotted in Figure 5.6 b). Table 5.5 summarizes this deposition's average and best cell performance parameters.

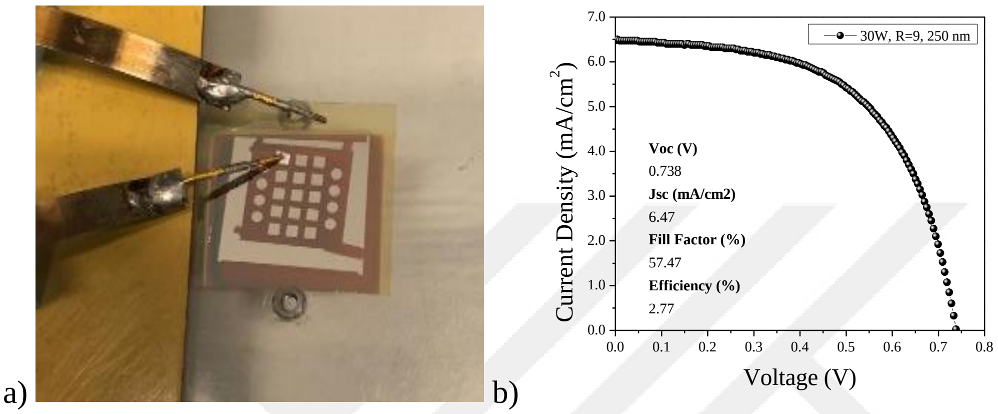

Figure 5.6 a) Image of the deposited sample b) I-V characteristics of TYPE-2 production

Table 5.5 Results of TYPE-2 p-i-n solar cell

	Voc (V)	*Jsc (mA/cm^2)*	*Efficiency (%)*	*Fill Factor (%)*
Best TYPE-2	0.738	6.47	2.77	57.47
Average	0.721	6.33	2.53	54.43

5.1.1.4 Thin Film Silicon Solar Cells with optimized layers: TYPE-3

The solar cell represented here is obtained with the best parameters resulting from each layer's optimization. Parameters used in the device production are given in Table 5.6. In addition to the change of deposition power, the ratio R is increased to 14. Deposition temperature, power, and pressure are the same for doped layers, respectively, at 175°C, 50 W, and 1 Torr. Metal contact of the cells is thermally evaporated and is annealed after metal contact evaporation. The best I-V curve obtained from this deposition is plotted in Figure 5.7.

AZO 600 nm / p-a-Si:H (12 nm) / i-a-Si:H (250) / n-a-Si:H (17 nm) / Ag 300 nm.

Table 5.6 Deposition parameters used in the TYPE-3 p-i-n

Parameters	p-layer	i-layer	n-layer
Deposition Power	50 W	30 W	50 W
Deposition Pressure	1 mTorr		
Temperature	175°C		
$R=[H_2]/[SiH_4]$	18	14	18
$D=[Dopant]/[SiH_4]$	0.055	-	0.015

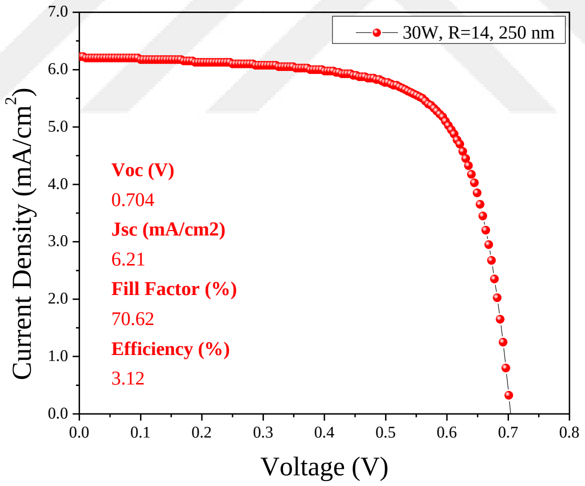

Figure 5.7 I-V characteristics of TYPE-3 production

5.1.1.5 Thin Film Silicon Solar Cells with optimized layers: TYPE-4

The solar cell represented here is to compare different i-layer thicknesses in terms of the performance parameter of the solar cell. Process parameters used in the device production are the same as in Table 5.6. Metal contact of the cells is thermally evaporated and is annealed after metal contact evaporation. The best I-V curve obtained from this deposition is plotted in Figure 5.8.

AZO 600 nm / p-a-Si:H (12 nm) / i-a-Si:H (300 nm) / n-a-Si:H (17 nm) / Ag 300 nm.

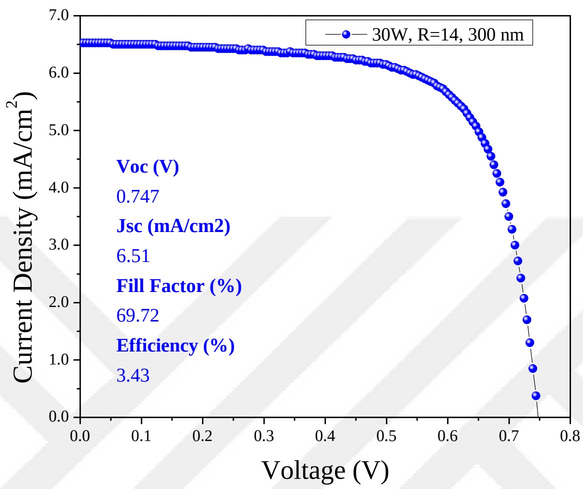

Figure 5.8 I-V characteristics of TYPE-4 production

5.1.1.6 Comparison of Different Types of Thin Film Silicon Solar Cells

In each p-i-n production, doped layers are deposited with the same deposition parameter at 175°C deposition temperature, 50 W power, and 1 Torr pressure. The difference between each type of p-i-n production is in the intrinsic layer, and all the varying deposition parameters are summarized in Table 5.7. The solar cell represented here is obtained with the best parameters resulting from each layer's optimization.

Table 5.7 Deposition parameters of each type of p-i-n solar cells

	TYPE-1	**TYPE-2**	**TYPE-3**	**TYPE-4**
Deposition Power	50 W	30 W	30 W	30 W
R=[H_2]/[SiH_4]	9	9	14	14
i-layer thickness	250 nm	250 nm	250 nm	300 nm

50 W power deposition is done to compare the process parameters with the old i-chamber. Even if the results of TYPE-1 deposition are high, the deposition at 50 W power in the new i-chamber is not stable. As discussed in Chapter 3, deposition at these conditions results in delamination, which is not consistent and reproducible. TYPE-2 and TYPE-3 show that the intrinsic layer becomes well-ordered as expected due to the hydrogen to silane ratio increase. When comparing TYPE-3 and TYPE-4, the increased intrinsic layer increases open-circuit voltage (V_{oc}). An increase in V_{oc} can be explained by the increase in thickness which means that the deposited layer reaches the microcrystalline regime. In addition, an increase in short circuit current means more absorption due to increased layer thickness. Annealing also improves this condition as well.

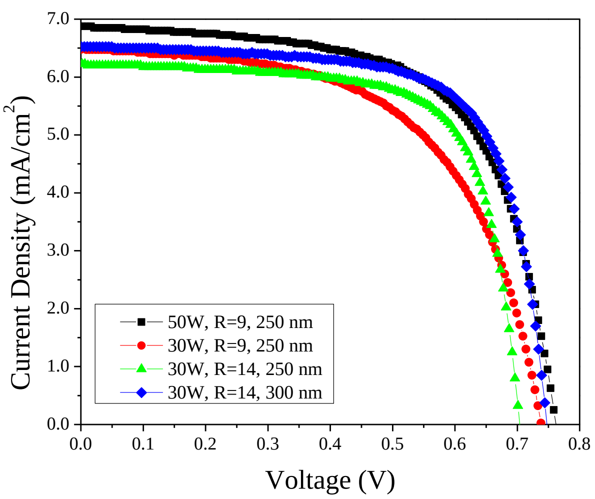

Figure 5.9 I-V characteristics of four different types of solar cells deposited in GünEr

The best parameters of 3.43% efficiency, 0.741 V open-circuit voltage, 6.51 short-circuit current density, and 69.72 fill factor is obtained.

Table 5.8 Results of different types of p-i-n solar cell

	Voc (V)	*Jsc (mA/cm^2)*	*Efficiency (%)*	*Fill Factor (%)*
TYPE-1	0.761	6.28	3.09	63.29
TYPE-2	0.738	6.47	2.77	57.47
TYPE-3	0.704	6.21	3.12	70.62
TYPE-4	0.747	6.51	3.43	69.72

5.2 Device Structure of laser textured AZO samples

Light management in the first layer of the device enhances the light absorption of a thin film solar cell. The first layer, the transparent conductive oxide layer, is textured, or the substrate can be textured. Texturing helps to reduce scattering and enhance light entering the absorber layer. Parameters such as texture size and periodicity are essential features for texturing.

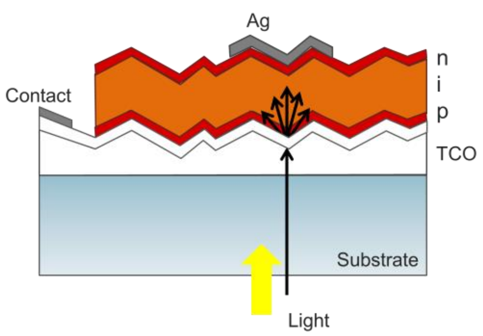

Figure 5.10 Schematic representation of amorphous silicon solar cell in superstrate configuration

The focus of this study is to compare the surface texturing of AZO thin films deposited on ultra-thin flexible glass substrates by RF magnetron sputtering for thin film photovoltaic applications obtained with different laser parameters operating at infrared, green, and ultraviolet. Laser textured samples studied earlier are used as the substrate for p-i-n type single junction thin film silicon solar cells. Metal contact of the cells is thermally evaporated directly onto the n-layer. A schematic representation of amorphous silicon solar cell superstrate configuration is seen in Figure 5.10. Device structure with layer thickness is; laser texture AZO (1200 nm) / AZO (100 nm) / p-a-Si:H (12 nm) / i-a-Si:H (250 nm) / n-a-Si:H (17 nm) / Ag 300 nm. Parameters used in the deposition are given in Table 5.9.

Table 5.9 p-i-n parameters used in the deposition of textured samples

Parameters	p-layer	i-layer	n-layer
Deposition Power	50 W	30 W	50 W
Deposition Pressure	1 mTorr		
Temperature	175°C		
$R=[H_2]/[SiH_4]$	18	9	18
$D=[Dopant]/[SiH_4]$	0.055	-	0.015

5.2.1 Results of Thin Film Silicon Solar Cell on Laser Textured AZO

Different textured samples processed with three different laser wavelengths are presented in Figure 5.11. Samples used in this study are laser textured samples discussed in Chapter 4. In order to overcome the degradation of the AZO layer and improve the conductivity, 100 nm AZO was deposited onto AZO textured samples

IR1_c1	G3_c2	UV4_c3

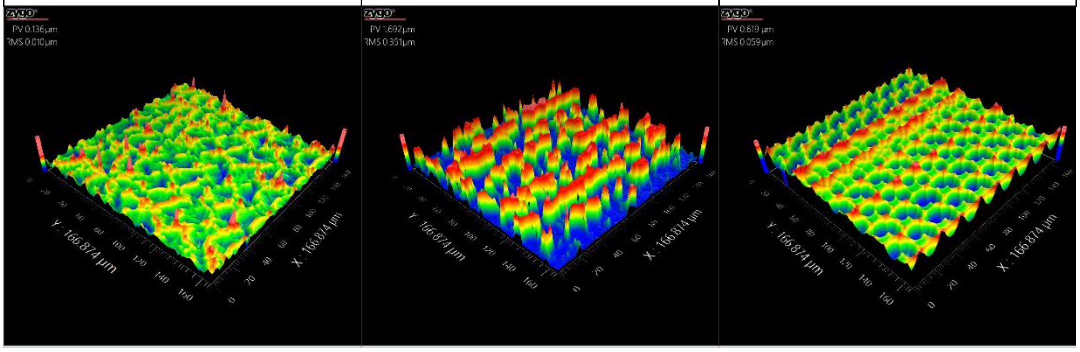

P-V: 0.136 µm	P-V: 1.7 µm	P-V: 0.619 µm
RMS: 10 nm	RMS: 351 nm	RMS: 59 nm

Figure 5.11 Optical profiler image of the UV, green, and IR laser textured TCO samples that are used for solar cell application

Laser textured samples studied earlier are used as the substrate for p-i-n type single junction thin film silicon solar cells. Most textured samples having high P-V values do not work due to shorting. The green laser textured sample given in Figure 5.11 is worked. This sample contains a large island that has extensive surface coverage.

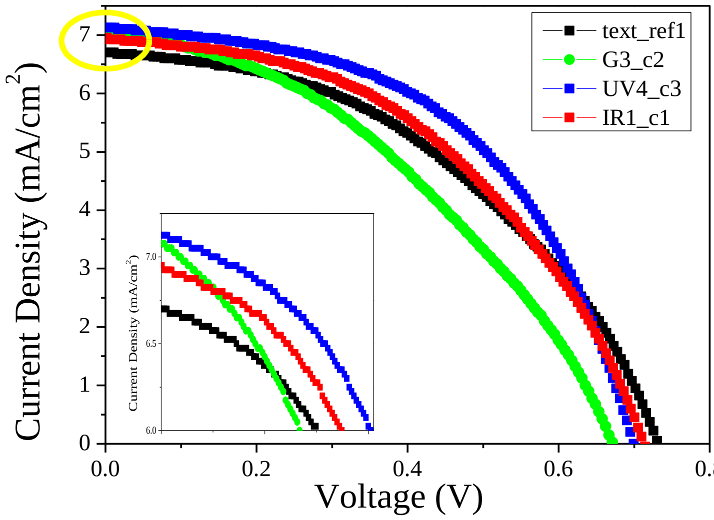

Figure 5.12 Solar cell results of textured samples of UV, green, and IR laser textured TCO samples (inset shows J_{sc} values in detail)

From the I-V results of these samples given in Figure 5.12, it can be seen that an increase in short circuit current (I_{sc}) is observed where a slight decrease in open-circuit voltage (V_{oc}). A slight decrease in V_{oc} is observed and can be explained by the resistance resulting from texture. A decrease in V_{oc} can be explained by the resistance resulting from texture. 3.35 % for IR, 5.59 % for green, and 5.22 % for UV increase in I_{sc} are observed due to AZO texturing.

Table 5.10 Summary of best results of textured p-i-n solar cells

	Efficiency (%)	*Voc (V)*	*Jsc (mA/cm^2)*	*Fill Factor (%)*
IR texture	2.29	0.713	6.93	46.07
Green texture	1.88	0.671	7.04	39.47
UV texture	2.57	0.699	7.06	51.47
Reference	2.20	0.731	6.67	44.60

5.3 Monolithically series-connected flexible device

Large-area thin film modules are made using laser processes. Successive cells can be separated from each other using precision laser scribing. Laser processing separates the cells and ensures they are connected in series by applying it between the solar cell production steps. The schematic diagram shows the monolithic series connection of cells in Figure 5.13. Contrary to the crystalline solar cell technologies, laser scribing technology gives us the flexibility to arrange the size of each cell and their connections with each other during cell production [70].

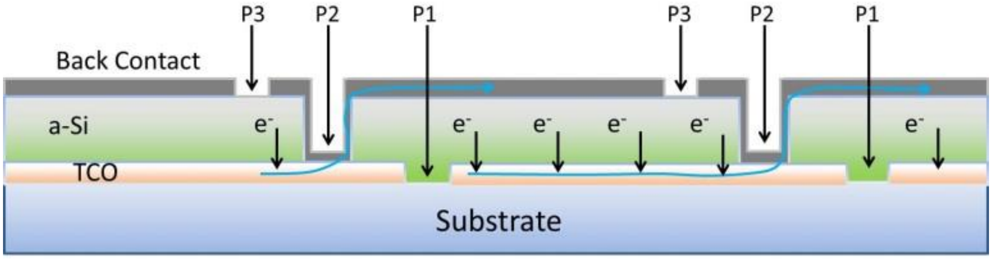

Figure 5.13 Thin film silicon solar cell module cross-section shows monolithic connection scribes

The module is obtained by three main scribe lines called P1, P2, and P3, shown in Figure 5.14. Each laser process takes place during cell production. P1 removes the transparent conductive oxide (TCO) layer, which provides electrical isolation of each cell. Scribing of P1 is mainly done by laser with a wavelength in the range of infrared (1064 nm). Ultra-violet (355 nm) laser is also used for P1 scribing. The wavelength used in the P1 scribing process can be selected according to the TCO material used in the solar cell. After P1 scribing is done, the p-i-n structure is deposited. P2 removes the silicon layer up to the TCO layer, which provides an electrically series connection between cells. P2 scribe is done by a green laser (532 nm). Back contact is deposited after the P2 scribing process. P3 is the removal of the back contact, which provides the series connection of each cell. In addition to these scribes, a fourth scribe isolates the whole structure to form the resulting module [71].

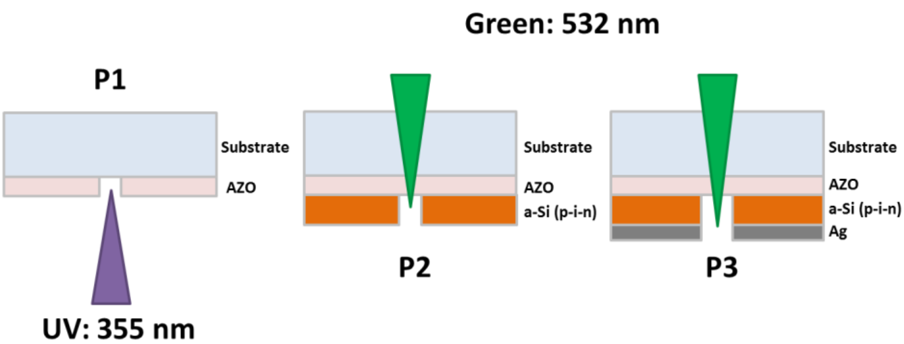

Figure 5.14 Laser Scribing Stages

After layer characterization of thin films for silicon solar cells is completed, a-Si:H thin film module will be studied. The thin film module is obtained by monolithic series connection via laser processes. In order to obtain an electrical connection between each cell, layers are cut via laser, and then the next layer is deposited on top.

5.3.1 Laser scribing of P1

Preliminary P1 scribing study using an IR (1064 nm wavelength) laser are studied on 600 nm AZO deposited on standard 2 mm glass substrates. Laser scribe lines can be seen in Figure 5.15.

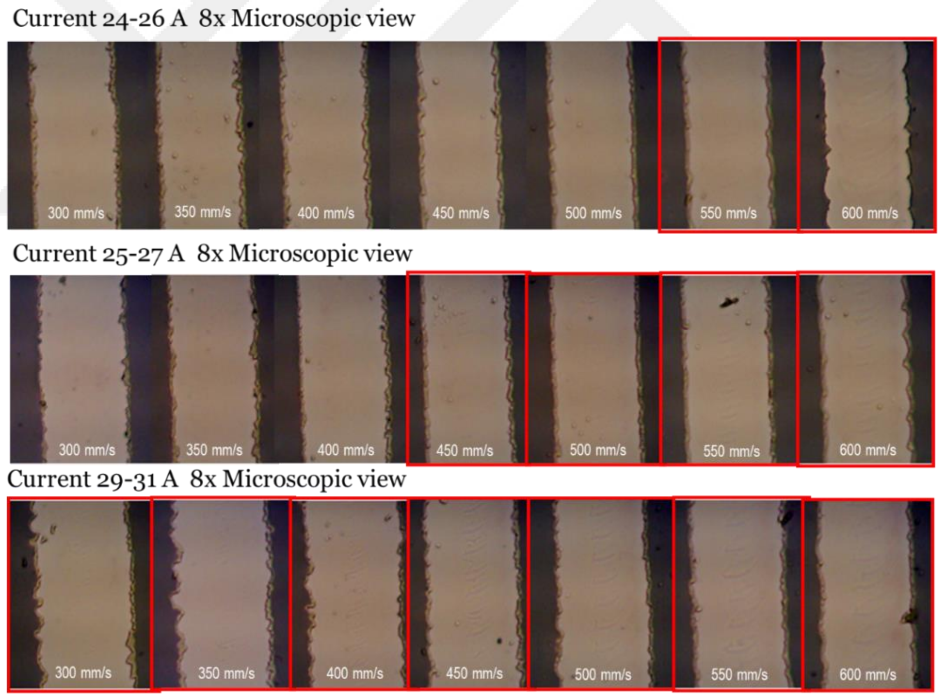

Figure 5.15 P1 scribes at 50 kHz with IR laser

At constant frequency, it is observed that increasing current (increasing laser power) and increasing motor stage speed damage the glass underneath. Other experiments are designed accordingly.

P1 scribing is studied using a UV (355nm wavelength) laser. 1 µm AZO deposited flexible glass substrates are studied.

The design of the experiment (DOE) is prepared according to the AZO texturing study, and process parameters are tabulated in Table 5.11 and Table 5.12. Frequency and the current values are increased to have complete layer removal.

Table 5.11 DOE for 30 kHz frequency (ls-DOE-1)

	Frequency	***Current***	***M. Speed***
1	30 kHz	34-36 A	600 mm/s
2	30 kHz	36-38 A	600 mm/s
3	30 kHz	34-36 A	300 mm/s

Table 5.12 DOE for 50 kHz frequency (ls-DOE-2)

	Frequency	***Current***	***M. Speed***
4	50 kHz	34-36 A	600 mm/s
5	50 kHz	36-38 A	600 mm/s
6	50 kHz	36-38 A	300 mm/s
7	50 kHz	34-36 A	300 mm/s

Optimization of any of the scribe is related to the film thickness. The essential point of this process is the total TCO removal. The simplest and most effective way to test total removal is to look at the electrical connection of the two separated pieces with a multi-meter. Further characterization of the scribe line is done by analyzing optical microscope images.

Samples used here are 1 µm thick AZO-coated ultra-thin flexible glass substrates. A UV laser operating at 355 nm irradiates from the film side. Laser scribing lines are investigated by optical microscope imaging, and results are given in Table 5.13 and

Table 5.14. Electrical disconnection of each laser line is also checked via multi-meter.

Table 5.13 Optical microscope images of DOE for 30 kHz frequency

Frequency	Current	M. Speed	Reflection Image	Transmission Image
30 kHz	34-36 A	600 mm/s	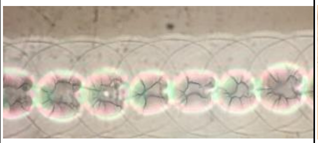	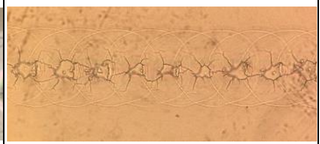
30 kHz	36-38 A	600 mm/s	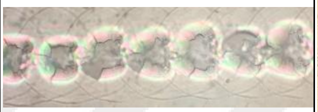	
30 kHz	34-36 A	300 mm/s	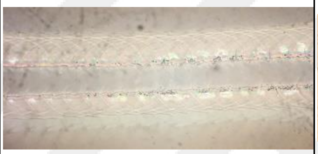	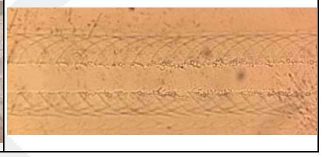

Table 5.14 Optical microscope images of DOE for 50 kHz frequency

Frequency	Current	M. Speed	Reflection Image	Transmission Image
50 kHz	34-36 A	600 mm/s	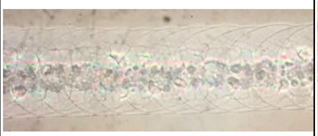	
50 kHz	36-38 A	600 mm/s		
50 kHz	36-38 A	300 mm/s		
50 kHz	34-36 A	300 mm/s		

UV irradiation is absorbed by both the Aluminum doped zinc oxide layer and glass substrate. As a result of that, films are illuminated from the film side. However, the Gaussian nature of the laser beam results in high energy in the center and relatively lower energy at the edge of the laser spot.

Microscope images reveal a region around the centerline that is the thermal effect caused by the laser during ablation. When the motor stage speed is increased thermal effect reduces; however, the scribe line width broadens. The width of each scribe line defines the dead regions between cells in a module.

5.3.2 Laser scribing of P2

P2 scribing is done via a green (532 nm) laser process. At low powers, more debris is observed. The performance parameters of this scribe are to obtain a narrow and clean cut. The line width of the scribe defines the death zone of the connected cells—the cleanness of the scribe results in excellent electrical isolation.

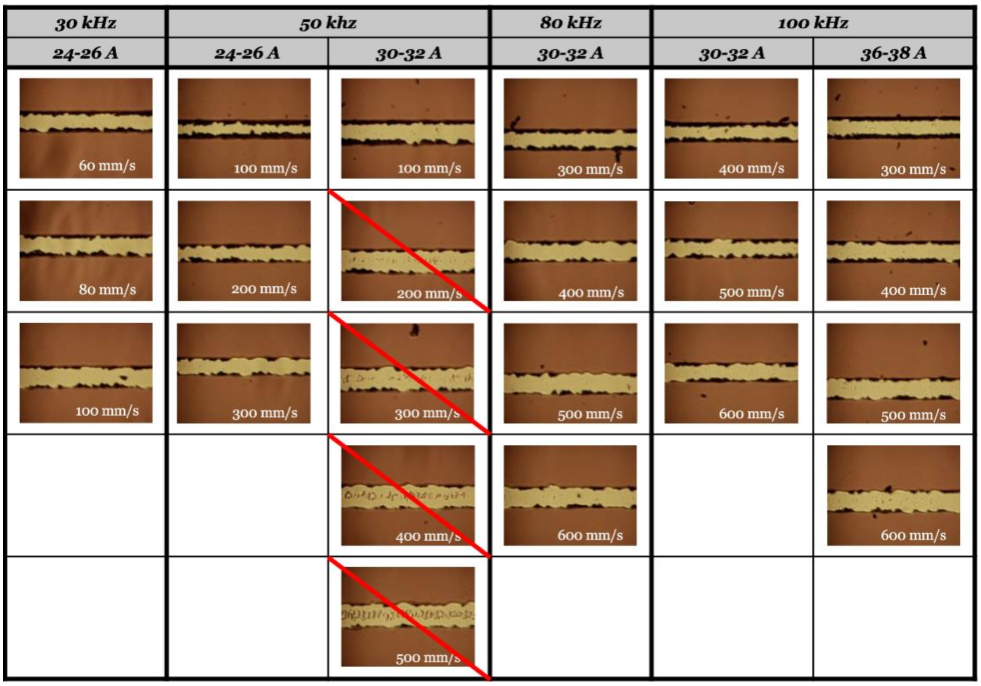

Figure 5.16 Parameter study of P2 scribe

The debris formation can be controlled with increasing frequency and motor stage speed. In addition, the layer thickness also influences the material removal. Figure 5.16 shows the parametric study of the P2 scribes, which are determined individually for each production. Optimized parameters are given in the following section.

5.3.3 Laser scribing of P3

P3 scribing is done via a green (532 nm) laser process. Since the P2 and P3 scribes are both done with the same wavelength, it is essential to find the suitable parameter to ablate the metal layer and not damage the a-Si layer, as seen in Figure 5.17, at low frequencies even if at shallow currents underlying layer is also damaged.

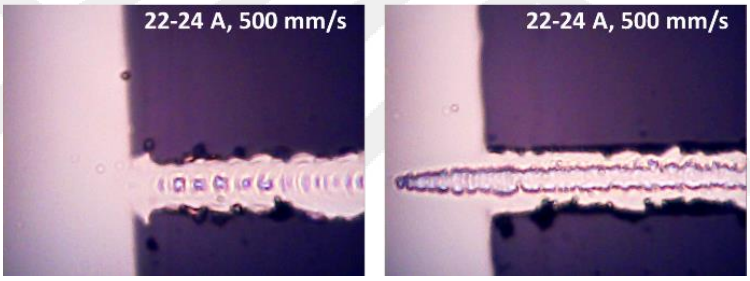

Figure 5.17 P3 scribe at 30 kHz operating at 532 nm

Low powers create more debris, as observed in Figure 5.18. The line width of the scribe defines the death zone of the connected cells. A clean scribe is crucial to obtaining electrical isolation. Any residue such as debris or flakes is short of the structure.

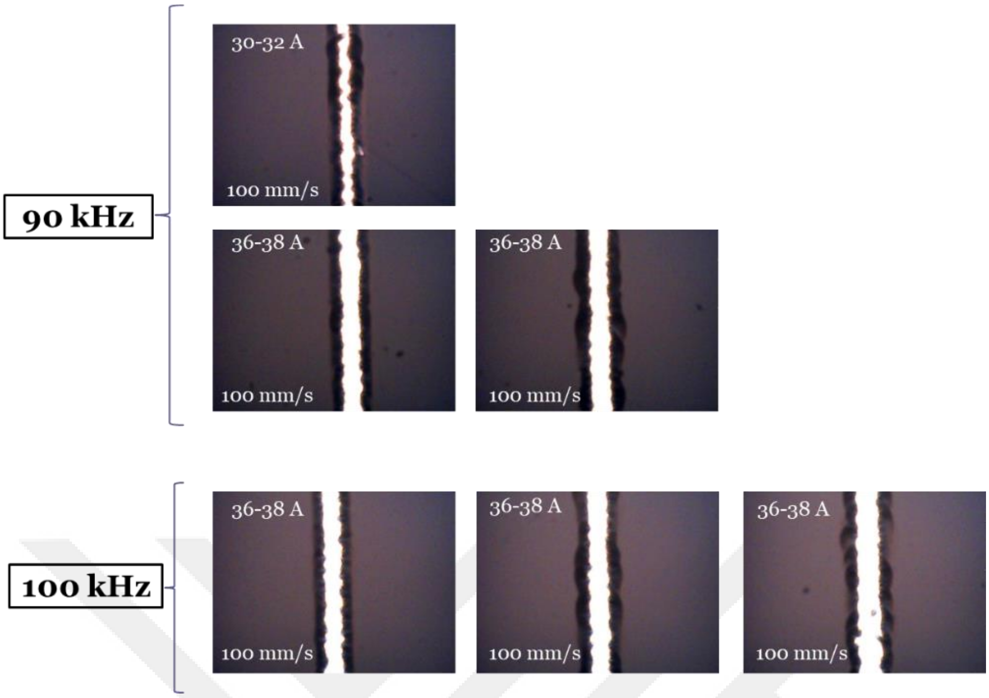

Figure 5.18 P3 scribe at 90 kHz and 100 kHz operating at 532 nm

5.3.4 Results of Thin Film Silicon Solar Cell Module Monolithically Series Connected

A laser scribing study is conducted on ultra-thin flexible glass substrates, also used for solar cell production. Initially, samples are coated with 600 nm thick AZO with previously optimized deposition parameters. Then samples are cut into 3 cm x 3 cm square pieces. These small samples are processed from the film side by UV laser with a 355 nm operation wavelength (P1 scribing). Electrical disconnection of each laser line is also checked via multi-meter. Parameters used for P1 scribing are

- 20 kHz frequency, 36-38 A current, and 550 mm/s motor stage speed.

The simplest and the most effective way to test the P1 scribe line is to look at the electrical connection of the two successive cell areas with a multi-meter. P1 line aims to define and separate the cell regions.

UV irradiation is absorbed by both the aluminum-doped zinc oxide layer and glass substrate. Therefore films are illuminated from the film side. Due to the beam profile, high energy in the center and relatively lower energy at the edge of the laser spot result in deeper grooves in the middle, as seen in Figure 5.19. However, due to the Gaussian nature of the laser beam, scribe lines are deeper in the middle. Figure 5.19 shows the profile of the P1 laser scribe on a p-i-n solar cell measured from the metal contact surface. This profile is observed in each scribe line (P1-P2-P3).

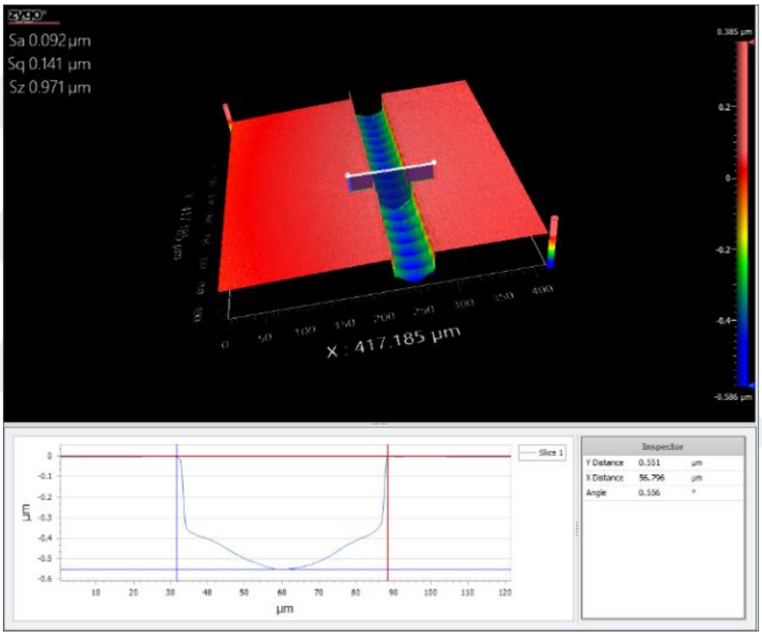

Figure 5.19 Profile of P1 laser scribe on pin solar cell from the contact surface

After p-i-n deposition, samples are removed and scribed with a green laser from the film side. Since the output power of our laser system is high for silicon thin film layers, an attenuator is used. The profile of the P2 line is shown in Figure 5.20. Parameters used for P2 scribing are

- 80 kHz frequency, 27-29 A current, and 700 mm/s motor stage speed.

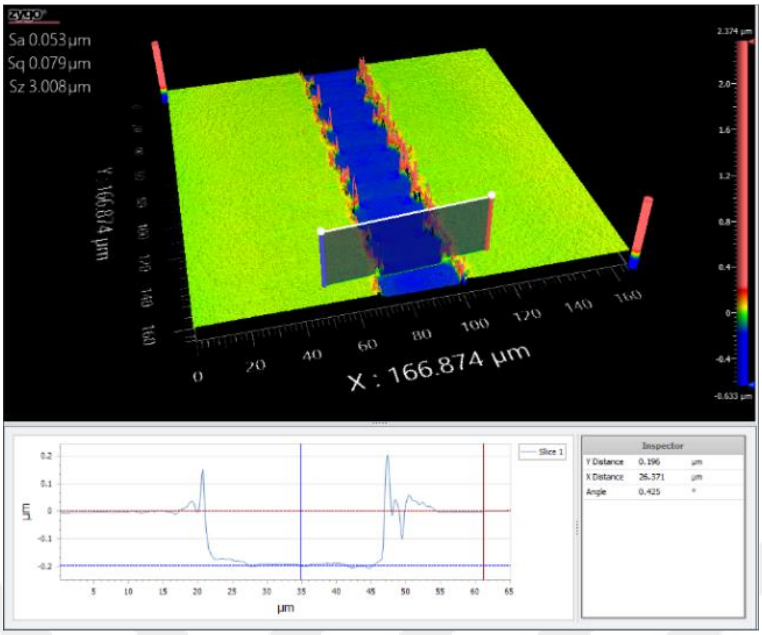

Figure 5.20 Profile of P2 scribe line

Optimization of any of the scribe is related to the film thickness. The essential point of this process is the total layer removal. Residues coming from damaged removal shorts the whole structure or due to the application of high power resulting complete removal of front contact resulting in loss of monolithic connection to next consecutive cell. These problematic issues make the P3 scribe the most critical scribe since metal contact layer removal defines the isolation of each cell. Parameters used for P3 scribing are

- 80 kHz frequency, 27-29 A current, and 700 mm/s motor stage speed.

Each scribe line after total cell production is shown in Figure 5.21.

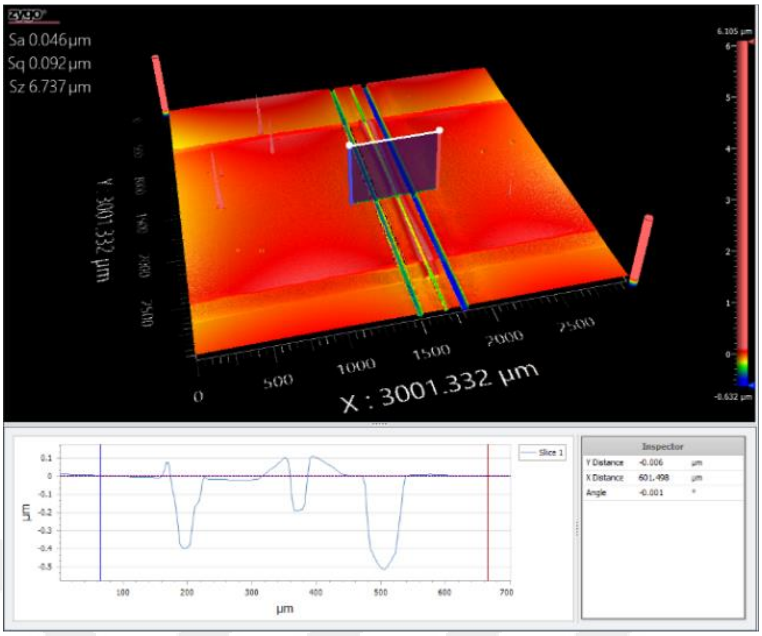

Figure 5.21 Profile of P1-P2-P3 scribe lines

5.3.5 Results of Laser scribed p-i-n deposition and Discussion of Module Results

In order to test laser scribes and monolithic series connection, a complete device production is conducted, as can be seen in Figure 5.22. The results of the first p-i-n module done by laser processes in the GünEr cluster system are shown in Figure 5.23.

This study uses the standard device structure for laser scribes: AZO / p-a-Si:H / i-a-Si:H / n-a-Si:H / Ag in substrate cell configuration. The solar cell deposited for the module application is TYPE-2

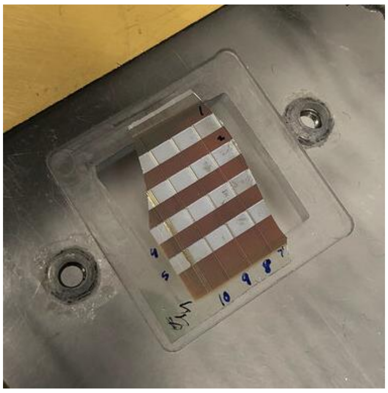

Figure 5.22 Monolithically serries connected first thin film silicon module deposited in GünEr

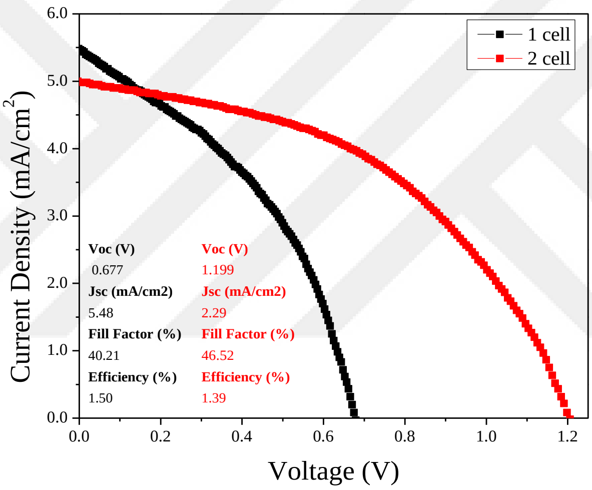

Figure 5.23 First p-i-n module done by laser processes in GÜNER cluster system

Table 5.15 Results of the p-i-n module deposited with TYPE-2 parameters

	Voc (V)	*Jsc (mA/cm^2)*	*Efficiency (%)*	*Fill Factor (%)*
1 cell	0.677	5.48	1.50	40.21
2 cells	1.199	2.29	1.39	46.52

CHAPTER 6

CONCLUSION

The main focus of this thesis is to optimize and produce intrinsic amorphous silicon (i-aSi:H) layers, laser scribing for monolithic series connection for module formation, and deposition of thin amorphous layers for p-i-n type single-junction silicon solar cells. Thin-film deposition optimization in CVD chambers and laser processes is optimized. The aim of this study is to optimize the flexible solar cell process by investigating the effects of deposition parameters on a-Si:H thin film properties and cells, to obtain surface texturing on transparent conductive oxide by a novel texture, which is done by direct laser writing, to scale-up from cell to monolithically series-connected flexible solar module.

Surface texturing studies are of great importance to increase the efficiency of thin film solar cells. This concept is widely studied currently in research groups [72]. In this study, the roughening of transparent conductive thin film layers of solar cells was studied. The texturing of the surfaces with laser application shows the significance of this study. Laser texturing is also a new concept studied as periodic surface texturing [73]. The difference in this work is that random texturing obtained high haze values through a wide spectral range. Unlike wet chemical etching, laser texturing stands out as a method that can be included in the roll-to-roll deposition process.

Silicon-based thin-film solar cells produced in the RF PECVD type thin-film deposition system GünEr and the optimization of amorphous silicon layers are studied. Amorphous silicon layers were produced in three different types intrinsic, p- and n-type. Each type of layer was deposited in separate production chambers and characterized separately.

In order to optimize i-aSi:H layers, samples having different hydrogen to silane ratios are produced. A narrow interval of ratio change is discussed to fine-tune the intrinsic layer characterization concerning the previous optimization set reported. Each layer was characterized electrically. The effect of the hydrogen to silane ratio on the conductivity is reported. According to the optimization results, the best parameters having the highest performance were chosen for device production.

The transparent conductive oxide layer is deposited by the RF magnetron type sputtering thin film growth method and characterized. The layer optimized is used as the top contact layer for thin film flexible solar cells in the superstrate configuration.

The effects of system production pressure, production power, and gas flow parameters on AZO growth were investigated within characterization studies. Since different substrates will be used to produce flexible solar cells and PET substrates with low-temperature resistance are included, the optimization was carried out at room temperature.

Surface texturing studies for the effective use of light in thin film solar cells are studied. A new method, direct laser processing, is developed for surface texturing of the AZO layer. As a result of this study, the texturing is optimized with the laser operated at three different wavelengths. Results of green-laser texture reach haze values as high as 64% and cover the 350nm to 1100 nm spectrum. UV laser texture reaches haze value as high as 55% at 380 nm wavelength. IR texture reaches the haze value as high as 60% at 380 nm wavelength.

The novel part of this thesis study is to achieve light trapping of amorphous silicon solar cells with direct laser writing as a non-chemical method. Samples produced with this method reached an efficiency value of 2.57 % in ultra-violet, 1.83 % in green, and 2.30 % in the infrared wavelength.

Module formation of amorphous silicon solar cells is achieved via three main scribes. The first laser scribed thin film silicon solar cell on the flexible substrate was produced. A monolithic series connection is obtained for two subsequent cells. Thin film scribing is also studied to achieve monolithic series connection of thin film silicon solar cell (TFSSC) by laser processes.

The device structure given here is adapted from literature to obtain the top efficient, flexible solar cell produced in the GünEr PECVD system. Single junction p-i-n silicon solar cells are achieved with 3.43% cell efficiency.

REFERENCES

[1] IEA, “World Energy Outlook 2021 - revised version October 2021,” 2021.

[2] E. Becquerel, “Memoire sur les effects d´electriques produits sous l´influence des rayons solaires,” *Comptes Rendus l’Academie des Sci.*, vol. 9, pp. 561–567, 1839.

[3] D. M. Chapin, C. S. Fuller, and G. L. Pearson, “A new silicon p-n junction photocell for converting solar radiation into electrical power,” *J. Appl. Phys.*, vol. 25, no. 5, pp. 676–677, 1954, doi: 10.1063/1.1721711.

[4] Sterling H F and Swann R C G, “CHEMICAL VAPOUR DEPOSITION BY r . f . DISCHARGE,” *Solid. State. Electron.*, vol. 8, no. 8, pp. 653–654, 1965.

[5] R. C. Chittick, J. H. Alexander, and H. F. Sterling, “1.2411779,” *J. Electrochem. Soc.*, vol. 116, no. 1, pp. 77–81, 1969.

[6] W. E. Spear and P. G. Le Comber, “Substitutional doping of amorphous silicon,” *Solid State Commun.*, vol. 17, no. 9, pp. 1193–1196, Nov. 1975, doi: 10.1016/0038-1098(75)90284-7.

[7] D. E. Carlson and C. R. Wronski, “Amorphous silicon solar cell,” *Appl. Phys. Lett.*, vol. 28, no. 11, pp. 671–673, 1976, doi: 10.1063/1.88617.

[8] C. R. Wronski, D. E. Carlson, and R. E. Daniel, “Schottky-barrier characteristics of metal-amorphous-silicon diodes,” *Appl. Phys. Lett.*, vol. 29, no. 9, pp. 602–605, 1976, doi: 10.1063/1.89158.

[9] D. L. Staebler and C. R. Wronski, “Reversible conductivity changes in discharge-produced amorphous Si,” *Appl. Phys. Lett.*, vol. 31, no. 4, pp. 292–294, 1977, doi: 10.1063/1.89674.

[10] H. Okaniwa, K. Nakatani, M. Yano, M. Asano, and K. Suzuki, “Preparation

and properties of a-si: H solar cells on organic polymer film substrate," *Jpn. J. Appl. Phys.*, vol. 21, no. S2, pp. 239–244, 1982, doi: 10.7567/JJAPS.21S2.239.

[11] A. V. Shah *et al.*, "Thin-film silicon solar cell technology," *Prog. Photovoltaics Res. Appl.*, vol. 12, no. 2–3, pp. 113–142, 2004, doi: 10.1002/pip.533.

[12] K. L. Chopra, P. D. Paulson, and V. Dutta, "Thin-film solar cells: An overview," *Prog. Photovoltaics Res. Appl.*, vol. 12, no. 2–3, pp. 69–92, 2004, doi: 10.1002/pip.541.

[13] S. Y. Myong, L. S. Jeon, and S. W. Kwon, "Superstrate type flexible thin-film Si solar cells using flexible glass substrates," *Thin Solid Films*, vol. 550, pp. 705–709, Jan. 2014, doi: 10.1016/J.TSF.2013.11.039.

[14] "MELINEX ® STCH11 Product Description," 2016. [Online]. Available: https://usa.dupontteijinfilms.com/wp-content/uploads/2017/01/STCH-11-Datasheet.pdf. [Accessed: 23-Mar-2020].

[15] "MELINEX ® STCH12 Product Description." [Online]. Available: https://usa.dupontteijinfilms.com/wp-content/uploads/2017/01/STCH-12-Datasheet.pdf. [Accessed: 23-Mar-2020].

[16] "Ultra-Thin Glass for Electronics Applications." [Online]. Available: https://www.schott.com/d/advanced_optics/db832253-0598-4da4-8c88-8784839ccc8b/1.0/schott-ultra-thin-glass-electronics-appl-nov-2015-eng.pdf. [Accessed: 23-Mar-2020].

[17] W. C. O. Mara, R. B. Herring, and L. P. Hunt, "HANDBOOK OF SEMICONDUCTOR Edited by," pp. 1–843, 1990.

[18] U. Kroll, J. Meier, A. Shah, S. Mikhailov, and J. Weber, "Hydrogen in amorphous and microcrystalline silicon films prepared by hydrogen dilution," *J. Appl. Phys.*, vol. 80, no. 9, pp. 4971–4975, 1996, doi: 10.1063/1.363541.

[19] A. Shah, *THIN-FILM SILICON*. EPFL Press, 2010.

[20] A. Janotti and C. G. Van de Walle, “Fundamentals of zinc oxide as a semiconductor,” *Reports Prog. Phys.*, vol. 72, no. 12, p. 126501, Dec. 2009, doi: 10.1088/0034-4885/72/12/126501.

[21] P. Barquinha, R. Martins, L. Pereira, and E. Fortunato, *Transparent Oxide Electronics*. West Sussex, UK: John Wiley & Sons, Ltd., 2012.

[22] M. G. Faraj and K. Ibrahim, “Optical and structural properties of thermally evaporated zinc oxide thin films on polyethylene terephthalate substrates,” *Int. J. Polym. Sci.*, vol. 2011, no. December 2013, 2011, doi: 10.1155/2011/302843.

[23] H. L. Shen, H. Zhang, L. F. Lu, F. Jiang, and C. Yang, “Preparation and properties of AZO thin films on different substrates,” *Prog. Nat. Sci. Mater. Int.*, vol. 20, no. 1, pp. 44–48, 2010, doi: 10.1016/s1002-0071(12)60005-7.

[24] E. Fortunato, P. Nunes, D. Costa, D. Brida, I. Ferreira, and R. Martins, “Characterization of aluminium doped zinc oxide thin films deposited on polymeric substrates,” *Vacuum*, vol. 64, no. 3–4, pp. 233–236, 2002, doi: 10.1016/S0042-207X(01)00319-0.

[25] B. Jeong *et al.*, “Optical and electrical properties of amorphous carbon films deposited using filtered cathodic vacuum arc with pulse biasing,” *Thin Solid Films*, vol. 447, no. 1, pp. 148–152, 2004, doi: 10.1016/S0040-6090.

[26] J. K. Rath *et al.*, “Transparent conducting oxide layers for thin film silicon solar cells,” *Thin Solid Films*, vol. 518, no. 24 SUPPL., pp. e129–e135, 2010, doi: 10.1016/j.tsf.2010.03.104.

[27] Y. Igasaki and H. Kanma, “Argon gas pressure dependence of the properties of transparent conducting ZnO:Al films deposited on glass substrates,” *Appl. Surf. Sci.*, vol. 169–170, pp. 508–511, 2001, doi: 10.1016/S0169-4332(00)00748-0.

[28] H. Kim *et al.*, “Effect of aluminum doping on zinc oxide thin films grown by pulsed laser deposition for organic light-emitting devices,” *Thin Solid Films*, vol. 377–378, pp. 798–802, 2000, doi: 10.1016/S0040-6090(00)01290-6.

[29] I. V. Minin and O. V. Minin, *Elements of diffraction quasi-optics*, no. 3. 1994.

[30] E. T. Flaherty, J. Marshall, P. Albert, A. M. Brzychcy, D. Forbes, and R. Halverson, “Stability of Diborane Mixtures Used for Borophosphosilicate Glass Films,” *J. Electrochem. Soc.*, vol. 140, no. 6, pp. 1709–1713, 1993, doi: 10.1149/1.2221628.

[31] A. Bogaerts, “The glow discharge: An exciting plasma!,” *J. Anal. At. Spectrom.*, vol. 14, no. 9, pp. 1375–1384, 1999, doi: 10.1039/a900772e.

[32] A. Shah, *Thin-Film Silicon Solar Cells1*, Second Edi. Elsevier Ltd, 2013.

[33] R. W. Collins and A. S. Ferlauto, “Advances in plasma-enhanced chemical vapor deposition of silicon films at low temperatures,” *Curr. Opin. Solid State Mater. Sci.*, vol. 6, no. 5, pp. 425–437, 2002, doi: 10.1016/S1359-0286(02)00095-5.

[34] Y. Ni, S. Yu, H. Jiang, and L. He, “The shape of telephone cord blisters,” *Nat. Commun.*, vol. 8, pp. 1–6, 2017, doi: 10.1038/ncomms14138.

[35] J. Ramanujam and A. Verma, “Photovoltaic properties of a-Si:H films grown by plasma enhanced chemical vapor deposition: A review,” *Mater. Express*, vol. 2, no. 3, pp. 177–196, 2012, doi: 10.1166/mex.2012.1073.

[36] J. Kanicki, *Amorphous and microcrystalline semiconductor devices. Volume II, Materials and device physics*. Boston: Artech House, 1992.

[37] D. S. Ginley and J. D. Perkins, “Handbook of Transparent Conductors,” *Handb. Transparent Conduct.*, pp. 1–25, 2011, doi: 10.1007/978-1-4419-1638-9.

[38] K. M. Yu, M. A. Mayer, D. T. Speaks, H. He, R. Zhao, L. Hsu, S. S. Mao, E. E. Haller, and W. Walukiewicz, J. Appl. Phys. 111, 123505 (2012)

[39] H. Liu, V. Avrutin, N. Izyumskaya, Ü. Özgür, and H. Morkoç, Superlattice Microst. 48, 458 (2010)

[40] S. Fernández, and F.B. Naranjo, Sol. Energy Mater. Sol. Cells 94, 157 (2010)

[41] M.Y. Zhang, Q. Nian, and G.J. Cheng, Appl. Phys. Lett. 100, 151902 (2012)

[42] A. Plichta, A. Weber and A. Habeck (2003). MRS Proceed-ings 769, H9.1 DOI 10.1557/PROC-769-H9.1 (2003)

[43] S. Garner, G. Merz, G. S. Glaesemann, J. Tosch, C. Chang, D. Marshall, X. Li, L. Tian, K. Vasilakos and A Gagov, SID. Int. Symp. Dig. Tec. 43, 342 (2012)

[44] S. M. Garner, K. Wu, Y. C. Liao, J. W. Shiu, Y. S. Tsai, K. T. Chen, Y. C. Lai, C. Lai, Y. Lee, J. C. Lin, X. Li, and P. Cimo, J. Display Technol. 9, 644 (2013)

[45] Z. Fang, H. Zhu, Y. Li, Z. Liu, J. Dai, C. Preston, S. Garner, P. Cimo, X. Chai, G. Chen, and L. Hu, Scientific Reports 4, 5842 (2014)

[46] W. Beyer, J. Hüpkes, and H. Stiebig, Thin Solid Films 516, 147 (2007)

[47] H.C. Weller, R.H. Mauch, G.H. Bauer, Sol. Energ. Mat. Sol. C 27, 217 (1992)

[48] M. De la, L. Olvera, A. Maldonado, and R. Asomoza, J. Ma-ter. Sci. Mater. Electron. 11, 1 (2000)

[49] H. Nasser, E. Özkol, A. Bek, and R. Turan, Opt. Mater. Ex-press 5, 932 (2015)

[50] W. Yanga, Z. Liua, DL. Pengb, F. Zhanga, H. Huanga, Y. Xiea, and Z. Wua, Appl. Surf. Sci.255, 5669 (2009)

[51] Z.L. Pei, X.B. Zhang, G.P. Zhang, J. Gong, C. Sun, R.F. Huang, and L.S. Wen, Thin Solid Films 497, 20 (2006)

[52] T. Miyata, Y. Minamino, S. Ida, and T. Minami, J. Vac. Sci. Technol. A 22, 1711 (2004)

[53] H Kim, J.S Horwitz, S.B Qadri, and D.B Chrisey, Thin Solid Films 420-421, 107 (2002)

[54] K. Ellmer, J. Phys. D: Appl. Phys. 33, R17 (2000)

[55] E. Fortunato, P. Nunes, D. Costa, D. Brida, I. Ferreira, and R. Martins, Vacuum 64, 233 (2000)
[56] M. P. Seah, Thin Solid Films **81**, 279 (1981)
[57] A. R. Nyaiesh, and L. Holland, Vacuum **31**, 315(1981)
[58] X. Chen, W. Guan, G. Fang and X. Z. Zhao, Appl. Surf. Sci. **252**, 1561 (2005)
[59] S. Fernández, A. Martínez-Steele, J.J. Gandía, and F.B. Naranjo, Thin Solid Films **517**, 3152 (2009)
[60] C. C. Hu, T. W. Lu, C. Y. Chou, J. T. Wang, H. H. Huang, and C. Y. Hsu, Bull. Mater. Sci. 37, 1275 (2014)
[61] Y. Liu, Y. Li, and H. Zeng Journal of Nanomaterials Volume 2013
[62] J. I. Owen, J. Hüpkes, H. Zhu, E. Bunte, and S. E. Pust, "Novel etch process to tune crater size on magnetron sputtered ZnO:Al," Phys. Status Solidi A 208(1), 109–113 (2011)
[63] W. L. Lu, K. C. Huang, C. H. Yeh, C. I. Hung, and M. P. Houng, "Investigation of textured Al-doped ZnO thin films using chemical wet-etching methods," Mater. Chem. Phys. 127(1-2), 358–363 (2011)
[64] E. Bunte, H. Zhu, J. Hüpkes, and J. Owen, "Novel texturing method for sputtered zinc oxide films prepared at high deposition rate from ceramic tube targets," EPJ Photovo. 2, 20602 (2011)
[65] S. Eckhardt et al. Physics Procedia 41 (2013) 552 – 557
[66] T. Knüttel, S. Bergfeld and S. Haas JLMN-Journal of Laser Micro/Nanoengineering Vol. 8, No. 3, 2013
[67] S. Eckhardt et al. Light Management in AZO Thin Film Electrodes ADVANCED ENGINEERING MATERIALS 2013, 15, No. 10
[68] S. Lauzurica, M. Lluscàb, D. Cantelia, M.I. Sánchez-Aniortea, J. López-Vidrierb, S. Hernándezb, J.Bertomeu b, C. Molpeceresa Proc. of SPIE Vol. 9180 918006-1
[69] S. Ku et al. / Solar Energy Materials & Solar Cells 108 (2013) 87–92
[70] S. Haas, A. Gordijn and H. Stiebig Prog. Photovolt: Res. Appl. 2008; 16:195–203

[71] J.J. Garcia-Ballesteros, S. Lauzurica, C. Molpeceres, I. Torres, D. Canteli, J.J. Gandia Physics Procedia 5 2010; 293-300

[72] G. Limodio *et al.*, "Modulated surface texturing of temporary Al foils substrates for high-efficiency thin-film, flexible solar cells," *2021 IEEE 48th Photovoltaic Specialists Conference (PVSC)*, 2021, pp. 1103-1105, doi: 10.1109/PVSC43889.2021.9518843.

[73] D. Canteli, I. Torres, S. Fernández, J.D. Santos, M. Morales, C. Molpeceres, "Photon-collection improvement from laser-textured AZO front-contact in thin-film solar cells," *Applied Surface Science*, 463, 2019, pp. 775-780

CURRICULUM VITAE

PERSONAL INFORMATION

Surname, Name: Demircioğlu, Zeynep
Nationality: Turkish (TC)

EDUCATION

Degree	Institution	Year of Graduation
MS	METU Physics	2011
BS	METU Physics	2008
High School	Başkent Üni. Özel Ayşeabla Fen Lisesi, Ankara	2004

WORK EXPERIENCE

Year	Place	Enrollment
2021-Present	TUBİTAK SAGE	Chief Researcher
2017-2021	TUBİTAK UZAY	Chief Researcher
2016-2017	GUNAM	Research Assistant
2008-2016	METU Dept. of Physics	Research Assistant

FOREIGN LANGUAGES

Advanced English,

PUBLICATIONS

1. Demircioglu Z., Nasser H., Balog R. S., and Turan R., "Effect of Laser Wavelength on AZO Surface Texturing by Direct Laser Processing / Patterning for Thin-Film Silicon Solar Cells Applications," MRS Advances, Volume 3, no. 25, pp. 1411–1418, 2018

2. M. Ünal, Z. Demircioğlu, E. Dönerçark, E. Özkol, R. Turan, "Aluminum induced texturing of sandy and prism glasses: combination of micro/nano texture with macro texture", Physica Solidi Status-a, Volume 214, Issue 8, page 1600856, August 2017

3. Z. Demircioğlu, E. Özkol, H. Nasser, R. Turan, "Low temperature aluminum doped zinc oxide thin film deposition on ultra-thin flexible glass and PET substrates

by RF magnetron sputtering", Physica Status Solidi (c), Volume 12, Issue 9-11, pages 1215–1219, November 2015

4. S. Galioğlu, M. İşler, Z. Demircioğlu, M. Koç, F. Vocanson, and N. Destouches "Photochromic behavior of silver nanoparticle incorporated titanosilicate ETS-10 films", Microporous and Mesoporous Materials, Volume 196, 15 September 2014, Pages 136–144

CONFERENCE PAPERS, PRESENTATIONS, POSTERS

1. M. Ünal, **Z. Demircioğlu**, E. Dönerçark, E. Özkol, R. Turan, "*Aluminum Induced Texturing of Glasses Combined with Macro-scale Texture and Their Effect on Efficiency of a-Si:H*", E-MRS Fall Meeting 2016
2. E. Özkol, **Z. Demircioğlu**, S. Kıncal, R. Turan, "*Effects of Plasma Properties on Defect Density and Doping of a-Si:H in PECVD System*". The Turkish-German Conference on Energy Technologies, METU, Ankara, Turkey, 13-15 October, 2014
3. **Z. Demircioğlu**, E. Ozkol, R. Turan, "*Optimization of a-Si:H thin film deposited on ITO coated flexible substrate*", ***Oral*** Presentation, Nano TR10, Istanbul 2014
4. M. Unal, H. Nasser, E. Ozkol, **Z. Demircioglu**, R. Turan, "*Aluminum Induced Nanotexturing of Glass Superstrate for Enhanced Photo-response of a-Si:H Thin Film*", ***Oral*** Presentation, Nano TR10, Istanbul 2014
5. E. Özkol, G. Nogay, H. Nasser, **Z. Demircioğlu**, G. Yılmaz, H. Cansever, S. Kıncal, M. Güneş, R. Turan, "*Effects of Plasma Properties on Doping a-Si in Capacitatively Coupled Plasma System*" , 28th European PV Solar Energy Conference and Exhibition (EU PVSEC 2013), Paris, France, 30 Sep-04 Oct 2013
6. S. Galioğlu, M. İşler, **Z. Demircioğlu**, M. Koç, F. Vocanson, and N. Destouches, "*Photochromic behavior of silver nanoparticle incorporated titanosilicate ETS-10 films*", E-MRS Spring 2013
7. E. Özkol, G. Nogay, H. Nasser, **Z. Demircioğlu**, S. Kıncal, "*New Cluster PECVD system at GÜNAM*", ***Oral*** Presentation; Solar Electricity Conference and Exhibition (Solar-TR-2), Antalya, Turkey 07-09 November 2012, P. 31